Evaluation of Seismic Probability and Fault Reactivation for Enhanced Geothermal Systems

by

Faraz Valipoor Goodarzi

A thesis

presented to the University of Waterloo

in fulfillment of the

thesis requirement for the degree of

Master of Applied Science

in

Civil Engineering

Waterloo, Ontario, Canada, 2017

AUTHOR'S DECLRATAION

I hereby declare that I am the sole author of this thesis. This is a true copy of the thesis, including any required final revisions as accepted by my examiners. I understand that my thesis may be made electronically available to the public.

ABSTRACT

Growth in energy demand from developing nations necessitates the utilization of all available sources of energy. Primarily due to their environmental benefits, clean and renewable energy resources are of particular interest. Moreover, since renewable energy is gathered from naturally replenished sources, it is widely available around the world. Origins of renewable energy include sunlight, rain, wind, waves, and geothermal heat. Of these, geothermal heat is the area of focus in this research.

The main goal of geothermal energy technology is to find a way to transfer the thermal energy to the surface where it can be used for heating and generating electricity. All geothermal technologies are based on this principle. The process of geothermal energy extraction can take place in both shallow and deep layers of crust. Among the commonly available energy extraction technologies, Enhanced Geothermal System (EGS) is of particular interest in this research. Through EGS, a cold fluid is injected into the ground and extracted heat energy is delivered through a process called “hydraulic stimulation”.

The target of this research is to develop a model to investigate the geomechanical issues of a deep EGS set-up in addition to the influence of the “hydraulic stimulation” process on the geologic medium, particularly the problem of induced seismicity in a pre-existing fault which exists in the system. A 2D numerical finite element code is developed to

analyze the behavior of porous subsurface in terms of displacement, stress, fluid pressure distribution, and temperature through a coupled thermo-hydro-mechanical (THM) approach using the corresponding mathematical governing equations. After modeling an EGS setup and stimulation program, an efficient approach is introduced along the concept of Mohr-Coulomb diagram which enables studying the seismic risk potential in an EGS using the final stress state of the geologic medium obtained from the THM approach.

ACKNOWLEDGEMENT

I would like to acknowledge the Department of Civil and Environmental Engineering for the funding for this research. I would like to express my gratitude to my advisors, Prof. Dipanjan Basu and Prof. Maurice Dusseault for their support. I would like to sincerely thank my parents and my friends.

December 16, 2016

Table of Contents

CHAPTER 1 – Geothermal Energy: Overview and Research Scope

1.1 Introduction

Concerns about the environmental impacts and carbon footprint of fossil fuel emissions led to the initiation of research and development in the fields of renewable and clean energy. Among the renewable energy sources, geothermal energy has certain advantages. Geothermal energy holds a relatively higher capacity factor (i.e., actual output versus generation potential) than other renewable energy sources (Figure 1.1), which can make it a reliable source of electricity (Grasby et al., 2012). The total capacity of geothermal power plants installed all over the world was 12,635 MW in 2015, which is equal to 73,549 GWh of electricity (Bertani, 2015). Compared to other renewable energy sources, geothermal energy is relatively low-cost (Figure 1.2). These benefits along with potential worldwide accessibility make geothermal energy an appealing source of renewable energy.

In Canada, over 5,000 MW of power generation is estimated to be available from shallow geothermal resources such as sedimentary aquifers. This estimation could reach up to 15,000 MW if the available potential from deep geothermal systems (particularly the Enhanced Geothermal System) is added (Bertani, 2015). However, currently there is no geothermal-based electrical power generation in Canada notwithstanding Geological Survey of Canada's reports of the high potential of geothermal energy resources. Besides policy limitations and concerns over costs of deep drilling, this absence is mainly due to a 30-year break in federal government funding of geothermal science (Thompson et al., 2015). Nevertheless, from previous experiences and pilot projects it is now clear that geothermal energy is widely feasible in Canada.

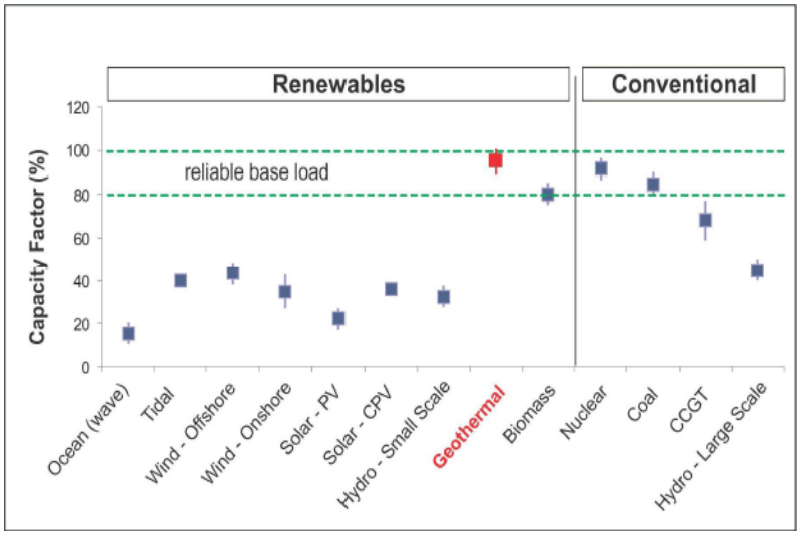

Figure 1.1 Typical capacity factors of different power generation technologies. (Emerging Energy Research, 2009). PV = photovoltaics, CPV = concentrated photovoltaics, CCGT = combined-cycle gas turbine

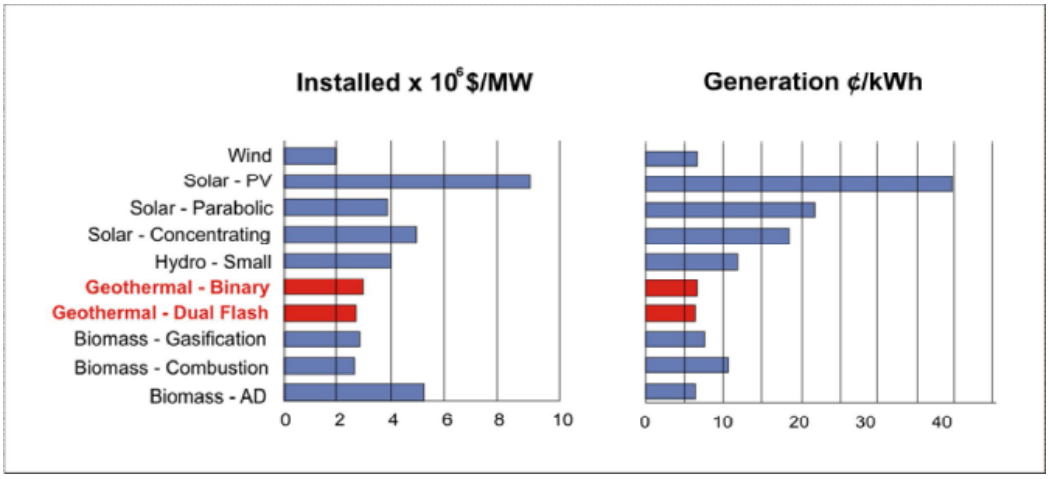

Figure 1.2 Comparison of installation and generation costs for various renewable energy resources (California Energy Emissions, 2007).

1.2 Geothermal Energy

1.2.1 Geothermal Energy Definition

Heat in the earth's inner layers is mainly generated from radioactive decay of uranium, thorium, and potassium, in addition to the pre-existing heat from primeval earth formation (Grasby et al., 2012). This heat energy is called the geothermal energy, which normally finds its way to the surface and creates a temperature gradient with depth. Because this source of heat exists all over the earth, geothermal energy is a widely available resource. However, specific technologies should be used to extract geothermal energy economically.

Geothermal energy is conveyed vertically upward to the ground surface if three conditions are satisfied. First, a sufficiently hot rock formation should be economically and potentially available for heat extraction. Second, a fluid should exist to convey the heat energy to the surface. And third, there should be enough permeability to allow the fluid to move through the geologic medium. All the existing geothermal heat extraction technologies are based on these three elements without exception. Newer technologies are achieving higher efficiencies of geothermal energy extraction by improving the efficiency of at least one of these elements. For example, energy production can be improved by artificially enhancing the thermal and hydraulic conductivities of the geologic medium. Production efficiency can also be enhanced by improving the thermodynamic aspects so that the required temperature differential for electricity production decreases. These improvements contribute to the worldwide appeal of geothermal energy.

1.2.2 Geothermal Resource Types

Geothermal resources range widely from shallow groundwater to deep, hot, and dry rock formations (Grasby et al., 2012). The formation temperature is dependent on factors

such as redundancy of radioactive origins, thermal conductivity of the base rock, and volcanic processes. Typically, geothermal resources are categorized, based on their temperature ranges, into three types: high-temperature (greater than 150 °C), medium temperature (between 80 °C and 150 °C), and low-temperature (less than 80 °C). For electricity generation, high- and medium-temperature resources are of particular interest, whereas low-temperature resources are generally used for direct space heating (Grasby et al., 2012).

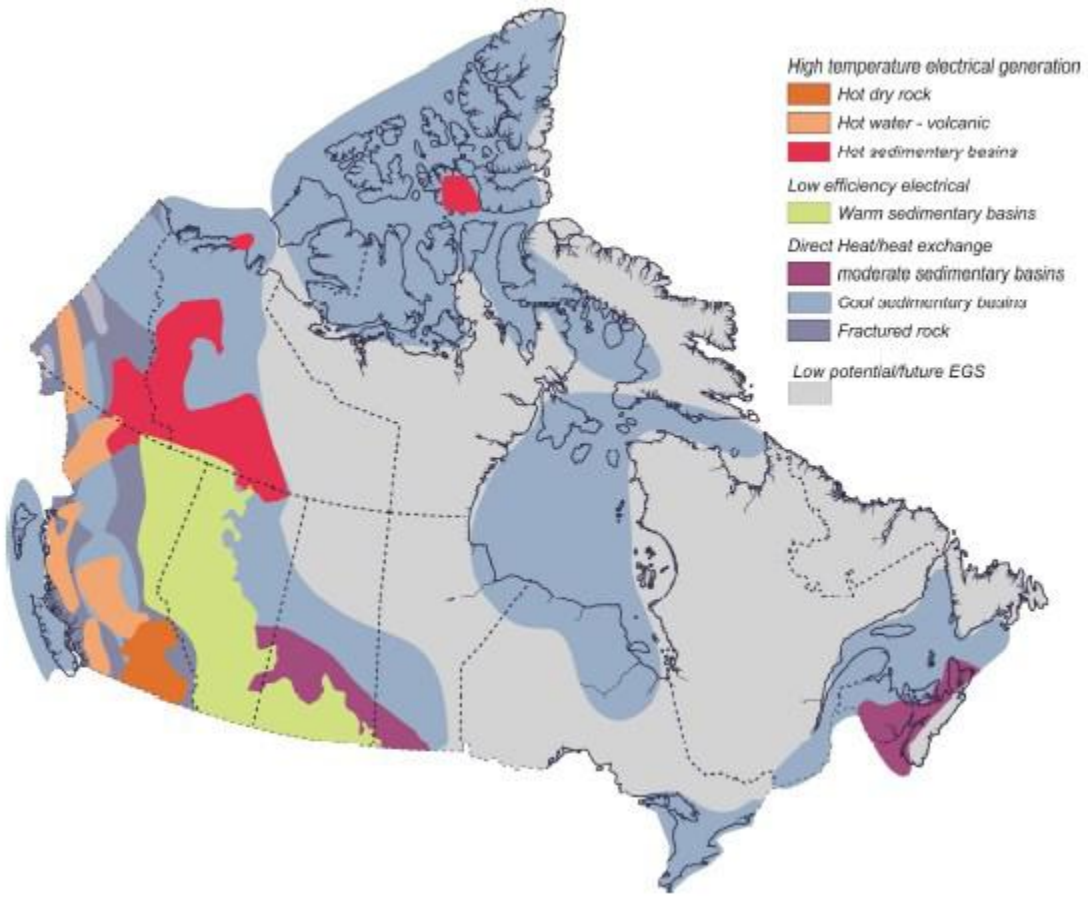

Figure 1.3 Canadian geothermal resource potential (Grasby et al., 2012).

1.2.3 Low- to Medium-Temperature Geothermal Energy

Although the focus of the research work presented in this thesis is on high-temperature geothermal systems, low- and medium-temperature geothermal systems are briefly introduced so that the overall perspective on geothermal systems is clear to the reader. The low- to medium-temperature geothermal systems obtain the heat energy from shallow depths (shallow geothermal systems), and their main function is direct use of hot water for space heating, agriculture (greenhouses), aquaculture, recreation (spas), medical (balneology), and industrial use (Ghomshei and Sadler-Brown, 1996). Figure 1.4 shows the percentage applications of direct use geothermal systems.

Good examples of low-temperature geothermal energy include geo-exchange systems, which may also be known as ground source heat pump systems; ground-coupled systems; earth energy systems; or, where storage is involved, aquifer or borehole thermal energy storage systems depending on their exact function and purpose of use. These systems can be open-loop or closed-loop. In open loop systems, water is extracted via a vertical well and used for heat exchange, whereas in closed-loop systems, a horizontal or vertical loop is added to the system and heat exchange takes place within the loop (Figure 1.5). If the horizontal loop is set up adjacent to the bottom of a close lake or pond, it is called pond loop. Pond loop is the most economical closed-loop system for heat storage, as it is useful in both summer and winter (CGC, 2009). Open-loop and closed-loop applications commonly exist for using the subsurface as thermal energy storage. Open-loop systems such as Aquifer Thermal Energy Storage (ATES) are useful where an aquifer exists, and closed-loop systems such as Borehole Thermal Energy Storage (BTES) are useful as an alternative in the absence of aquifers.

Although these resources are not as efficient as high-temperature resources for electricity generation purposes, they are available to produce electrical power by utilizing a binary cycle plant (DiPippo, 2004). In this technique, a second liquid with a low boiling point is "flashed" or vaporized by the geothermal heat in a heat exchanger (Figure 1.6). As this vapor expands and rises, it passes through a turbine coupled to a generator (Barbier, 2002). After having passed through the turbine, the vapor is condensed and recycled back to the heat exchanger. The efficiency of these systems is low at less than 6% (Barbier, 2002), mainly because binary plants are poor converters of heat into work. However, some plants have achieved an efficiency of more than 40% (DiPippo, 2004). Despite these low efficiencies, binary power plant technology has emerged in the global market as a low-cost and reliable means of electricity generation from medium-temperature reservoirs (Barbier, 2002; Bertani, 2005).

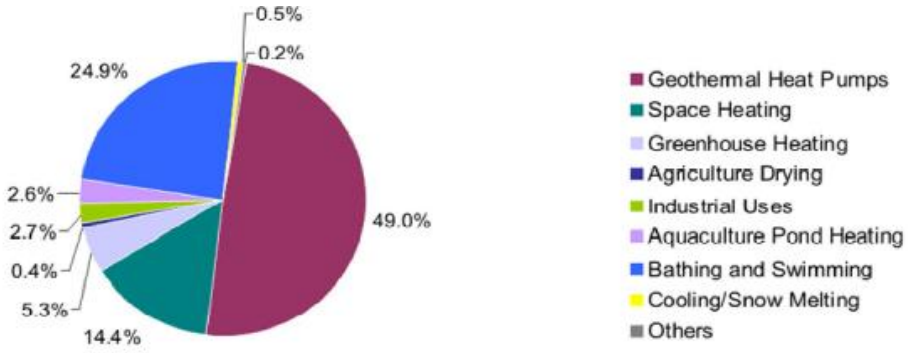

Figure 1.4 Direct use of geothermal energy applications worldwide (percentage of total energy use) (Lund et al., 2010).

1.2.4 High-Temperature Geothermal Energy

In high-temperature geothermal resources, a high geothermal gradient exists in the geologic medium. Usually, there are hot springs or steam vents in these locations as

evidence of such geothermal activities. These high-temperature heat sources are comprised of a large body of rock formation at great depths (Grasby et al., 2012). The main types of high-temperature geothermal resources are water/vapor-dominated hydrothermal systems, hot dry rocks (HDR), and magmatic geothermal resources. The HDR can be used to extract energy by a new technology in which hydraulic stimulation is performed, as described later, and this technology of geothermal energy extraction is known as Enhanced Geothermal System (EGS).

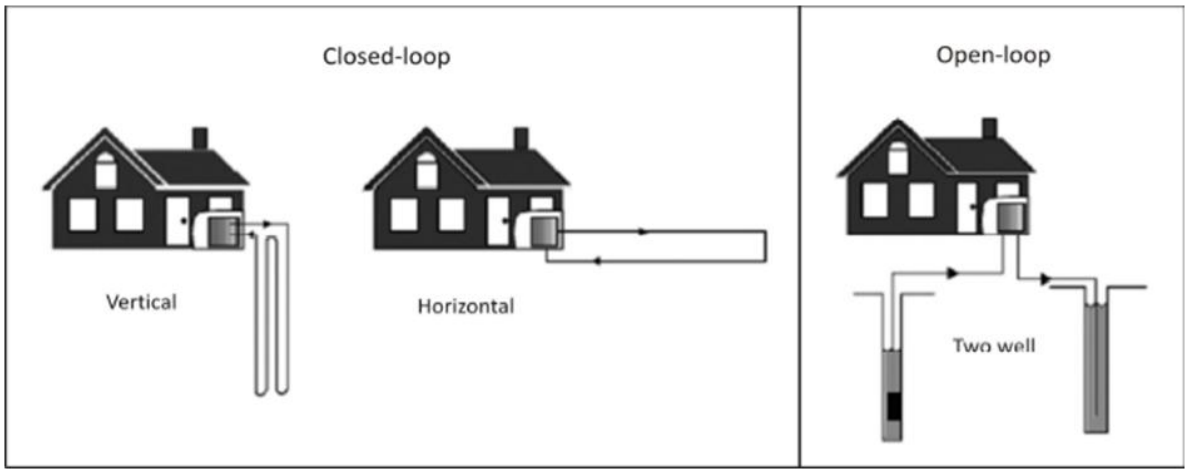

Figure 1.5 A simplified illustration of two typical geo-exchange systems: closed-loop and open-loop (Lund et al., 2004).

1.2.4.1 Hydrothermal Systems

These are natural geothermal resources where hot water or steam is present in the geologic formation and directly available for human use. These thermal fluids are primarily derived from precipitation, which infiltrate into the recharge areas at the surface and move downward increasing in temperature and eventually penetrate the hot rocks of the geothermal reservoir. Because of density variations caused by temperature, water moves inside the reservoir by convection, transferring heat from the lowest parts of the reservoir to

its upper parts and create a reservoir of fairly uniform temperature (Barbier, 2002). The formation rocks contribute to the process by conducting the heat within the reservoir.

Hydrothermal systems can be water-dominated or vapor-dominated systems. Water-dominated systems (fields) deliver either hot water (hot water field) or a mixture of water and steam (wet steam field) as the medium containing the heat energy. In vapor-dominated systems (fields), steam is naturally ejected from the geologic formation. Water-dominated fields are more commonly found than vapor-dominated fields (Hochstein, 1990).

In hot water fields, the temperature in the reservoir is below the boiling point of water because of which only hot water is produced at the surface (Barbier, 2002). A hot water hydrothermal field is economically beneficial if the reservoir is found at a depth of less than two kilometers, if the salt content of the water is lower than 60 g/kg, and if the wells have high flow-rates (above 150 tons/hour) (Barbier, 2002). The best known examples of exploited hot water fields are those in the Pannonian Basin (Hungary), the Paris Basin (France), the Aquitanian Basin (France), several formations in Russia, the Po River Valley (Italy), Klamath Falls (Oregon, USA), and Tianjin (China) (Barbier, 2002).

In wet steam fields, bubbles of steam mixed with liquid water exist in the shallow and low-pressure parts of the reservoir (Barbier, 2002). The pressure inside the reservoir is governed by the liquid phase. When the fluid is brought to the surface via a well and its pressure decreases, a fraction of the fluid is flashed to steam, while the greater part remains as boiling water (Barbier, 2002). The water and steam are then separated, and the steam is used for electricity generation. The large amount of extracted water which contains chemical elements such as chlorates and sulfates is disposed of by re-injection to the reservoir. Wet steam fields are the most commonly used hydrothermal systems in the world (Grasby et al.,

2012). According to Barbier (2002), world's most noteworthy wet steam fields producing electricity are in Cerro Prieto, Los Azufres, Los Humeros (Mexico); Momotombo (Nicaragua); Ahuachapa´n-Chipilapa (El Salvador); Miravalles (Costa Rica); Zunil (Guatemala); Wairakei, Ohaaki, Kawerau (New Zealand); Salton Sea, Coso, Casa Diablo (California); Puna (Hawaii); Soda Lake, Steamboat, Brady Hot Springs (Nevada); Cove Fort (Utah); Dieng, Salak (Indonesia); Mak-Ban, Tiwi, Tongonan, Palinpinon, Bac Man (Philippines); Pauzhetskaya, Mutnovsky (Russia); Fang (Thailand); Kakkonda, Hatchobaru, Mori (Japan); Olkaria (Kenya); Krafla (Iceland); Azores (Portugal); Kizildere (Turkey); Latera (Italy); and Milos (Greece).

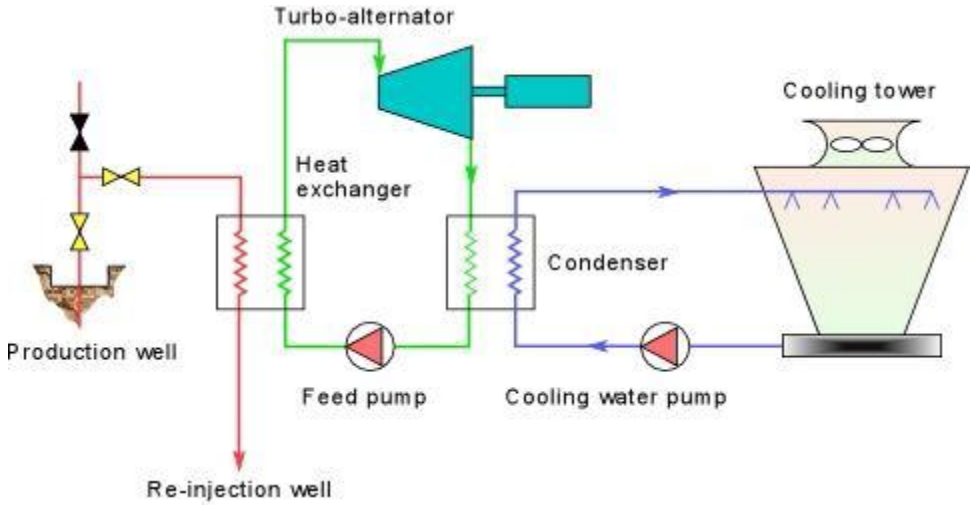

Figure 1.6 A simplified illustration of binary power plant (Dickson and Fanelli, 2004).

In vapor-dominated fields, the heat source is deep enough to produce a dry saturated or slightly superheated steam at the surface (Grasby et al., 2012). Contrary to wet steam fields, here the presence of an impermeable confining layer is necessary. The steam phase is dominant and governs the pressure inside the reservoir. The pressure drop occurs when a

well infiltrates the reservoir, leading to boiling and vaporization of liquid water. The surrounding hot rock prevents the cooling of the produced steam and therefore the steam temperature remains above the vaporization value. Approximately half of the geothermal-based electric energy generated in the world comes from the following six vapor-dominated fields (Grasby et al., 2012): Larderello (Italy), Mt. Amiata (Italy), the Geysers (California), Matsukawa (Japan), and Kamojang and Darajat (Indonesia).

Electricity generation can take place utilizing three types of power plants based on the three types of hydrothermal systems mentioned above. Binary-cycle plants, introduced in the previous section, are used for hot water fields. Flash steam plants are used for wet steam fields, where the pressurized water is guided to a low-pressure tank and then the flash steam is used to turn turbines. Dry steam plants are used for vapor-dominated fields, where the produced steam is directly utilized to drive turbines. If exploited properly, hydrothermal systems are quite reliable as a clean and renewable energy source over a long period of time.

1.2.4.2 Magma Energy

The heat stored in magma (molten geologic matter) can be considered a possible geothermal source (Barbier, 2002). Although this technology has not been applied yet, studies are in progress in order to extract magma thermal energy in countries such as Japan (Tomiya, 2000). According to Dunn (1988), the main issues related to heat extraction from magma are locating the magma bodies, capability of high-temperature drilling, accessibility of required engineering materials, and an appropriate heat extraction technology. All these factors should be considered keeping in mind the economic feasibility so that an efficient magma energy extraction process can be obtained.

1.2.4.3 Hot Dry Rocks (HDR) and Enhanced Geothermal System (EGS)

Enhanced Geothermal System (EGS) (MIT, 2006) is a relatively new system in which the presence of a natural water source is not required. It is highly advantageous to establish a geothermal energy source without requiring this natural fundamental element because the EGS technology can then be implemented anywhere irrespective of the subsurface geological conditions. This technology enables the use of a large geothermal mass, which have not been previously exploited. Such thermal mass is generally present in hot dry rock (HDR) reservoirs, although the sufficient heat may be found in wet rocks as well.

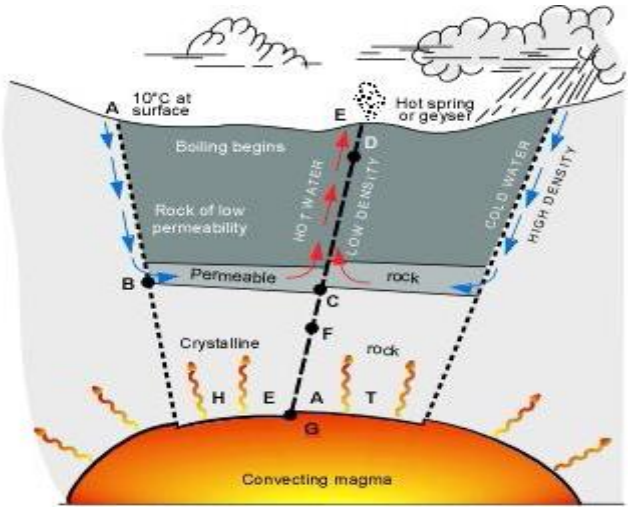

Figure 1.7 A simplified illustration of a geothermal system (White, 1973).

In EGS, the thermal energy of hot dry rock is extracted by pumping cold fluid into the deep rock through a well, performing 'hydraulic stimulation' by forcing the injected fluid to re-open the existing fractures (which enhances the hydraulic conductivity of the rock formation and increases the surface area over which heat exchange between the rock and the

fluid takes place), and finally recovering the heated fluid via a production well (Nathwani and Blackstock, 2012). Thus, a significant amount of thermal energy is transferred to the surface for use. The three-step process is a closed-loop cycle, which results in minimal use of water and other natural resources (Duchane, 1996). After the fluid delivers the energy via the production well, it is re-injected into the ground, and the cycle is repeated. The extracted energy is mainly used to generate electricity in most EGSs.

Similar to hydrothermal systems, the operation of EGS should be monitored in detail in order to achieve a highly efficient system. The main parameters that are required to be monitored are pressure and temperature of the geologic formations, subsurface seismic data to avoid micro-seismic events, and injection/production rates, which critically influence the function of the system. EGS systems based on HDR reservoirs are currently being developed and tested in France, Australia, Japan, Germany, the U.S.A., Switzerland, and the U.K. The largest EGS project in the world is currently being developed in the Cooper Basin, Australia with a potential to generate 5,000–10,000 MW of electricity (Grasby et al., 2012).

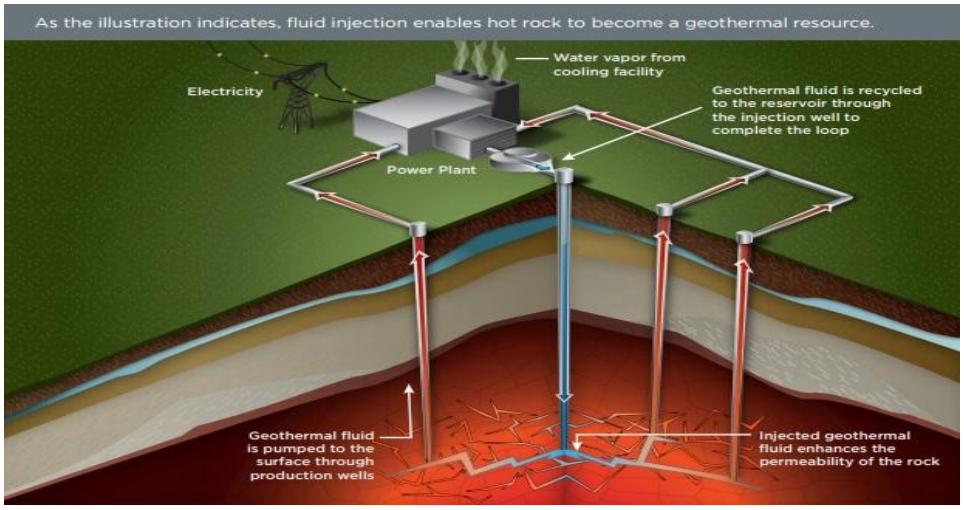

Figure 1.8 A visual model of an enhanced geothermal system (U.S. Department of Energy, Geothermal Technologies Office, 2013).

1.3 Research Motivation, Scope, and Objectives

Among the available geothermal heat extraction technologies, the EGSs are of particular interest because it is widely recognized as a universal system that can be installed anywhere in the world. EGS can result in energy security, reduction in air pollution, and local job creation (Nathwani et al., 2012). Generation of 1400 TWh of geothermal energy per year, which is possible by utilization of EGS, can avoid almost 800 Mt of CO_2 emissions (International Energy Agency, 2011). However, a major limitation in implementing EGS technology is the seismic events induced as a result of EGS operation. In fact, there is evidence in the literature of induced seismicity that led to a closure of an entire EGS project (Meier et al., 2015). The changes in the subsurface stress states because of hydraulic stimulation and heat flow results in shear slips along rock fractures and faults, and in creation of new fractures, which trigger micro-seismic events in the subsurface, which if not controlled may lead to bigger events and potential damage to the neighboring communities (Majer et al., 2007). Thus, it is necessary to investigate under what conditions pertaining to geomechanics seismic events are triggered during EGS operation, which is the central theme of this thesis.

The geomechanics of EGS involves coupled processes of fluid flow, thermal flow, and mechanical stress changes that must be modeled in an integrated framework to estimate the seismicity induced by an EGS operation (MIT, 2006). Such a thermo-hydro-mechanical (THM) system is often analyzed using the finite element method (Karahanoglu et al., 1984) that includes modeling of rock discontinuities so that potentials for shear slip caused by hydraulic stimulation and thermal flow can be estimated. However, to the author's knowledge, there is no study performed on estimating the seismic potential of an EGS

system through THM coupled approach. One quantitative study was performed to investigate the problem of induced seismicity in the subsurface, but none of these studies are directly concerned with EGS (Verdon et al., 2011). THM coupling analyses (Karahanoglu et al., 1984) found in the literature are mostly not related to induced seismicity, and in the few cases where these are related to induced seismicity (Rutqvist, 2013), the systems under investigation were not an EGS. The problem of induced seismicity in EGS has been the subject of study based mostly on case studies, seismic data analysis, and statistical approaches (Evans et al., 2012; Shapiro et al., 1997, 1999, 2002; Cornet, 2000; Rothert and Shapiro, 2003; Parotidis et al., 2004). Thus, there is a need for a comprehensive approach for numerical analysis of the EGS system using the coupled THM modeling to investigate EGS induced seismicity. This involves modeling of the formation stress-strain response, fluid flow through rock discontinuities, and thermal flow, and connecting the ensuing information to estimate slip potential along rock discontinuities. The scope of this research work is to develop such a modeling framework that integrates all these aspects of EGS.

The specific objectives of this research work are (i) to develop a two-dimensional finite element (FE) model of a typical subsurface profile consisting of a fractured zone surrounded by intact rock zones and consisting of a fault within the formation that can simulate fluid flow and thermal flow and estimate changes in the subsurface stress states, (ii) to use the subsurface stress information from the FE results to estimate slip potentials along the fault, and (iii) to identify the important parameters based on parametric studies that contribute to the induced seismicity.

The coupled THM finite element formulation was developed using the weighted residual approach (Reddy, 2006) and implemented by writing a user-defined code in

MATLAB (MathWorks, 2016). The Mohr-Coulomb failure criterion is used as a measurement for slip along the fault surface. Subsequently, a thorough parametric study is performed to identify the relative importance of the different parameters in generating potential slip along the fault surface.

1.4 Thesis Organization

This thesis is divided in four chapters. Chapter 1 provides a general introduction of the topic. Chapter 2 presents a detailed review of the literature consisting of previous research studies on geomechanics issues related to EGS systems and induced seismicity. Chapter 3 outlines the fundamental concepts and mathematical theories pertaining to EGS and related induced seismicity, and provides the details of the modeling studies performed in this research and the relevant results. Chapter 4 provides the main conclusions and suggestions for future studies.

CHAPTER 2 – Fundamentals and Literature Review

2.1 Overview

This chapter presents a brief overview of the fundamentals and existing literature on the geomechanics aspects of EGS. The specific topics discussed are the in situ stresses, thermo-hydro-mechanical coupling, hydraulic stimulation, and induced seismicity.

2.2 Salient Aspects of Geomechanics related to EGS

2.2.1 In situ Stresses

The state of stress in the geologic medium plays a critical role in the management of EGS setup. The in situ stresses have a direct effect on the drilling procedure, pressure required for reservoir stimulation, evolution of hydraulic conductivity, seismic potential of the subsurface, and fracture network (Ghassemi, 2012). The in situ stresses, in turn, are influenced by rock discontinuities, heterogeneities, and THM-coupled processes caused by injection/production (Ghassemi, 2012). Thus, knowledge of the in situ stress state is essential in developing and managing an EGS system. Depending on the tectonic characteristics of the geological formation, two in situ stress regimes are usually observed – either the vertical stress is greater than the horizontal stress (in which case, the vertical stress is considered to be the major principal stress σ_1 and the horizontal stresses are the intermediate and minor principal stresses σ_2 and σ_3, respectively) or one of the horizontal stresses is greater than the vertical stress (in which case, the greater horizontal stress is σ_1, and the vertical and the lower horizontal stresses can be σ_2 and σ_3 or vice versa). These stress regimes may have an impact on the THM coupled process (Rutqvis et al., 2007) that governs the EGS system.

2.2.2 Thermo-Hydro-Mechanical (THM) Coupling

The operation of an EGS is governed by changes in the temperature field, fluid pressure distribution, and mechanical deformations and stresses in the subsurface medium. The THM coupled processes result in opening of preexisting fractures and creation of new fractures that increase the hydraulic conductivity of the formation. When a fractured medium is established with the aid of induced and pre-existing natural faults, it needs to be carefully monitored and analyzed for potential induced seismicity in order to achieve an efficient geothermal system with high flow rate.

Linking the thermal, hydraulic, and mechanical aspects of geomechanics began with the theories of Terzaghi and Biot (Terzaghi, 1925; Biot, 1956). Terzaghi introduced the concept of effective stress, which considers the effect of pore fluid pressure on the stress state in the subsurface. If an elastic constitutive relationship is used to describe the stress-strain relation in the medium while considering the fluid flow equation and changes in pore pressure, the analysis is said to be based on poro-elasticity. However, the term poro-elasticity was not used until Biot improved Terzaghi's theory to include the compressibility of the elastic medium. Biot also considered the effect of temperature changes on the stress field, thereby initiating one of the very first approaches of thermo-poro-elasticity.

As a necessary element to face in geosciences and geoenvironmental studies, THM coupling has been a point of interest in analyzing wide range of geomechanical problems such as disposal of radioactive wastes (Selvadurai and Nguyen; 1997, Gnirk, 1993), energy piles and ground source energy extraction (Knellwolf et al., 2011; Laloui and Di Donna, 2011), and geothermal energy extraction (Dickson and Fanelli, 1995; Duffield and Sass, 2003, Karahanoglu et al., 1984). Although THM coupling in context of geothermal energy

has been studied, a few of these studies are linked with EGS in particular (Cao et al., 2015). Another important issue is that a few of THM coupling analyses in the literature are concerned with problem of induced seismicity and discontinuity analysis (Selvadurai and Nguyen, 1995, Rutqvist, and Stephansson, 2003, Rutqvist et al., 2013). Therefore, a complete study where the main focus is on EGS and the problem of induced seismicity analysis is achieved by using THM coupling is required.

2.2.3 Hydraulic Stimulation

The low permeability reservoir in an EGS necessitates an effective fluid injection operation in order to establish a permeable fracture network. The fluid injection opens up the preexisting rock discontinuities and creates new discontinuities by hydraulic fracturing. This process is called hydraulic stimulation, and it is the key process deciding the efficiency of an EGS.

The first numerical simulations of geothermal systems considered hydrothermal effects while generally neglecting rock mechanics aspects (GEOCRACK:Swenson et al. 1997; Hopkirk et al., 1981, Kohl et al., 1995). Previous studies by Sesetty and Ghassemi (2012), Weng et al. (2011), Zhang and Jeffrey (2006), and Koshelev and Ghassemi (2003) are good examples of advancements and achievements gained in this research area. However, these early elastic models do not focus on fracture propagation and interaction. Other approaches have used complex and real variable boundary element methods (Olson, 2008; Dobroskok et al., 2005; Bobet & Einstein, 1998) to model fracture interactions. Poroelastic and thermoelastic displacement discontinuity methods (Zhou & Ghassemi, 2011; Ghassemi & Zhou, 2011; Ghassemi & Roegiers, 1996; Carter et al., 2000); finite element method (FEM) (Boone et al., 1991); and extended finite element method (XFEM) (Yazid et

al., 2009) were also introduced. The newer studies of hydraulic stimulation in a geological subsurface are mainly limited to small-scale analysis of crack growth, fracture propagation, and near well-bore interactions (Ghassemi, 2012).

2.2.4 Induced Seismicity

Induced seismicity is generally defined as a series of micro-seismic events which are caused artificially by human activities. The pore pressure increase and temperature decrease, resulting from cold fluid injection in an EGS setup, can lead to rock failure in shear or shear slip on new or pre-existing fracture planes (Majer et al., 2007). Thermo-poro-mechanical processes have an impact on large-scale stress state and also on fracture network in small-scale, with both being capable of triggering micro-seismic events. Therefore, mathematical studies regarding induced seismicity are usually linked with analysis of THM and hydraulic fracturing (HF) processes (Rutqvist et al., 2013).

Proliferation of micro-seismic activities may lead to larger seismic events (De Pater and Baisch, 2011), which are at times felt on the surface (Haring et al, 2008). Therefore, investigation of seismic risk potential is necessary for an EGS setup development. However, a relationship has not yet been established between micro-seismic potential and EGS-related activities such as fluid flow in the subsurface and injection rates, though it is definitely clear that seismic activities in geothermal fields are associated with injection/production operation (Majer et al., 2007; Das and Zoback, 2011). Qualitative and quantitative studies on induced seismicity usually deal with investigation of micro-seismic events based on monitoring of seismic data (seismicity-based reservoir characterization), such as the review of 41 European case histories by Evans et al., 2012, to predict the behavior of an EGS system (Shapiro et al. 1997, 1999, 2002; Cornet 2000; Rothert and Shapiro 2003; Parotidis et al. 2004).

Mathematical analyses of induced seismicity in a geologic medium has been a subject of few studies such as Verdon et al., 2011, and Rutqvist et al., 2015, although in none of them EGS is the geoenvironmental system under investigation. The former is concerned with induced seismicity in CO_2 storage layers and the latter is dealing with shale-gas reservoirs.

2.2.5 Concluding Remarks

Although each of the geomechanics aspects mentioned in this chapter has been subject of numerous studies, but there are a few approaches in which all of them are gathered in an integrated study. THM coupling analyses are mostly not linked with the problem of induced seismicity, and in the few cases where both are considered, the system under investigation is not an EGS. EGS studies available in the literature are mainly limited to seismicity-based reservoir characterizations. In this thesis, the target is to come up with a model which covers all of these aspects and provides with a complete analysis of an EGS.

CHAPTER 3 – Analysis and Results

3.1 Synopsis

In this thesis, a THM coupled analysis of a geological medium representing an EGS system is provided. Instead of modeling the fracture initiation and crack growth as a result of hydraulic stimulation, a specific section of the medium is assumed to possess higher hydraulic conductivity, which forms the basis of the EGS system. A pre-existing fault is assumed to be located near the injection zone. This fault meets the high permeability zone and therefore gets affected by EGS operation, expressing potential of seismic activity as a result. A two-dimensional plain strain analysis is performed using Finite element method (FEM) to obtain pressure, temperature and stress changes in fault as a result of EGS system. The concept of fracture potential (Eckert, 2007) in shear regime is then used to mathematically investigate induced seismicity in the fault. The basic theory and governing equations of geological subsurface medium, along with FE formulation and numerical solution procedure of fully coupled THM analysis are given. FE formulation used in the code written using MATLAB commercial code is verified against several benchmark problems (Timoschenko, 1941; Terzaghi, 1925; Mandel, 1953; Selvadurai and Nguyen, 1995; Crank, 1975; Carter, 1989). Finally, a parametric study is performed investigating the effect of different parameters on induced seismicity potential of an EGS and the results are presented.

3.2 Governing Equations

3.2.1 Stress-Strain Constitutive Relationship and Theory of Thermo-poro-elasticity

Assuming that both the solid and fluid phases exist in every point of the subsurface poro-elastic medium, the total stress tensor σ_{ij} in non-isothermal condition can be expressed as (Selvadurai and Nguyen, 1995):

$$\sigma_{ij} = 2\mu\varepsilon_{ij} + \lambda\varepsilon_{kk} - \alpha_b p\delta_{ij} - 3K_D\alpha_s\Delta T\delta_{ij} \tag{3.1}$$

where ε_{ij} is the infinitesimal strain tensor, δ_{ij} is the Kronecker delta, p is the pore pressure (i.e., the pressure in the fluid present in the poro-elastic medium), T is temperature, μ and λ are Lame's constants, K_D is the bulk modulus of the porous skeleton, α_s is linear thermal expansion coefficient of the solid formation and α_b is Biot's coefficient (Biot, 1941) given by

$$\alpha_b = 1 - \frac{K_D}{K_S} \tag{3.2}$$

where K_s is the bulk modulus of solid formation. Although the value of α_b has been point of argue (Selvadurai and Nguyen, 1995), in most geomechanical applications, based on the fact that K_s is significantly higher comparing to K_D, α_b is assumed to be equal to 1.

The strain tensor for small deformations used in this analysis is given by

$$\varepsilon_{ij} = \frac{1}{2}\left(\frac{\partial u_i}{\partial x_j} + \frac{\partial u_j}{\partial x_i}\right) \tag{3.3}$$

where u_i is the displacement vector and x_j is the spatial coordinate in two dimensions.

The equation of equilibrium in terms of total stress is expressed as

$$\frac{\partial \sigma_{ij}}{\partial x_j} + b_i = 0 \tag{3.4}$$

where b_i represents the body force. Combination of equation (3.1) and equation (3.4) gives the governing equation of isotropic thermo-poro-elastic geological medium in the absence of body forces and gravity effects:

$$\mu \frac{\partial^2 u_i}{\partial x_i \partial x_j} + (\mu + \lambda) \frac{\partial^2 u_j}{\partial x_i \partial x_j} - \alpha_b \frac{\partial p}{\partial x_i} - 3K_D \alpha_s \frac{\partial T}{\partial x_i} = 0 \tag{3.5}$$

3.2.2 Fluid Flow

Darcy's law for fluid flow is applicable to a wide range of geological processes in both soils and rocks. The generalized form of Darcy's Law can be expressed as follows (Selvadurai and Nguyen, 1995; Verruijt, 1969):

$$V_{if} - V_{is} = \frac{k_{ij}}{\eta} \left(\frac{\partial p}{\partial x_j} \right) \tag{3.6}$$

where V_{if} is the fluid velocity in the pore spaces in the subsurface, V_{is} is the fluid velocity in the porous skeleton of the geologic medium, k_{ij} is permeability, and η is dynamic viscosity. The difference between intrinsic permeability (k_{ij}) and hydraulic conductivity (K_{ij}) should be noted. Permeability is not dependent on the fluid, whereas hydraulic conductivity is a function of fluid dynamic viscosity and fluid density. Both these terms are used in the literature to describe Darcy's Law. The relationship between these two parameters are given as

$$\mathrm{K}_{ij} = \frac{\rho_f g}{\mu} k_{ij} \tag{3.7}$$

where ρ_f is the density of the fluid.

The governing equation of fluid flow through porous media starts by considering a control volume. In the volumetric element, the principle of mass conservation indicates that

the excess of in-flow over out-flow during a small period of time through the surfaces of the control volume in all directions should be equal to the change of mass within the control volume during the same time range (Bear, 1972). Neglecting the dispersion caused by fluctuation in velocity, mass flux can be written as:

$$J = \rho_f q \tag{3.8}$$

where q is the flux (discharge per unit area), defined as:

$$q = n(V_{if} - V_{is}) \tag{3.9}$$

where n is porosity. The rate of change in mass is represented by the change in fluid density and porosity $\frac{\partial(n\rho_f)}{\partial t}$. This gives:

$$-\frac{\partial}{\partial x_i}(\rho_f n(V_{if} - V_{is})) = \frac{\partial(n\rho_f)}{\partial t} \tag{3.10}$$

The right hand side of equation (3.10) can be written as:

$$\frac{\partial(n\rho_f)}{\partial t} = n\frac{\partial \rho_f}{\partial t} + \rho_f \frac{\partial n}{\partial t} \tag{3.11}$$

The density is a function of pressure and temperature, and the infinitesimal change in density can be written as:

$$d\rho_f = -\rho_f \left(\frac{dp}{K_f} + 3\alpha_f dT \right) \tag{3.12}$$

where K_f is the bulk modulus of the fluid and α_f is linear thermal expansion coefficient of the fluid. In order to proceed with the derivation, the Bishop Method (Bishop, 1973) is used. In this method, the variation in volume of an elemental volume V is considered as the combination of total stress increment $d\sigma_{ij}$ and temperature increment dT, where the total stress increment is itself divided into effective stress increment $d\sigma'_{ij}$ and pore fluid pressure

increment dp. The average increment of σ'_{ij} acting on the solid is assumed to be $d\sigma'_{ij}/(1-n)$ in the plane of area A that intersects the element and acts on the solid, since the area of solid in the plane is assumed to be $(1-n)\,\mathrm{A}$. Therefore, the changes of total volume and volume of solids are respectively $\mathrm{V}\dfrac{dp}{3K_s}$ and $(1-n)\,\mathrm{V}\dfrac{dp}{3K_s}$ due to dp, $\mathrm{V}\dfrac{d\sigma'_{kk}}{3K_D}$ and $\mathrm{V}\dfrac{d\sigma'_{kk}}{3K_S}$ due to $d\sigma'_{ij}$, and $3\mathrm{V}\alpha_e dT$ and $3(1-n)V\alpha_s dT$ due to dT where α_e is the linear thermal expansion coefficient if the drained material. The change in pore volume can be defined as the difference between the change in total volume and the change in solid volume:

$$d\,\mathrm{V}_f = d\,\mathrm{V} - d\,\mathrm{V}_s \tag{3.13}$$

Therefore:

$$d\,\mathrm{V}_f = \mathrm{V}\left(\frac{ndp}{K_S} + \left(\frac{1}{K_D} - \frac{1}{K_S}\right)\frac{d\sigma'_{kk}}{3} + [3\alpha_e - 3(1-n)\alpha_s]dT\right) \tag{3.14}$$

By definition:

$$dn = \frac{d\,\mathrm{V}_f}{\mathrm{V}} \tag{3.15}$$

And from the equilibrium equation:

$$d\sigma'_{kk} = 3K_D\left(d\varepsilon_{kk} - \frac{dp}{K_S} - 3\alpha_e dT\right) \tag{3.16}$$

Therefore:

$$dn = \left(\frac{(n-\alpha_b)dp}{K_S} + \alpha_b d\varepsilon_{kk} + [(1-\alpha)3\alpha_e - (1-n)3\alpha_s]dT\right) \tag{3.17}$$

From equations (3.11), (3.12), and (3.17), the right hand side of equation (3.10) can be written as

$$\frac{\partial(n\rho_f)}{\partial t} = \rho_f \left[-\left(\frac{n}{K_f} - \frac{n}{K_S} + \frac{\alpha_b}{K_S} \right) \frac{\partial p}{\partial t} + \alpha_b \frac{\partial \varepsilon_{kk}}{\partial t} + [3(1-\alpha_b)\alpha_e - 3(1-n)\alpha_s - 3\mathrm{n}\,\alpha_f] \frac{\partial T}{\partial t} \right] \tag{3.18}$$

It is assumed that:

$$\frac{\partial}{\partial x_i}(\rho_f n(V_{if} - V_{is})) = \rho_f \frac{\partial(n(V_{if} - V_{is}))}{\partial x_i} \tag{3.19}$$

From Darcy's law (equation (3.10)) and equations (3.18) and (3.19), the complete form of the governing equation of fluid flow in a porous medium is obtained as:

$$\frac{\partial}{\partial x_i}\left(\frac{k_i}{\eta}\left(\frac{\partial p}{\partial x_j} \right) \right) - \left(\frac{n}{K_f} - \frac{n}{K_s} + \frac{\alpha_b}{K_s} \right) \frac{\partial p}{\partial t} + \alpha_b \frac{\partial}{\partial t} \frac{\partial u_i}{\partial x_i} + [3(1-\alpha_b)\alpha_e - 3((1-n)\alpha_s - 3\mathrm{n}\,\alpha_f] \frac{\partial T}{\partial t} = 0 \tag{3.20}$$

In this research study, the effect of ∂T on the rate of density and porosity change is not included for the sake of simplicity. In other words, $\frac{\partial T}{\partial t}$ disappears and equation (3.20) is changed to:

$$\frac{\partial}{\partial x_i}\left(\frac{k_{ij}}{\eta}\left(\frac{\partial p}{\partial x_j} \right) \right) - \left(\frac{n}{K_f} - \frac{n}{K_S} + \frac{\alpha_b}{K_S} \right) \frac{\partial p}{\partial t} + \alpha_b \frac{\partial}{\partial t} \frac{\partial u_i}{\partial x_i} = 0 \tag{3.21}$$

As mentioned before, the terms including $\frac{1}{K_S}$ are neglected since K_s is significantly high. Defining $\beta = \frac{1}{K_f}$ as fluid compressibility results in

$$\frac{\partial}{\partial x_i}\left(\frac{k_{ij}}{\eta}\left(\frac{\partial p}{\partial x_j} \right) \right) - n\beta \frac{\partial p}{\partial t} + \alpha_b \frac{\partial}{\partial t} \frac{\partial u_i}{\partial x_i} = 0 \tag{3.22}$$

To account for inflow or outflow of the fluid per unit volume of the solid, the term $\frac{\partial Q_e}{\partial t}$ is added to the above equation:

$$\frac{\partial}{\partial x_i}\left(\frac{k_{ij}}{\eta}\left(\frac{\partial p}{\partial x_j}\right)\right)-n\beta\frac{\partial p}{\partial t}+\alpha_b\frac{\partial}{\partial t}\frac{\partial u_i}{\partial x_i}+\frac{\partial Q_e}{\partial t}=0 \tag{3.23}$$

3.2.3 Heat Transfer

Heat transfer in porous media is governed by heat conduction and heat convection. Conductive heat transfer takes place in the particles of porous medium without the mass movement, whereas the bulk movement is the main reason for convective heat flow. The heat transfer governing equation is derived using the concept of energy balance where the rate of energy accumulation should be equal to the excess flow of energy in a control volume of the medium. The excess flow due to diffusion results in conductive heat flow and the excess flow due to advection results in convective heat flow. The rate of energy accumulation is defined as the rate of change in thermal energy multiplied by the mass of the medium. Detailed derivation of heat transfer in porous media can be found in Combarnous and Bories (1975) and Lewis (1986). The final form of the governing equation of heat transfer is given by:

$$-\frac{\partial}{\partial x_i}\left(\kappa_{ij}\frac{\partial T}{\partial x_j}\right)+\rho_e C_e\frac{\partial T}{\partial t}+\rho_f C_f\overline{V}\frac{\partial T}{\partial x_i}-\frac{\partial Q_h}{\partial t}=0 \tag{3.24}$$

where κ_{ij} is the thermal conductivity of the medium, $\overline{V}$ is relative Darcy's velocity, Q_h is the out flow of heat per unit volume, ρ_e and C_e are respectively the effective values of mass density and heat capacity of the geological medium, which are the weighted average of the solid and fluid phases as determined by the porosity: $\rho_e C_e = n\rho_f C_f + (1-n)\rho_s C_s$ (subscript *s* stands for the solid phase and subscript *f* stands for the fluid phase).

3.3 Finite Element Formulation

The weighted residual approach along with Galerkin's method (Vaziri, 1988; Sandhu and Wilson, 1969; Ghaboussi and Wilson, 1973; Aboustit et al., 1985) is applied to equations (3.5), (3.23), and (3.24) to develop the finite element formulation. The two-dimensional domain is discretized into a set of nodes and elements. Each node is characterized by four primary unknown variables: nodal displacements in two directions, pore pressure, and temperature. The porous media is discretized by eight-noded quadrilateral (Q8) elements, where all the unknowns in each element are represented as a function of values of unknowns for all eight nodes. In an isoparametric coordinate with axes *s* and *t* (horizontal and vertical respectively), the shape functions for the Q8 elements are defined as

$$N_1(s,t) = \frac{1}{4}(1-s)(1-t)(-s-t-1) \quad \text{(i)}$$

$$N_2(s,t) = \frac{1}{4}(1+s)(1-t)(s-t-1) \quad \text{(ii)}$$

$$N_3(s,t) = \frac{1}{4}(1+s)(1+t)(s+t-1) \quad \text{(iii)}$$

$$N_4(s,t) = \frac{1}{4}(1+s)(1+t)(-s+t-1) \quad \text{(iv)}$$

$$N_5(s,t) = \frac{1}{2}(1-t)(1+s)(1-s) \quad \text{(v)}$$

$$N_6(s,t) = \frac{1}{2}(1-t)(1+t)(1+s) \quad \text{(vi)}$$

$$N_7(s,t) = \frac{1}{2}(1+t)(1+s)(1-s) \quad \text{(vii)}$$

$$N_8(s,t) = \frac{1}{2}(1-s)(1+t)(1-t) \quad \text{(viii)}$$

Finite difference scheme is used to numerically integrate the system of differential equations in time. Time-dependent functions are assumed to vary linearly between former and latter time step, therefore time-derivative terms are approximated by a first-order incremental ratio. Considering above shape functions for describing displacements, pore pressure, and temperature, respectively denoted as N_u , N_p , and N_T along with their derivatives denoted as B_u , B_p , B_T , the final matrix form of the system of equations following the application of the finite difference time integration scheme is:

$$\begin{bmatrix} K & -Q & -X \\ -Q^T & -S-R\theta\Delta t & 0 \\ 0 & 0 & -TS-TR\theta\Delta t \end{bmatrix} \begin{bmatrix} \tilde{u}^{t+\Delta t} \\ \tilde{p}^{t+\Delta t} \\ \tilde{T}^{t+\Delta t} \end{bmatrix} = \begin{bmatrix} K & -Q & -X \\ -Q^T & -S-R(\theta-1)\Delta t & 0 \\ 0 & 0 & -TS-TR(\theta-1)\Delta t \end{bmatrix} \begin{bmatrix} \tilde{u}^{t} \\ \tilde{p}^{t} \\ \tilde{T}^{t} \end{bmatrix} + \begin{bmatrix} f^{(u)} \\ f^{(p)} \\ f^{(T)} \end{bmatrix} \Delta t \tag{3.25}$$

where the definition of matrices are

$$K = \int B_u{}^T D B_u d\Omega \tag{a}$$

$$Q = \int B_u{}^T \alpha_b \delta N_p d\Omega \tag{b}$$

$$X = \int B_u{}^T \frac{E\alpha_s}{(1-2\nu)} \delta N_T d\Omega \tag{c}$$

$$S = \int N_p{}^T n\beta N_p d\Omega \tag{d}$$

$$R = \int B_p{}^T \frac{k}{\eta} B_p d\Omega \tag{e}$$

$$TS = \int N_T{}^T \rho_e C_e N_T d\Omega \tag{f}$$

$$TR = \int B_T{}^T \kappa B_T d\Omega + \int B_T{}^T \rho_f C_f \bar{V} N_T d\Omega \tag{g}$$

$$f^{(u)} = \int N_u{}^T \bar{t}_N d\Gamma + \int N_u{}^T b d\Omega \tag{h}$$

$$f^{(p)} = \int N_p{}^T q_p d\Gamma + \frac{\partial}{\partial t}\int N_p{}^T Q_e d\Omega \tag{i}$$

$$f^{(T)} = \int N_T{}^T q_T d\Gamma + \frac{\partial}{\partial t}\int N_T{}^T Q_h d\Omega \tag{j}$$

where θ is an arbitrary value between 0 and 1, usually selected to be equal to 1 to achieve an implicit scheme. The stress-strain relationship is defined as

$$\begin{bmatrix} \sigma_{xx} \\ \sigma_{yy} \\ \tau_{xy} \end{bmatrix} = \begin{bmatrix} D_{11} & D_{12} & D_{13} \\ D_{21} & D_{22} & D_{23} \\ D_{31} & D_{32} & D_{33} \end{bmatrix} \begin{bmatrix} \varepsilon_{xx} \\ \varepsilon_{yy} \\ 2\gamma_{xy} \end{bmatrix} \tag{3.26}$$

where D is the constitutive matrix, components of which in plane strain condition are as follows

$$D = \frac{E}{(1+\nu)(1-2\nu)} \begin{bmatrix} 1-\nu & \nu & 0 \\ \nu & 1-\nu & 0 \\ 0 & 0 & 1-2\nu/2 \end{bmatrix} \tag{3.27}$$

Equations (3.5), (3.23), and (3.24) that describe a THM (thermo-hydro-mechanical) coupled problem may be solved simultaneously as a system of equations in order to obtain solutions to well-posed boundary value THM problems. Therefore, with knowledge of initial and boundary conditions (traction forces, fluid flow, heat flux, initial temperature, pore pressure, and displacements), the equations can be solved in each time step (Figure 3.1).

To simplify the model, some assumptions are made. Permeability, porosity, and density of the medium and the fluid do not change during the operation. Furthermore, a fault already exists in the model. The effect of temperature change on pore pressure distribution is not considered. Each of these constraints can be relaxed at the expense of a more complex, non-linear model as well as computational penalties (execution time and convergence issues).

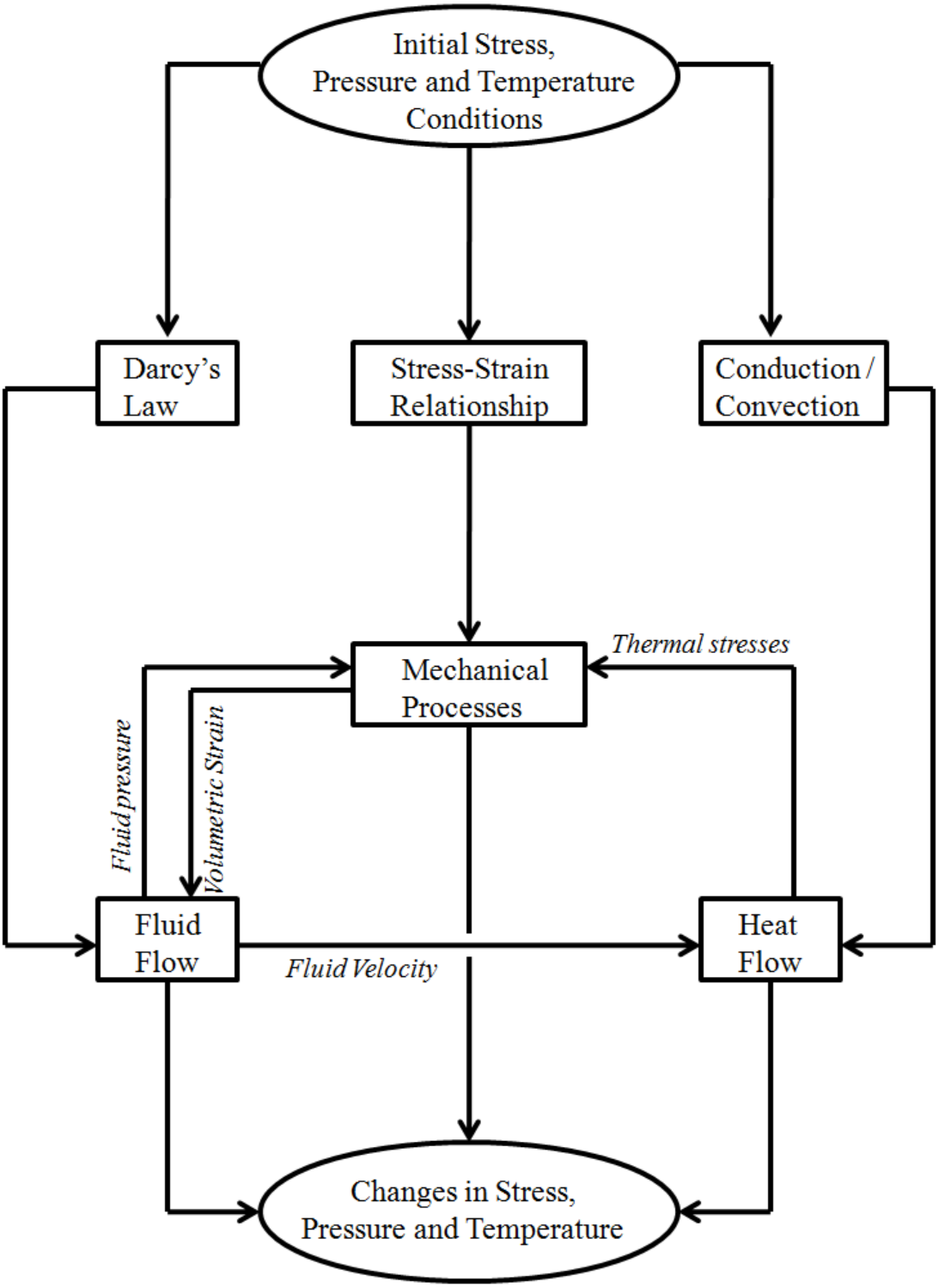

Figure 3.1 Structure of the FE model

Fault elements are also represented by solid elements in this study. Although numerous methods can be used in order to come up with more complex modeling of the fault, it was found that for the sake of what this research aims to achieve, using solid elements is acceptable for the main objectives of this work. Detailed explanation of how this point is concluded is presented in the analysis section.

Convergence of the FE code results are checked by calculating results in different time steps and meshes. Because the order of the answers expected to be observed is known, and also because the code is fully coupled and there is no iteration in calculating primary variables, the convergence process is not included in the code as a separate section.

3.4 Induced Seismicity Estimation Approach

Injection or extraction of fluid into or from a permeable rock induces not only a pore-pressure change in the reservoir, but also causes stress redistribution in the reservoir and in the surrounding formation. The mechanism of this process is shown in Figure 3.3, where a hydraulically induced stress redistribution is considered, occurring as a result of injection of a finite volume of fluid into a porous elastic sphere surrounded by a large relatively impermeable elastic body. This leads to pore pressure increase inside the sphere. Also, stress redistribution occurs because of expansion of the injection zone. The magnitude of the induced pore pressure depends on the rate of fluid injection, the total volume injected, permeability of the formation, storage coefficient, and fluid viscosity. An important point is that inducing a seismic activity can take place by either increasing or decreasing pore pressure with respect to the existing pore pressure. Also, the region in which the change in pore pressure occurs should be large enough to encompass the fault area so that fault gets

activated. Therefore, induced seismicity in a geothermal reservoir is associated with shear slip along pre-existing faults and activated fracture networks (Scholz, 1990).

In order to mathematically examine the shear slip, the Mohr-Coulomb criterion is usually used, in which the maximum shear stress that the fault can tolerate in is linked to the effective normal stress (σ_n') on a fault through its cohesion (c) and effective friction angle (ϕ):

$$\tau = c + \sigma_n' \tan\phi \tag{3.28}$$

where

$$\sigma_n' = \sigma_n - p \tag{3.29}$$

Using this criterion, the maximum possible pressure increase without shear slip occurrence can be roughly estimated. However, since thermo-poro-elastic effects are not considered in this first-order estimation, the actual value may be different. Figure 3.2 shows how pressure increase alone is illustrated in the Mohr-Coulomb diagram. However, Figure 3.3 shows what happens in presence of coupled processes, which may cause shear slip with a lesser value of pressure increase. To study shear slip potential, which is directly related to the state of Mohr circle with respect to the failure envelope, evolution of stress state should be observed during a specific time period after stimulation program.

The criterion shows only whether the failure has occurred or not, without being able to present the trend of the stress evolution or explaining how far different locations on the fault are from reaching to the failure level. Therefore, in order to introduce a measure for evaluating the likelihood of shear slip in each time step apart from the actual failure, the concept of fracture potential should also be introduced.

The fracture potential in shear regime (Verdon, 2011; Eckert, 2007) is defined as

$$\text{sFP} = \frac{\sigma'_d / 2}{\sigma'_{d,crit} / 2} \tag{3.30}$$

where σ_d and $\sigma_{d,crit}$ are respectively the actual and critical differential stresses (Figure 3.4):

$$\sigma'_d = \sigma'_1 - \sigma'_3 \tag{3.31}$$

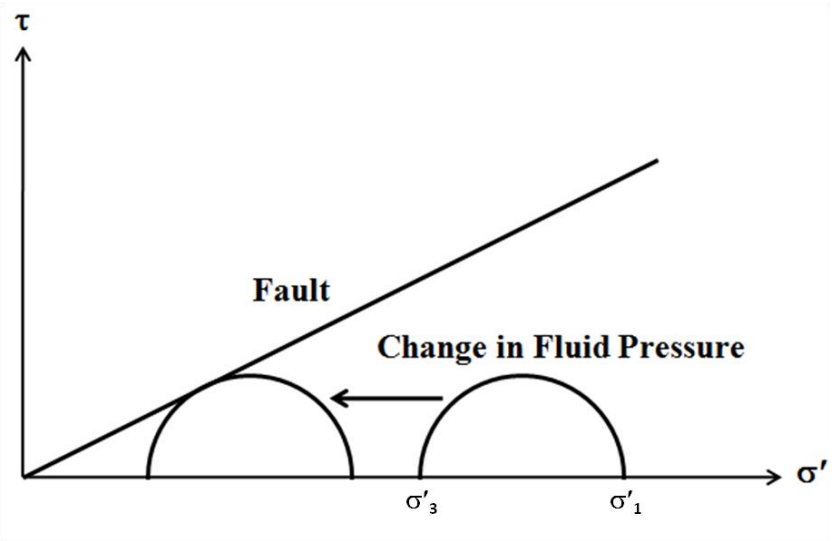

Figure 3.2 Changes in 2D Mohr circle as a result of pressure increase.

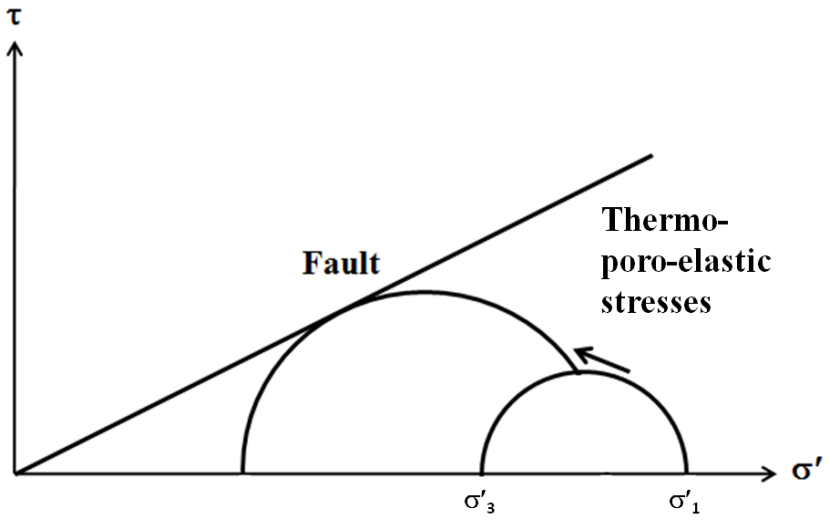

Figure 3.3 Changes in Mohr circle as a result of thermal or poro-elastic stresses in case of moving towards failure.

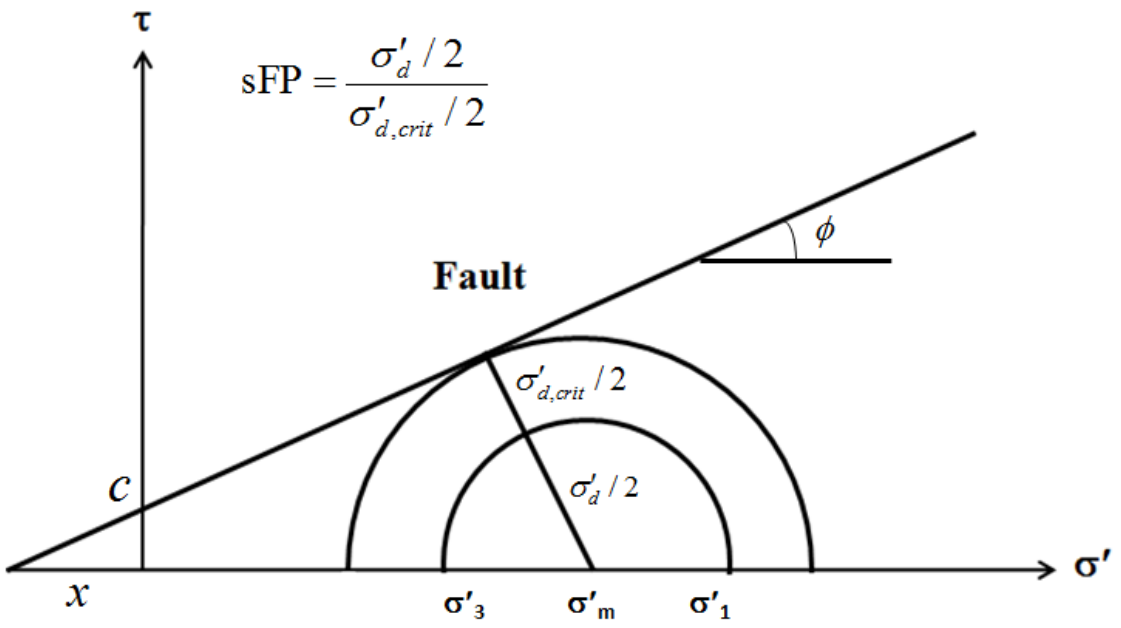

Figure 3.4 Shear fracture potential definition on Mohr-Coulomb diagram (Eckert, 2007).

From the diagram, $\sigma_{d,crit}$ can be written as a function of principal stresses and fault characteristics. Since $\sin\phi = \frac{\sigma'_{d,crit}/2}{x + \sigma'_m}$ and $x = \frac{c}{\tan\phi}$:

$$\frac{\sigma'_{d,crit}}{2} = (\frac{c}{\tan\phi} + \sigma'_m)\sin\phi = C\cos\phi + \sigma'_m \sin\phi \tag{3.32}$$

Therefore:

$$\mathrm{sFP} = \frac{\sigma'_d}{2(c\cos\phi + \sigma'_m \sin\phi)} \tag{3.33}$$

Therefore, understanding the values of principal stresses in enough to obtain Mohr-Coulomb diagram in each point and calculate the value of sFP. Initial horizontal and vertical effective stresses are considered principal stresses in the beginning (Chapter 2). Thus, no initial shear stress is considered before starting the injection process. Injection process results in pressure increase and therefore the total stress increases, but there will be a noticeable drop in

horizontal and vertical effective stresses. Also, there will be an induced shear stress in the medium. In order to measure *sFP* at each time step, the changes in horizontal and vertical effective stresses, and also the shear stress occurred as a result of injection are obtained and new values for principal stresses are calculated using these famous formulas:

$$\sigma'_1 = \frac{\sigma'_y + \sigma'_x}{2} + \sqrt{(\frac{\sigma'_y - \sigma'_x}{2})^2 + \tau^2_{xy}}$$
$$\sigma'_3 = \frac{\sigma'_y + \sigma'_x}{2} - \sqrt{(\frac{\sigma'_y - \sigma'_x}{2})^2 + \tau^2_{xy}} \quad (3.34)$$

Depending on how horizontal and vertical effective stresses change, and how much shear stress in induced, new principal stresses are determined and therefore in each time step, Mohr-Coulomb diagram is available, making it capable to calculate shear fracture potential as a result.

3.5 FE Code Verification

In order to verify the code and finite element formulation of thermo-hydro-mechanical governing equations, it is used to solve benchmark problems and compare the accepted results and the results obtained from FE code. These accepted results are mostly analytical solutions, except in one case where the accepted result is generated from a well-known numerical analysis software. This is mainly because it is difficult to get field data in subsurface activities such as the one proposed in this study. Each of these problems includes at least one of the three fundamental governing equations. The selection of problems has been done in such a way that at the end of this section, all parts of the solution matrix are investigated at least once, in order to guarantee the authenticity of FE code.

3.5.1 Elasticity

In this section, stress function concept is used to verify elastic equilibrium equation. The model used in this section is a cantilever beam with a concentrated shear force applied to its edge, geometry of which can be observed in Figure 3.5. Analytical solution for stress field through the beam length is provided in Timoschenko, 1941. Also, a widely-known formula exists for beam deflection profile. Basically, the analytical results derived from beam theory are compared to the results obtained from the code. The comparisons are presented in Figure3.6 and 3.7. Results should match along the beam profile except near the fixed edge. For a beam with conditions and coordinates similar to what shown in Figure 3.5, stress distribution and deflection are given as:

$$\sigma_{xx} = \frac{3F}{2b^3} xy \tag{i}$$

$$\sigma_{yy} = 0 \tag{ii}$$

$$\sigma_{xy} = \frac{3F}{4b^3}(b^2 - y^2) \tag{iii}$$

$$dv = \frac{F(2L + x)(L - x)^2}{6EI} \tag{iv}$$

where

$$I = \frac{2b^3}{3} \tag{v}$$

Input parameters used for this section are provided in Table 3.1. Figure 3.6 shows that FE code and analytical results for beam deflection are the same. Figure 3.7 shows that results obtained for stress components from FE code match well with the analytical solution.

Figure 3.5 Geometry of the elasticity problem

Table 3.1 Properties used for elasticity problem

$F(N)$	L(m)	b(m)	E(Pa)
8000	8	0.5	3×10^{7}

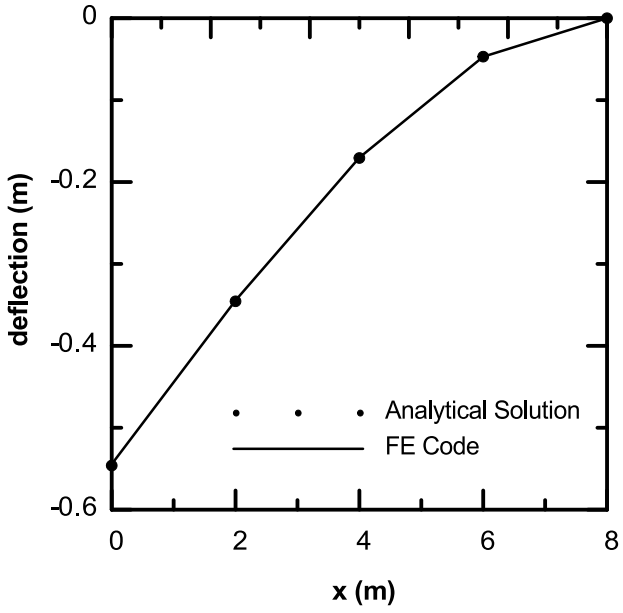

Figure 3.6 Beam deflection results (Maximum percentage error=0.36%)

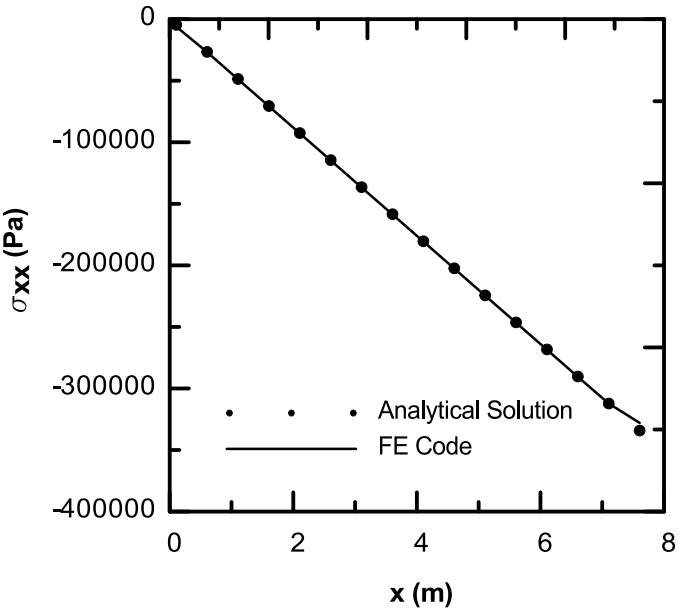

Figure 3.7.a Comparison of results obtained for horizontal stress field along the middle of the beam where y=0.0422m (Maximum percentage error=0.71%). The area near the beam support is excluded since stress function is valid everywhere except near supports.

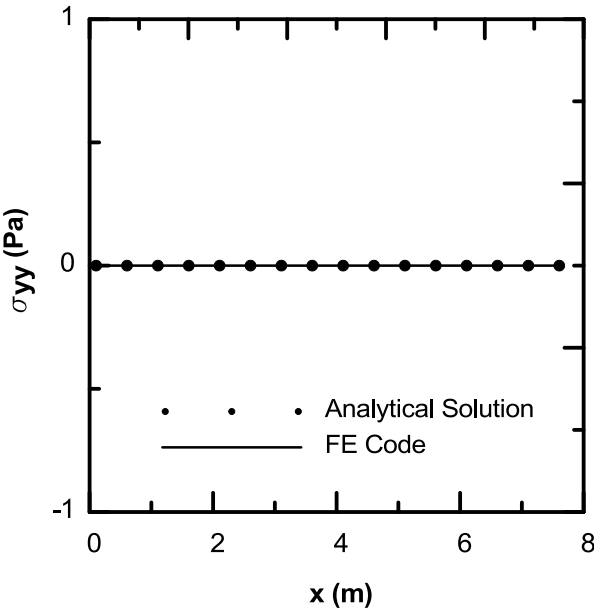

Figure 3.7.b Comparison of results obtained for stress fields along the middle of the beam where y=0.0422m. The area near the beam support is excluded since stress function is valid everywhere except near supports

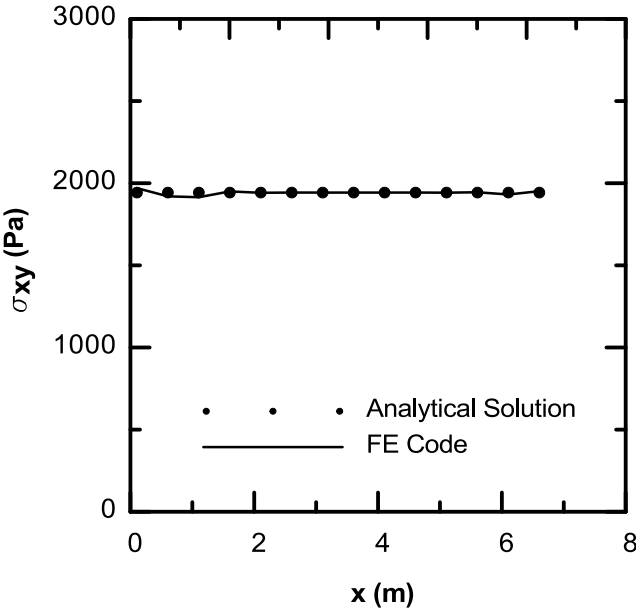

Figure 3.7.c Comparison of results obtained for stress fields along the middle of the beam where y=0.0422m (Maximum percentage error=1.39%). The area near the beam support is excluded since stress function is valid everywhere except near supports

3.5.2 Fluid Flow and Poroelasticity

In this section, the widely known 1D Terzaghi's problem and 2D Mandel's problem are investigated in order to check the accuracy of pressure-displacement coupling. After these two benchmark problems, the code is also verified against a case similar to a real-life application of poro-elasticity concept presented by Selvadurai and Nguyen, 1995. The input parameters used to verify the FE code against Terzaghi and Mandel's problem are provided in Table 3.2. Table 3.3 shows the input values used for verifying FE code for the third problem. In all three problems, the density of fluid is 1000 kg/m^3 and acceleration due to gravity is considered equal to 9.81 m/s^2 throughout the whole analysis.

Terzaghi's 1D problem (Terzaghi, 1925) provides analytical results for pressure and vertical settlement in a porous saturated column which is bearing a constant load applied on its top. The geometry of the problem is shown in Figure 3.8. The drainage is only allowed

through the top surface, and the bottom of the column is fixed. Analytical solutions can be found in Ferronato et al., 2010. Figure 3.9 and 3.10 respectively show that the results for both pore pressure and vertical displacement along the column gained from our finite element code match well with the analytical solution.

Mandel's problem (Mandel, 1953) consists of a porous medium located between two impermeable rigid plates which are loaded by a constant vertical force. The geometry of the problem is shown in Figure 3.11. Drainage is allowed from the right and left boundaries $(x = \pm a)$. The force per unit length, infinitely long in y-direction, is initially applied at $t = 0$ to the plate and results in an increase in the pressure to give an overpressure. Over time, the overpressure which is first generated by the sudden load application makes the pressure to rise to a certain point as the result of coupled strain transfer, and finally the pressure starts to decrease due to the increasing influence of the drainage. The initial increase in pressure is called the Mandel-Cryer effect. The analytical solution for evolution of pressure and displacement over time can be found in Ferronato et al., 2010, including detailed explanations of parameter $p_{\circ}$, which is defined as the initial overpressure, and parameter c, used in plots in order to obtain normalized pressure and dimensionless time. Figure 3.12 shows the results of finite element approach compared to the analytical solution.

Table 3.2 Hydro-Mechanical properties used for Terzaghi's consolidation problem and Mandel's problem

$K(m/s)$	a(m)	b(m)	E(Pa)	v	n	$\beta(1/\text{Pa})$
10^{-5}	8	8	10^{8}	0.25	0.375	4.4×10^{-10}

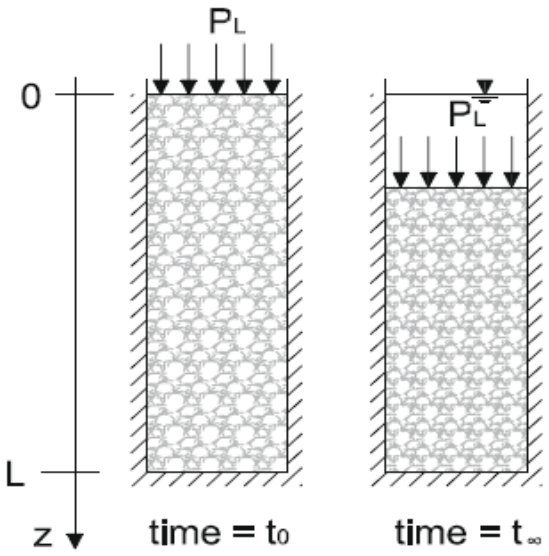

Figure 3.8 Geometry of Terzaghi's consolidation problem (Ferronato et al., 2010).

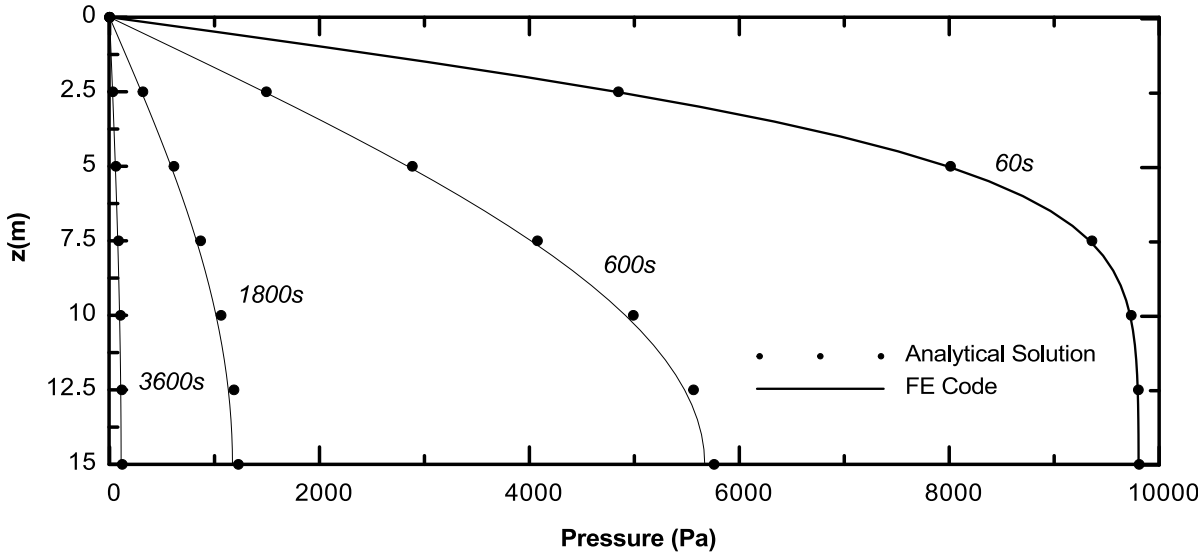

Figure 3.9 Terzaghi's consolidation: Analytical and numerical solution for evolution of pore pressure during different time periods (Maximum percentage error=1.54%).

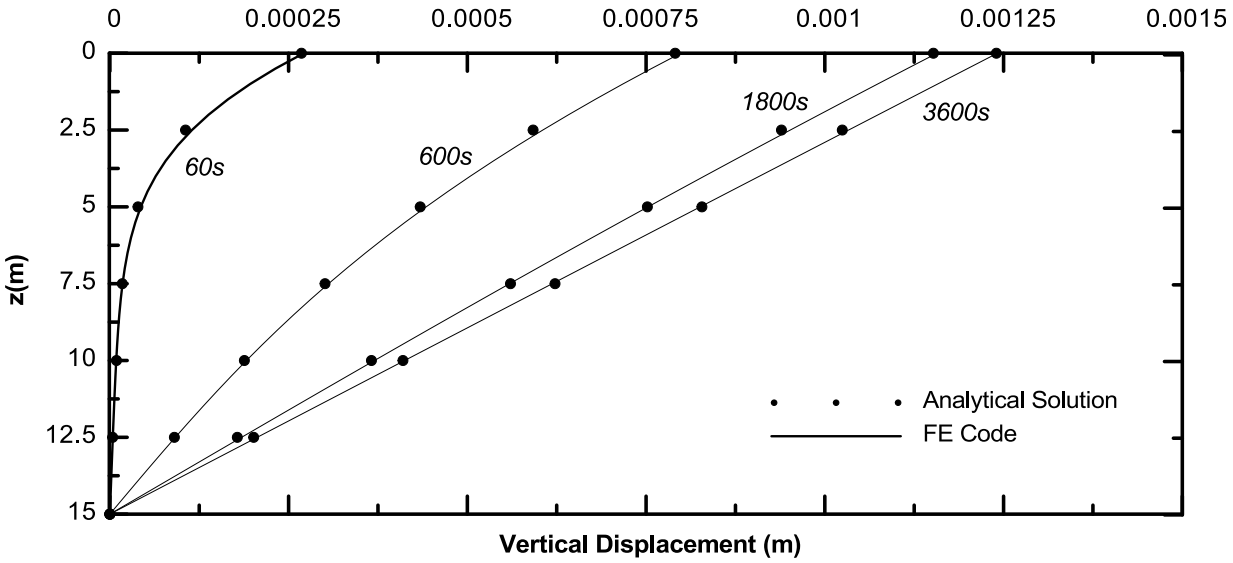

Figure 3.10 Terzaghi's consolidation: Analytical and numerical solution for evolution of vertical displacement during different time periods (Maximum percentage error=0.9%).

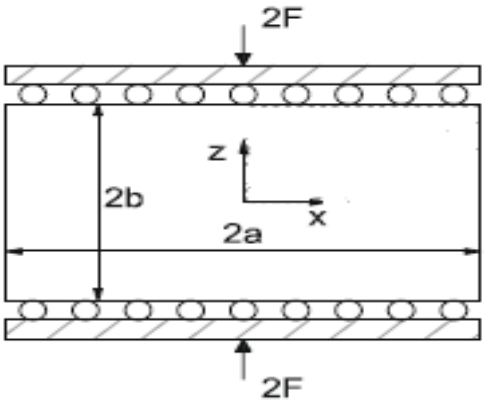

Figure 3.11 Geometry of Mandel's problem (Ferronato et al., 2010).

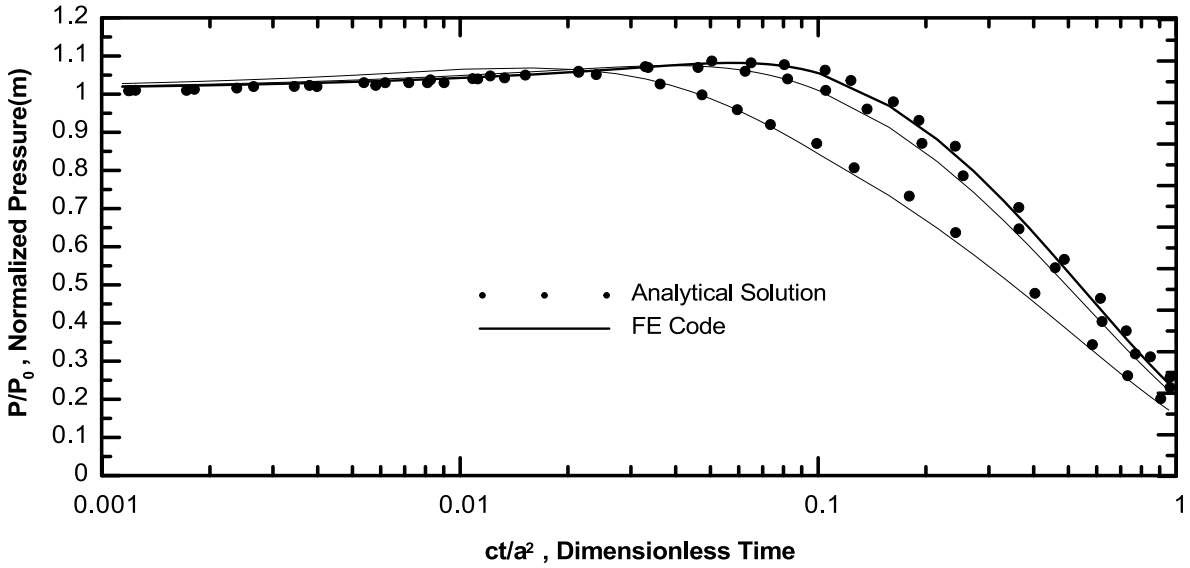

Figure 3.12 Mandel's problem: Analytical and numerical solution for pore pressure evolution at three different line sections (Maximum percentage error=2.52%).

In order to make sure that the code works for solving a realistic engineering application, the consolidation problem is observed in a geological layer with realistic characteristics. A detailed definition of the problem can be found in Selvadurai and Nguyen, 1995. The geometry of the problem is provided in Figure 3.13. Drainage is allowed from the top surface, and the normal displacements to left and bottom boundaries are fixed. It is expected to observe Mandel-Cryer effect as a result of the load. Both pore fluid and the solid skeleton are considered incompressible. Figure 3.14 and 3.15 respectively show the comparison between the results obtained for vertical displacement and pore pressure history with FE code and the analytical solution. Dimensionless values for displacement and pore pressure are calculated at point A located on the left boundary, where $z/b = 0.364$.

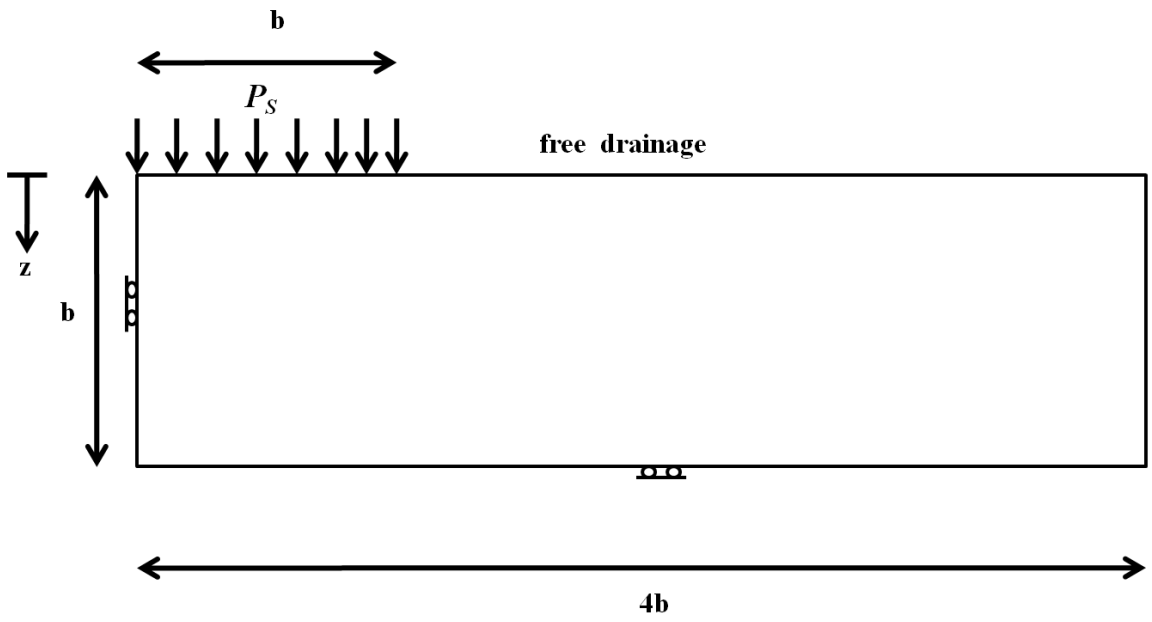

Figure 3.13 Geometry of the third poroelasticity problem.

Table 3.3 Hydro-mechanical properties used for the third problem of poroelasticity (characteristics of a typical plutonic rock mass of Canadian Shield).

$K(m/s)$	b(m)	E(GPa)	ν	$P_S(\mathrm{M}Pa)$	α_b
5×10^{-11}	5000	35	0.2	30	1

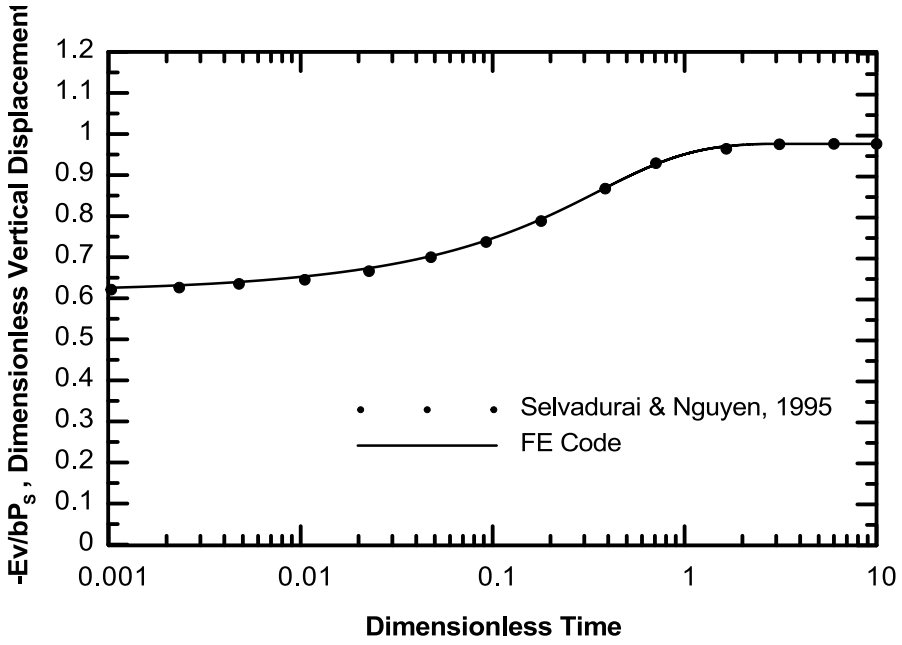

Figure 3.14 Dimensionless vertical displacement for the third problem at $z = 0.364b$ on the left boundary (Maximum percentage error=0.63%).

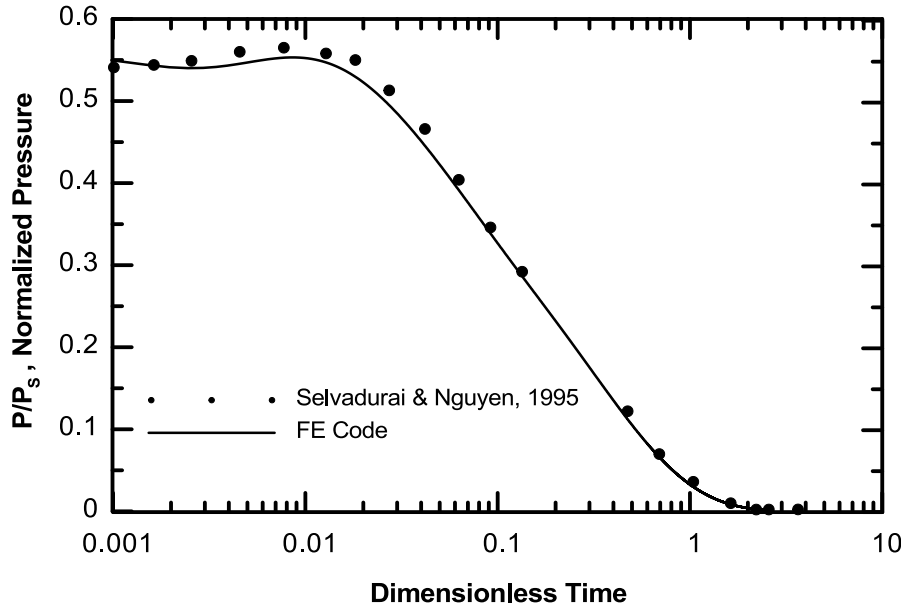

Figure 3.15 Dimensionless pore pressure history for the third problem at $z = 0.364b$ on the left boundary (Maximum percentage error=1.65%).

3.5.3 Heat Transfer and Thermoelasticity

In order to investigate correctness of FE code in solving temperature-related problems, three cases are considered. First, heat transfer equation alone is used to get the temperature profile in a plane sheet under conductive heat flow. Second, diffusion and advection terms are both included in the problem defined by the author. And finally, in order to measure the accuracy of temperature-displacement coupling, an infinitely long cylinder exposed to a temperature difference on its surface is analyzed.

Analytical solution exists for the temperature profile along a plane sheet with two constant temperatures maintained on its sides (Crank, 1975). The geometry of the problem is presented in Figure 3.16. The initial temperature is zero all over the plane until the left side undergoes a constant $T = 100^{\circ}C$ temperature change. The problem is solved with FE code and comparing the outputs, which are temperature profiles along the sheet after particular time durations, good matching between analytical and numerical solution procedures is observed (Figure 3.17). Input values used for solving this problem are given in Table 3.4.

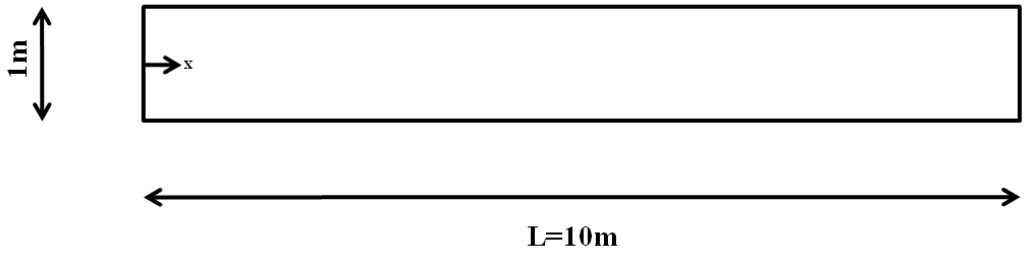

Figure 3.16 Geometry of 1D heat conduction problem

Table 3.4 Thermal properties used for conductive heat transfer in a plane sheet.

$\kappa(\mathrm{W/\,m/\,^{\circ}C})$	$\rho_e C_e (J/m^3/K)$
3.9	2×10^5

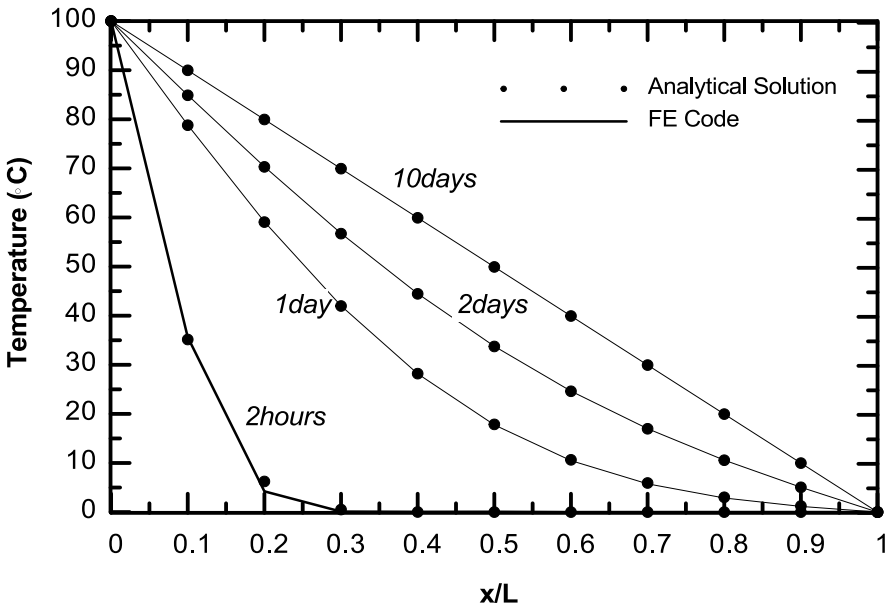

Figure 3.17 Comparison between analytical and numerical results for temperature distribution along the plane sheet length for different time durations (Maximum percentage error=0.56%).

In order to verify the rightness of advection term, a problem is defined by author and solved using FE code and COMSOL software. The model is presented in Figure 3.18 and the inputs are given in Table 3.5. Darcy velocity is considered equal to 0.00001 in x direction. As it can be seen, the left boundary is exposed by $20^{\circ}C$ temperature reduction. Figure 3.19 shows the temperature distribution along the horizontal arc located in the middle of the medium after five hours. Comparing to COMSOL results, FE code gives satisfactory results based on the observed results.

Table 3.5 Thermal properties used for convective heat transfer problem

$\kappa(\mathrm{W/m/^{\circ}C})$	$\rho_e C_e (J/m^3/K)$	$\rho_f C_f (J/m^3/K)$
3	2×10^6	4.2×10^6

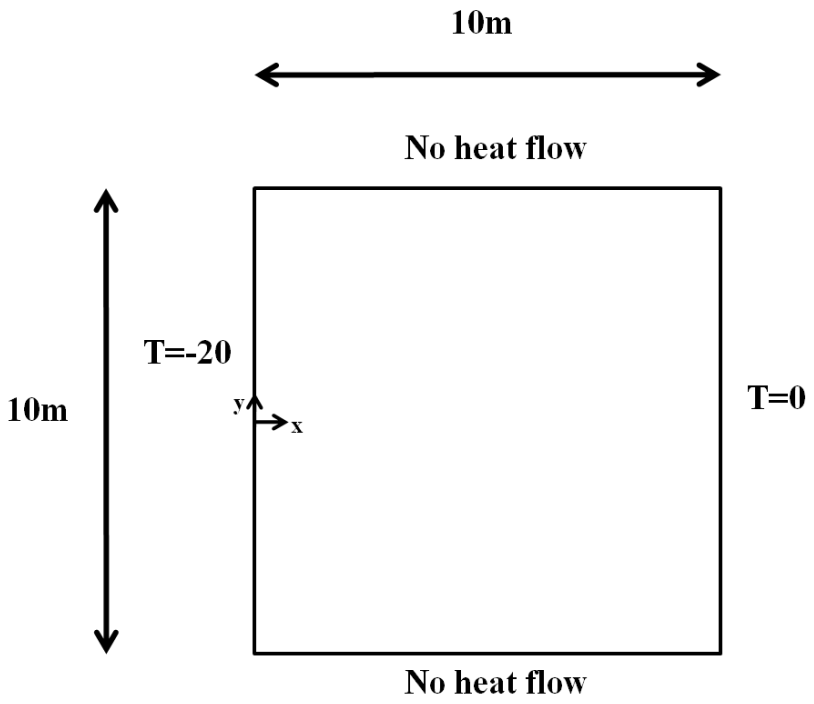

Figure 3.18 Geometry of convective heat transfer problem

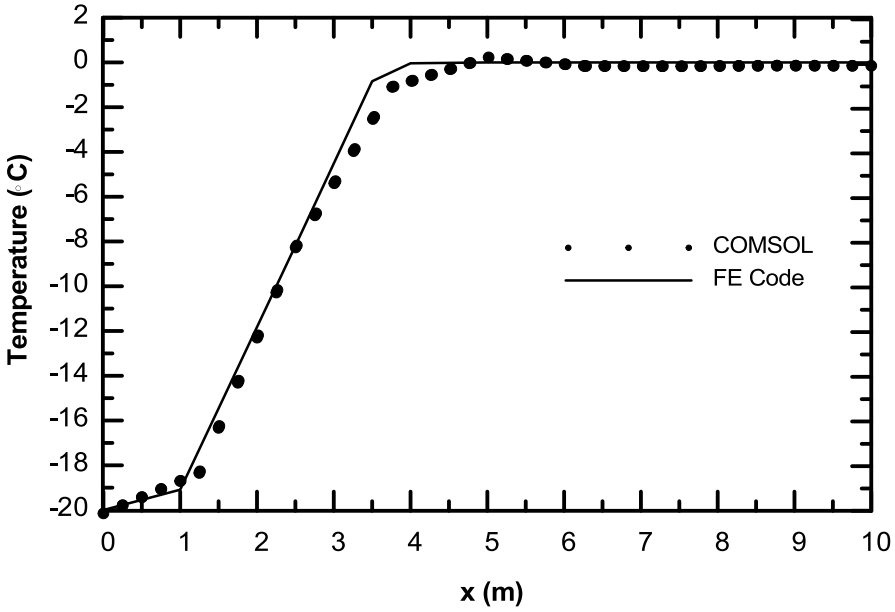

Figure 3.19 Numerical results obtained using COMSOL and FE code for temperature along the model at $y = 0$ (Average percentage error=6.1%).

Modeling an infinitely long cylinder exposed to a temperature difference on its surface is one of the classic thermo-elasticity problems with an existing analytical solution. The cylinder is considered infinitely long in one direction and therefore the problem is solved in 2D for one circular segment. Initial temperature of the whole cylinder can be zero or non-zero. Analytical solutions exist for both temperature profile and cylinder deformation due to temperature change and can be found in Carter, 1989. The analysis shows that numerical solutions perfectly match the analytical solutions in both zero and non-zero initial temperature conditions. Input values for this problem are shown in Table 3.6. Figure 3.20 and 3.21 show the comparison of analytical and numerical solutions for temperature distribution and radial surface displacement in case of zero initial temperature, while Figure 3.22 and 3.23 show the comparison in case of non-zero initial temperature. In this example, it is considered that the surface of the cylinder undergoes $100^{\circ}C$ of temperature change $(\Delta T_0 = 100^{\circ}C)$. Note that 'r' is the distance from the center of the circular section, 'R' is the radius of the section, is the surface temperature change, ΔT is the temperature change within the cylinder, and 'TT' is dimensionless time (each TT indicates a certain value of time). $A/M = 1$ indicates that the initial temperature of the cylinder is zero. $A/M = 1.5$ indicates non-zero initial temperature. Detailed explanations of A, M and TT can be also found in Carter, 1989.

Table 3.6 Thermal and mechanical properties used for thermo-elasticity problem

κ(W/ m/ $^{\circ}C$)	$\rho_e C_e (J/m^3/K)$	E(MPa)	ν	$\alpha_s (1/K)$	$R(m)$
3.9	2×10^5	100	0.3	0.00208	10

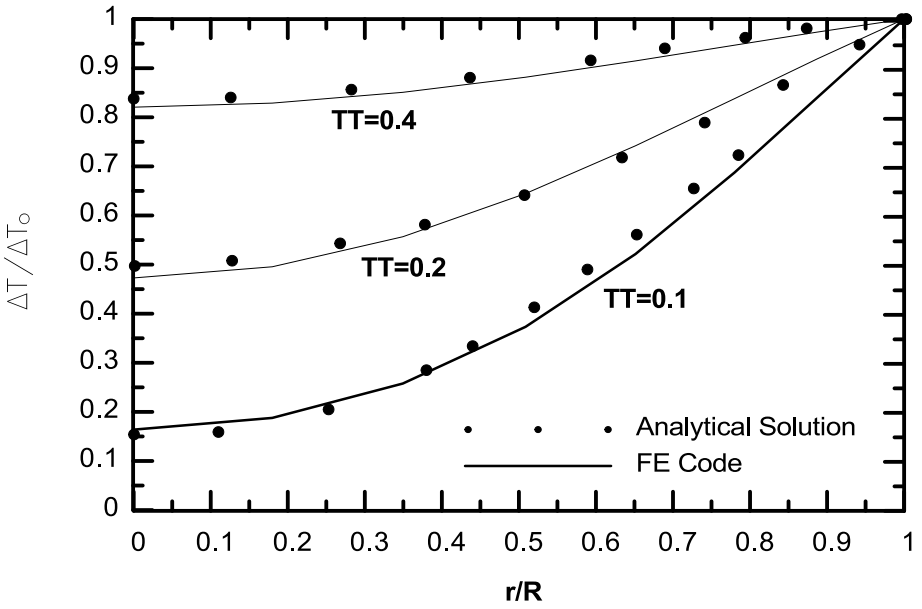

Figure 3.20 Comparison between analytical and numerical results for temperature distribution along the cylinder for different time periods with $A/M=1$ (Maximum percentage error=3.7%).

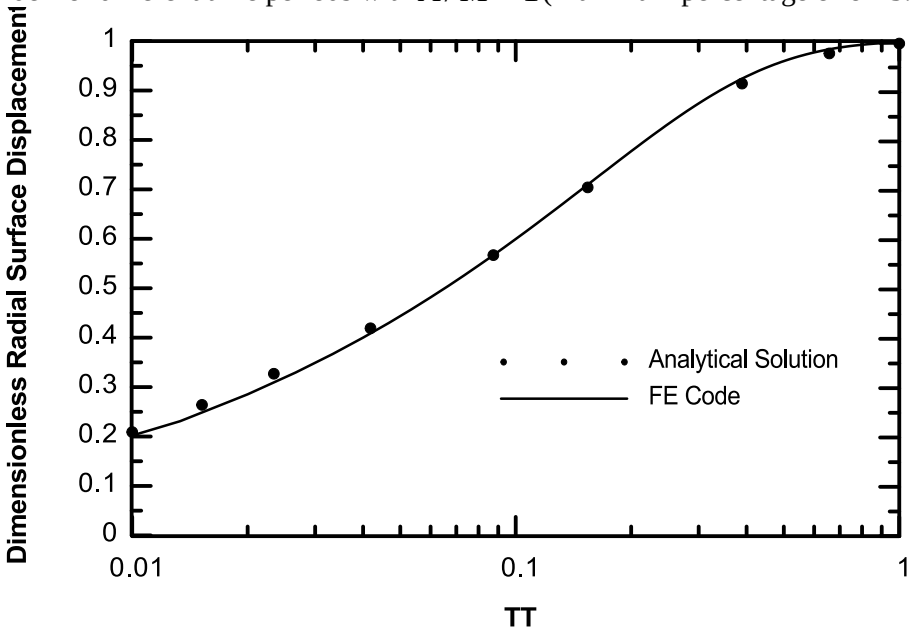

Figure 3.21 Comparison between analytical and numerical results of radial surface displacement evolution through time with $A/M=1$ (Maximum percentage error=2.6%).

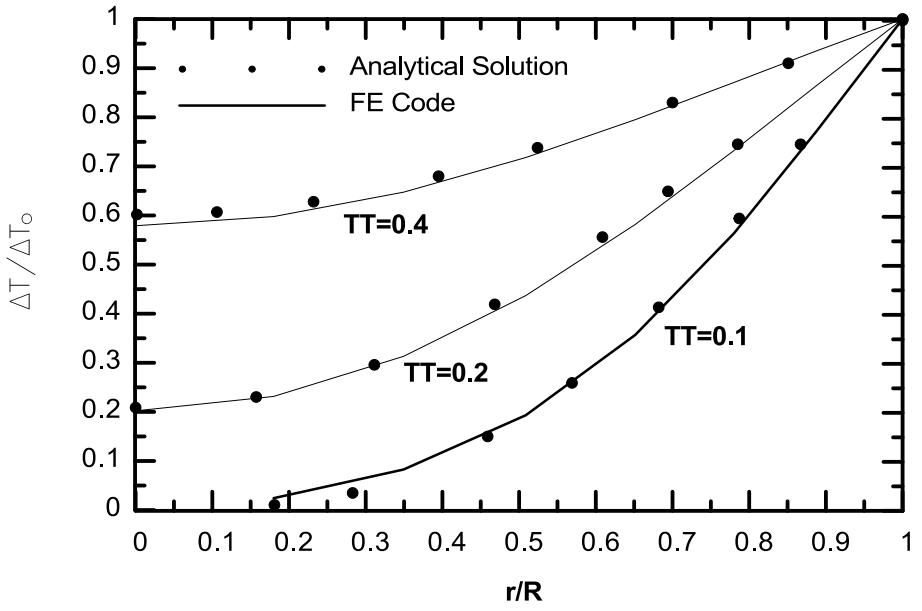

Figure 3.22 Comparison between analytical and numerical results for temperature distribution along the cylinder for different time periods with $A/M = 1.5$ (Maximum percentage error=7.6%).

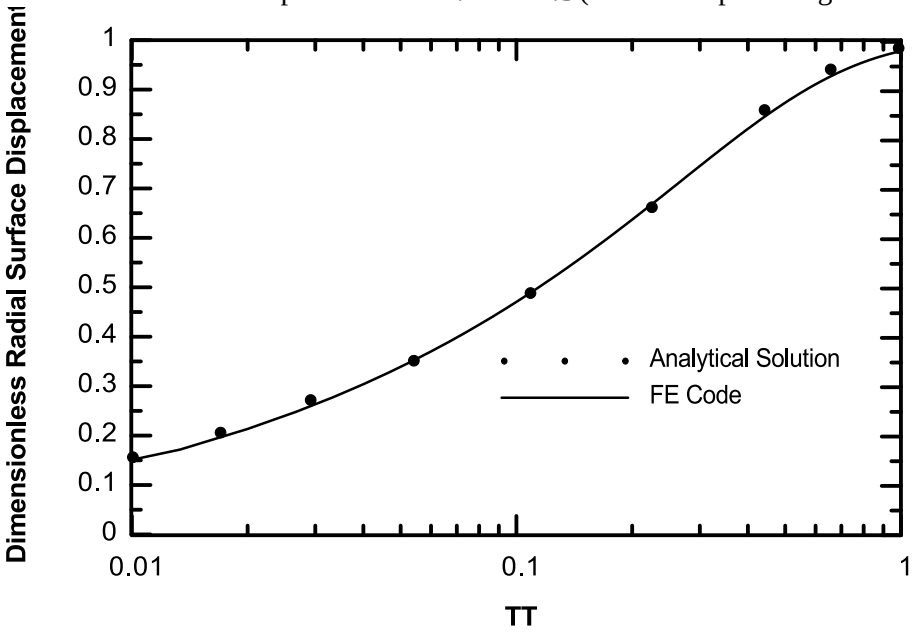

Figure 3.23 Comparison between analytical and numerical results of radial surface displacement evolution through time with $A/M = 1.5$ (Maximum percentage error=2.3%).

Having solved the benchmark problems presented, it can be concluded that the computer code written for this research study performs well and all parts of the final solution matrix are properly placed in order to give a correct THM coupled analysis.

3.6 Problem Definition

The model geometry is presented in Figure 3.24. A two-dimensional domain, 4.5 km × 2 km in size, is considered. A specific permeable stratum is assumed to exist in the impermeable medium, in order to represent the EGS system. Except the left boundary where no fluid and heat flow are allowed, other boundaries are open for fluid flow and heat transfer. The normal displacement is fixed for left and bottom boundaries, while the other two are free. THM properties of porous medium and fault characteristics are given in Table 3.7 and Table 3.8 respectively. Reasonable values are selected for all input parameters so that the case becomes similar to a real field situation. These values are chosen after investigating the proper ranges in the literature (Robertson, 1988) or obtained from other similar subsurface studies available (Rutqvist, 2013, Cappa and Rutqvist, 2011). Thermal properties of the fault are considered same as porous medium. In order to satisfy the stability of the model, it has been defined wide enough to make sure there would be no horizontal displacement far from the injection zone.

Table 3.7 THM properties used for porous media in enhanced geothermal system

κ(W/ m/ $^{\circ}C$)	$\rho_s(kg/m^3)$	$\rho_f(kg/m^3)$	E(GPa)
2.79	2600	1000	50
ν	n	$C_s(J/kg.^{\circ}C)$	$C_f(J/kg.^{\circ}C)$
0.25	0.375	790	4200
$k_{stratum}(m^2)$	$k_{medium}(m^2)$	$\beta_f(1/K)$	$\beta(1/Pa)$
10^{-14}	10^{-19}	2.4×10^{-5}	4.4×10^{-10}

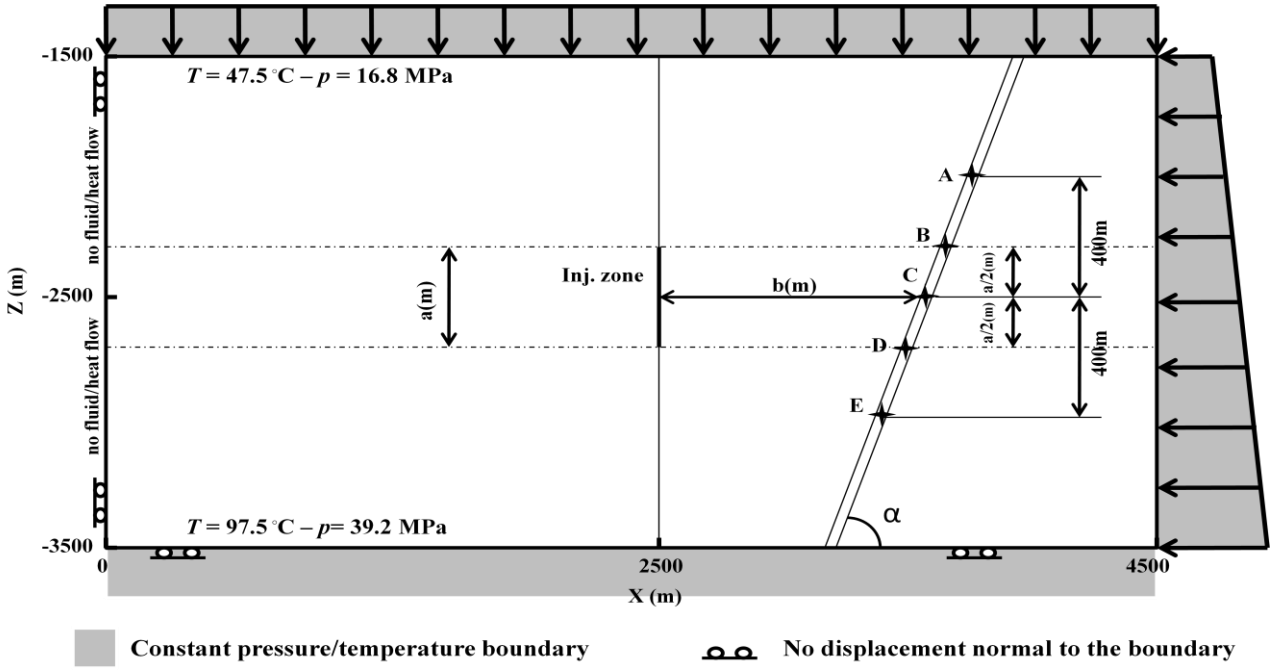

Figure 3.24 EGS numerical model domain with initial and boundary conditions (The figure is not to scale)

Table 3.8 Properties used for fault in enhanced geothermal system. Other input values for fault elements are the same as porous medium characteristics. Zero value for c indicates that fault is assumed to be cohesionless.

$k_{fault}(m^2)$	E(GPa)	ϕ	c
10^{-16}	5	25°	0

3.7 Justification of Using Solid Elements for Fault

One of the well-known methods of modeling fault elements is using zero-thickness interface elements, introduced by Goodman et al., 1968. In this method, shear and normal stress on the fault are calculated as a function of relative displacements of the top and the bottom of the fault element, multiplied by shear and normal stiffness of the fault which are given as an input. Goodman element allows for controlling the opening and closure of the

fault as well, which results in introducing non-linearity in the coding procedure. However, it was observed that the relative displacements calculated directly from finite element results matches well with the relative displacements calculated using Goodman's element shape functions. Since this research only focuses on the stress state of the fault element, it is concluded that solid elements are appropriate enough to go on with the analysis. Figure 3.25 and 3.26 show comparison between the results obtained for relative displacement along the edge of the fault where point B is located. Once FE code results are transformed sixty degrees and the relative displacements of two sides of the fault element are calculated, and once, interface element shape functions are used to calculate this value. As the graphs show, these two methods provide with similar results. Interface element shape functions used here are the ones used for a six-noded interface element, which can be found in Li and Kaliakin, 1993. It should still be mentioned that obviously interface element approach is more complex and can provide with more options in the fault analysis, but for the target of this study, using solid elements is adequate.

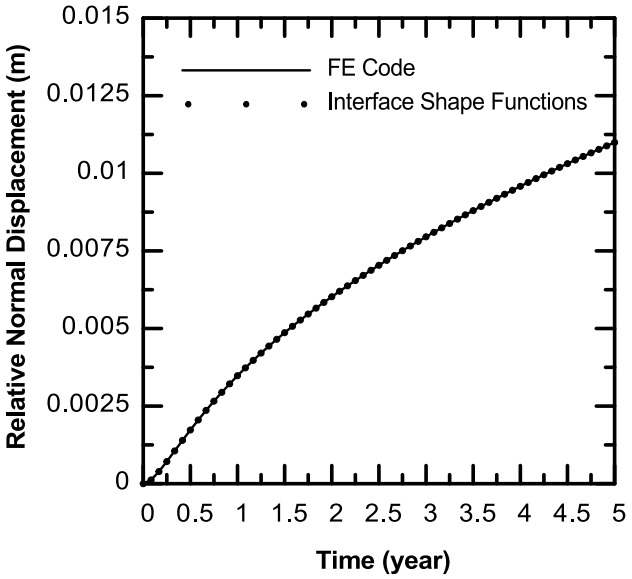

Figure 3.25 Relative normal displacements in the fault at point B, calculated by direct use of FE results and interface element shape functions.

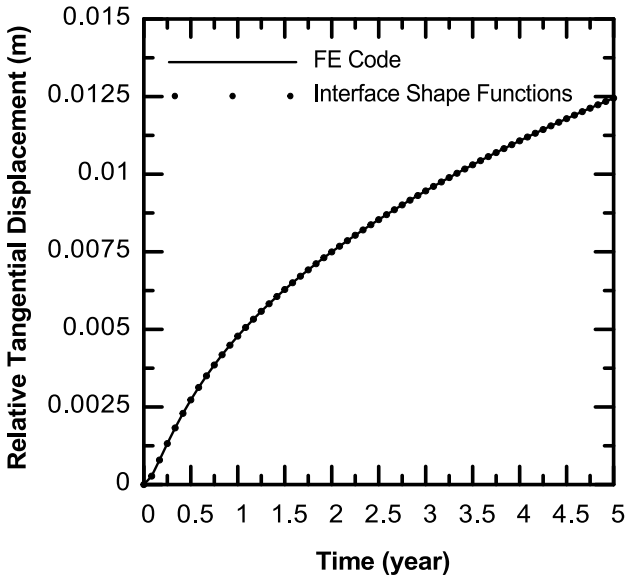

Figure 3.26 Relative normal displacements in the fault at point B, calculated by direct use of FE results and interface element shape functions.

3.8 Parametric Study

This type of geothermal process can take place at depths of 2km to 8km. In this thesis, for the analysis, a shallow case of geothermal resource is considered where the stratum is located 2.5km deep. The vertical stress (total) would be around 60 MPa (Bedrock column with an average density of 2.68 g/cm^3). The lateral stress is a parametrically varying number, and two cases are considered: extensional stress regime, and compressional stress regime, with effective stress ratios of 0.6, and 1.5 respectively, reflecting the range of conditions one might expect in various tectonic regimes. The initial pore pressure is considered around 28 MPa (salty water column with an average density of 1.14 g/cm^3) in the stratum. Generally, the pressure gradient is considered $11.2 MPa/\text{km}$. The injection program is considered in a way such that a total rate of 0.02 kg/s of water is achieved at each time step. The injection goes on for 5 years. This injection is implemented

in FE code as a Neumann boundary condition, while the cooling process as a result of injection is given as a Dirichlet boundary condition where the injection line provides with $30^{\circ}C$ of temperature reduction. Temperature gradient is considered $25^{\circ}C/km$ in addition to $10^{\circ}C$ of surface temperature.

In the parametric study, the seismic fracture potential is evaluated in a 5 year period after the beginning of hydraulic stimulation. Five points of interest (A to E in Figure 3.24) are considered along the fault. Points A, E, and C are fixed at depths 2100m, 2500m, and 2900m, respectively. Points B and D are considered at the edge of permeable stratum, therefore their location depends on the thickness of stratum. The effects of several factors on evolution of shear fracture potential are studied, focusing on the changes occurring to stress state in these five points of interest under both stress regimes.

3.8.1 Effect of Fault Dip Angle (α)

Along choosing constant values of $200m$ and $1000m$ for a and b respectively, we chose three different values of α and observed the differences of fracture potential evolution for five points of interests.

Figure 3.27 and 3.28 show that there is not much of increase in probability of seismic potential increase in point A under both stress regimes, in fact a decrease is observed in case of $\alpha = 60^{\circ}$. A small change is seen in sFP value for extensional regime for all values of α. The increase in sFP is less in case of higher fault angles.

Figure 3.29 and 3.30 show a significant difference between evolution of sFP under compressional and extensional regimes. First of all, seismic activity is observed in an extensional regime with fault dip angles of 75° and 90°. In compressional regime, lowest

fault dip angle shows a higher probability of shear slip, comparing to other two angles, although the likelihood of shear slip for the same case in extensional regime is still higher.

Figure 3.31 and 3.32 show that similar to point B, seismic activity is observed in point C for cases of in extensional regime, although the events occur in earlier stages of injection process. The trend of sFP change in compressional regime is similar to point B, with slight difference in actual values.

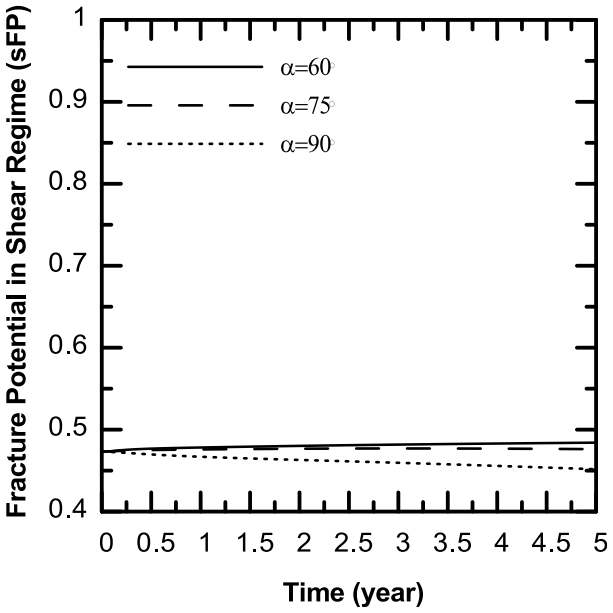

Figure 3.27 sFP evolution in 5 years for point A in compressional regime in case of different fault angles.

By comparing point C and point D plots, The first deduction is that still the seismic events show up in point C in a shorter period of time for $\alpha = 75^{\circ}, \alpha = 90^{\circ}$. The second matter is that in case of $\alpha = 75^{\circ}$, seismic event is only observed in point D. This means that defining the most critical point for observation is completely dependent on the fault angle. Figure 3.33 and 3.34 show the changes of sFP in point D.

It seems that the operation does not affect point E as much as other points of interests. A small decrease in seismic probability in compressional regime and a slight increase occur for all of three different values of α (Figure 3.35 and 3.36).

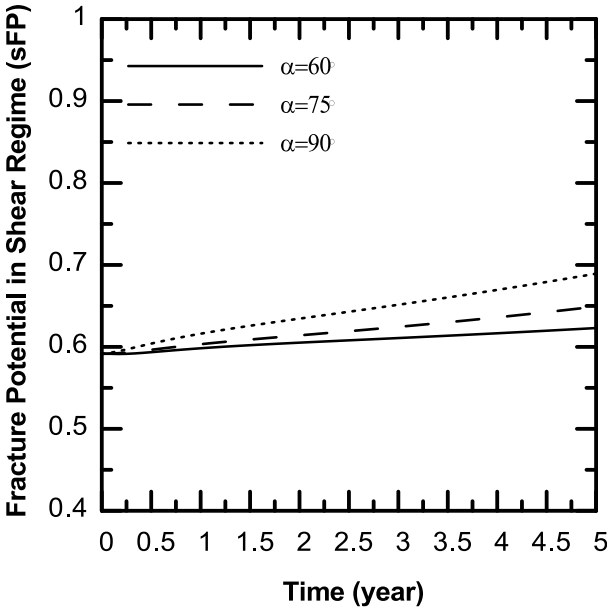

Figure 3.28 sFP evolution in 5 years for point A in extensional regime in case of different fault angles. 90°).

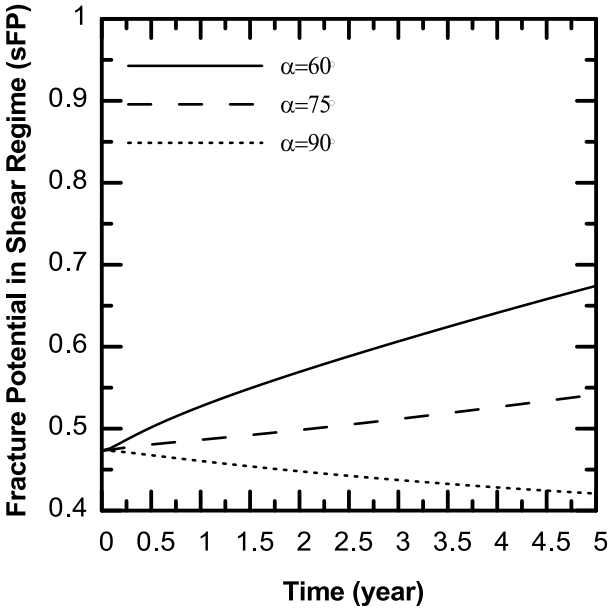

Figure 3.29 sFP evolution in 5 years for point B in compressional regime in case of different fault angles.

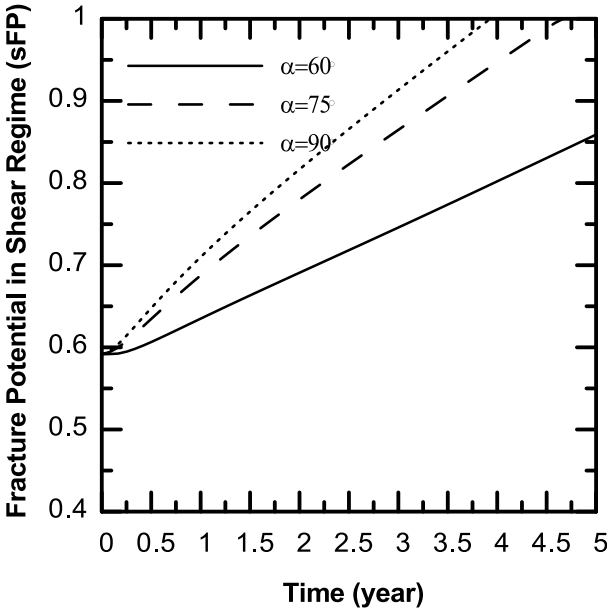

Figure 3.30 sFP evolution in 5 years for point B in extensional regime in case of different fault angles.

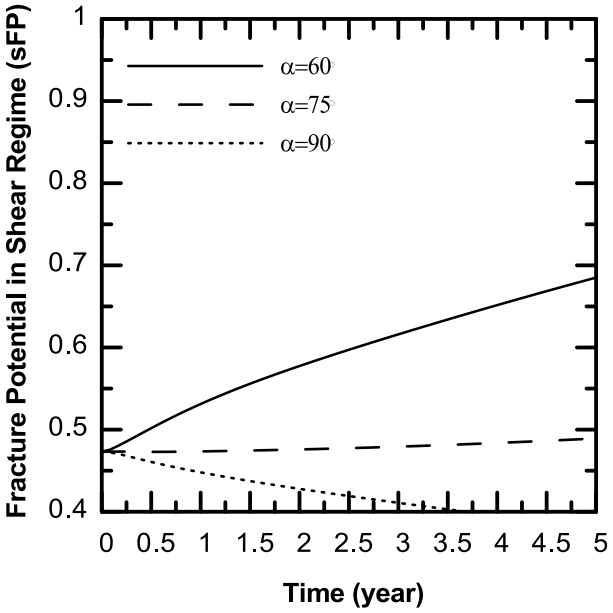

Figure 3.31 sFP evolution in 5 years for point C in compressional regime in case of different fault angles.

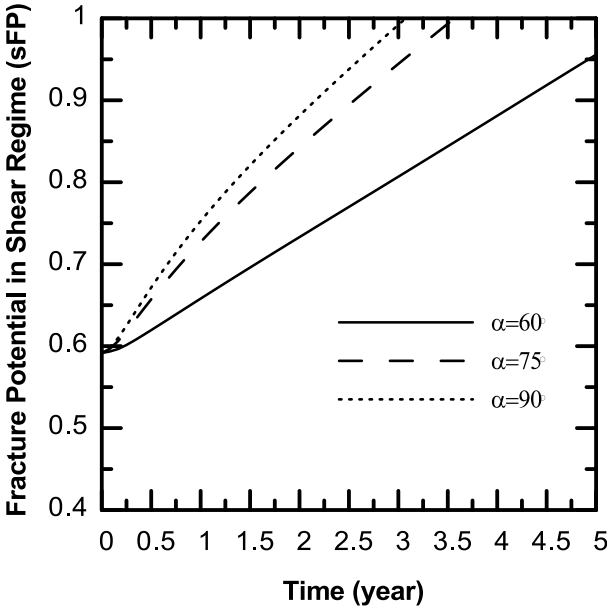

Figure 3.32 sFP evolution in 5 years for point C in extensional regime in case of different fault angles.

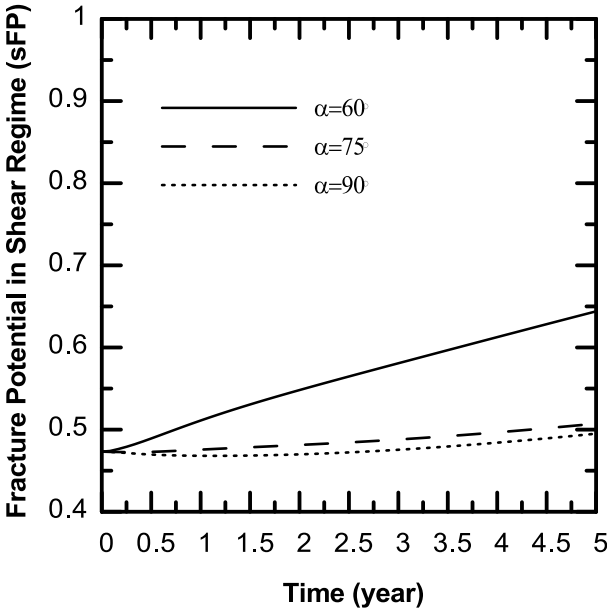

Figure 3.33 sFP evolution in 5 years for point D in compressional regime in case of different fault angles.

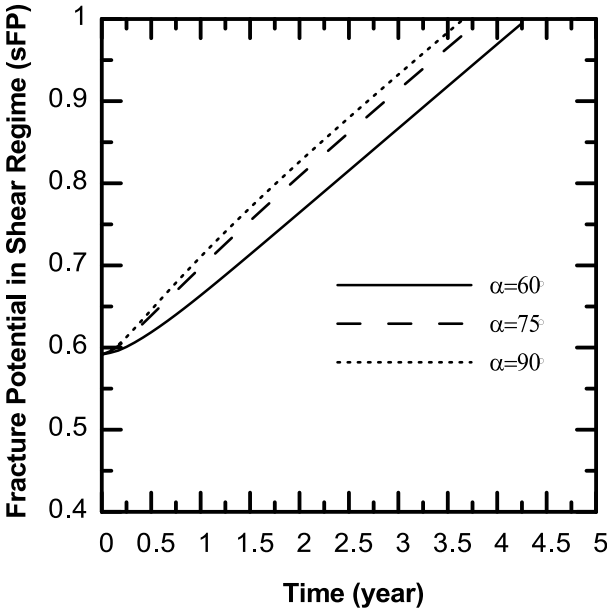

Figure 3.34 sFP evolution in 5 years for point D in extensional regime in case of different fault angles.

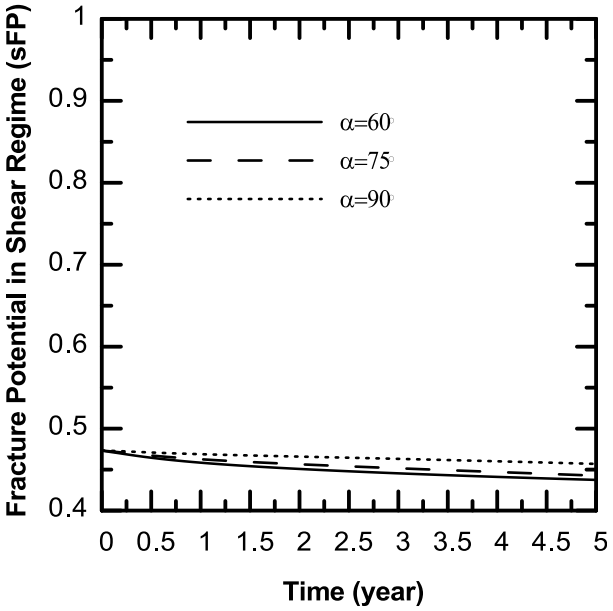

Figure 3.35 sFP evolution in 5 years for point E in compressional regime in case of different fault angles.

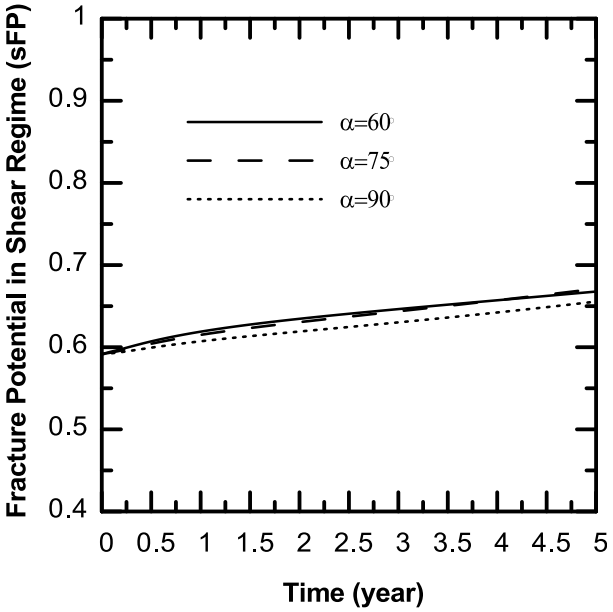

Figure 3.36 sFP evolution in 5 years for point E in extensional regime in case of different fault angles.

As it is mentioned before, the values of sFP in each time step are calculated using the values of horizontal and vertical effective stress drop as a result of cold fluid injection, which are an outcome of thermo-poro-elastic effects and subsequently temperature and pressure distribution. In order to provide with an example, the changes in temperature, pressure, and effective stresses along the fault after 5 years in case of a fault with dip angle of 60° are plotted and shown in Figures 3.37 to 3.34. It is visible that the pressure change has resulted in effective stress changes and therefore the total stress increase is lower than the amount of pressure increase. As it can be seen, the effect of cooling is not reached to the fault and the reason behind the changes in sFP is only poro-elastic effects. This is mainly because of low permeability of the whole system, and more importantly the linear FE approach where the permeability stays the same through the whole analysis. As a result of constant low permeability, convective heat term does not contribute to heat transfer, and the temperature decrease does not propagate in the medium.

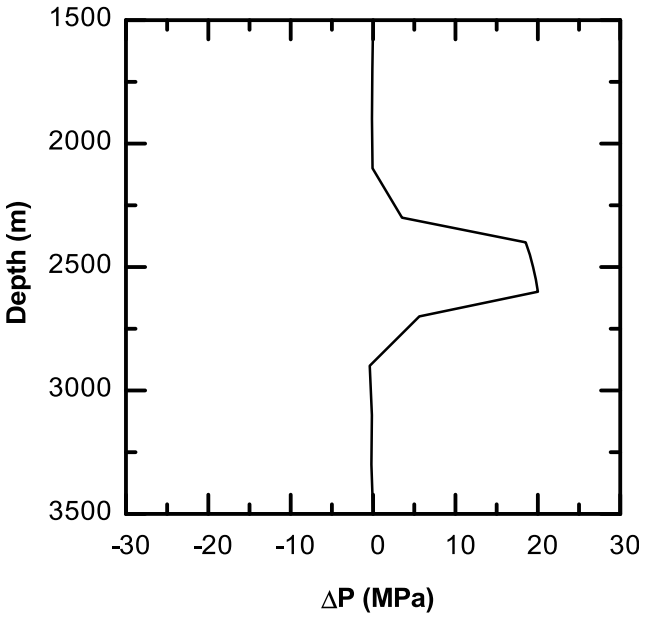

Figure 3.37 Profile of pressure change along the fault after five years of injection.

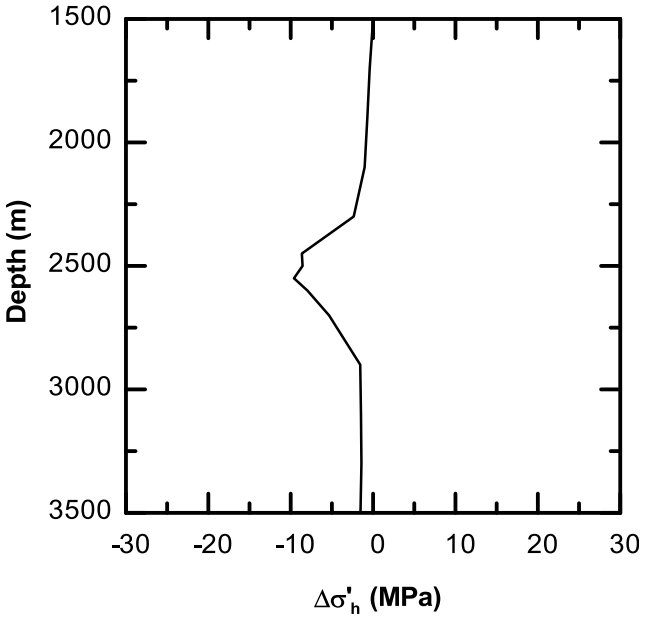

Figure 3.38 Profile of effective horizontal stress change along the fault after five years of injection.

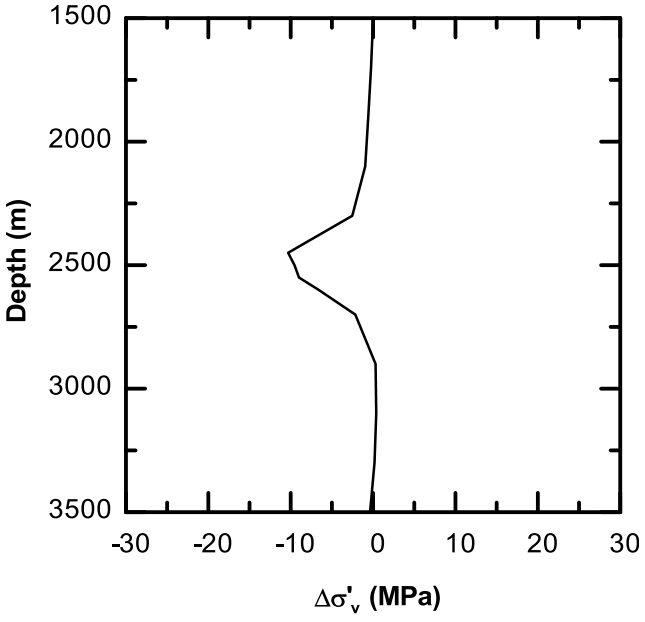

Figure 3.39 Profile of effective vertical stress change along the fault after five years of injection.

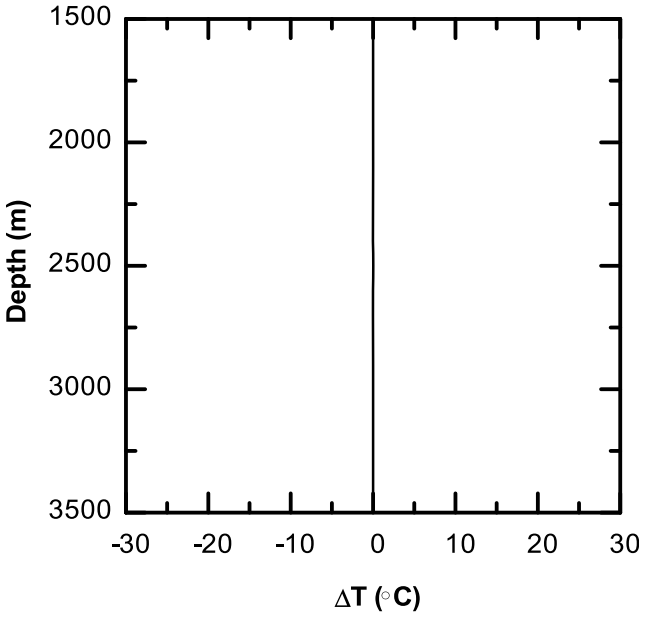

Figure 3.40 Profile of temperature change along the fault after five years of injection.

3.8.2 Effect of Stratum Thickness (a)

In this section, constant values of 60° and $1000m$ are considered for α and b respectively and the effect of a , height of permeable layer is studied. Three different values: $100m$, $200m$, and $400m$ are given as inputs for a and sFP changes in all cases under both stress regimes in all points of interest are plotted.

It can be seen from Figure 3.41 and 3.42 that there is not much of change in sFP value in point A. In both stress regimes the value is not increased more than 0.1.

Figure 3.43 and 3.44 show that sFP increases significantly in point B as a result of injection. In both stress regimes, probability of exhibiting seismic potential is lower in thicker layers. However, no failure is still observed.

The trend observed in point B is also seen in point C and D (Figure 3.45 to 3.48). However, seismic failure is more likely in the case of thin permeable layers. Again,

extensional regime is more at risk at both points, and thicker layer shows less probability of increase in seismic potential.

Beside point A, the only location where the highest value of layer thickness shows more potential of activity under extensional stress regime is Point E. However, comparing to other points, the increase in sFP in this case is not significant (Figure 3.43 and Figure 3.44). In compressional regime, probability stays constant in case of thin permeable layer and decreases in the thicker stratum.

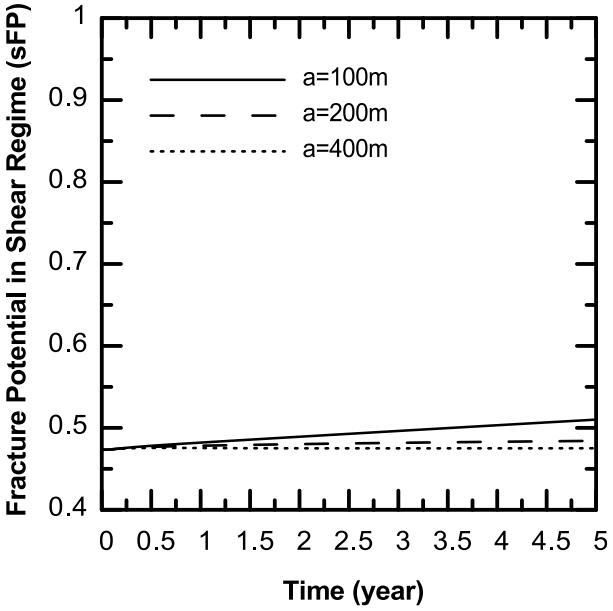

Figure 3.41 sFP evolution in 5 years for point A in compressional regime in case of different stratum thicknesses.

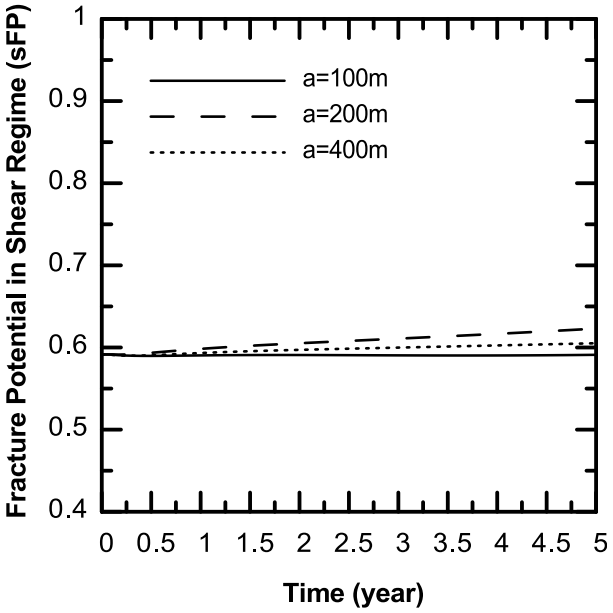

Figure 3.42 sFP evolution in 5 years for point A in extensional regime in case of different stratum thicknesses.

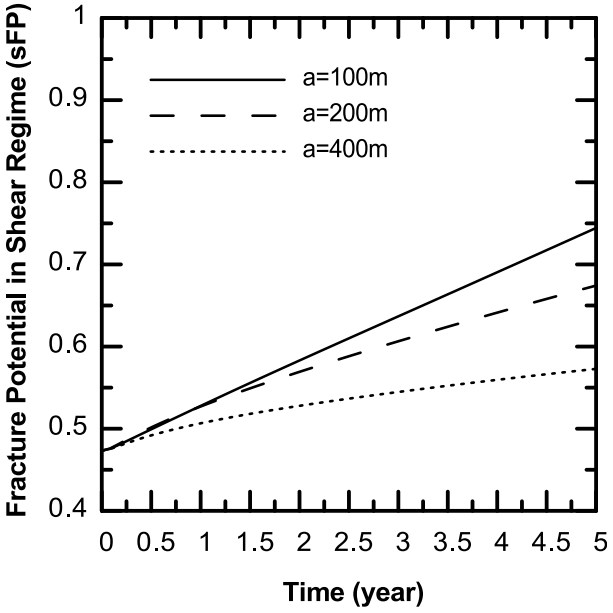

Figure 3.43 sFP evolution in 5 years for point B in compressional regime in case of different stratum thicknesses.

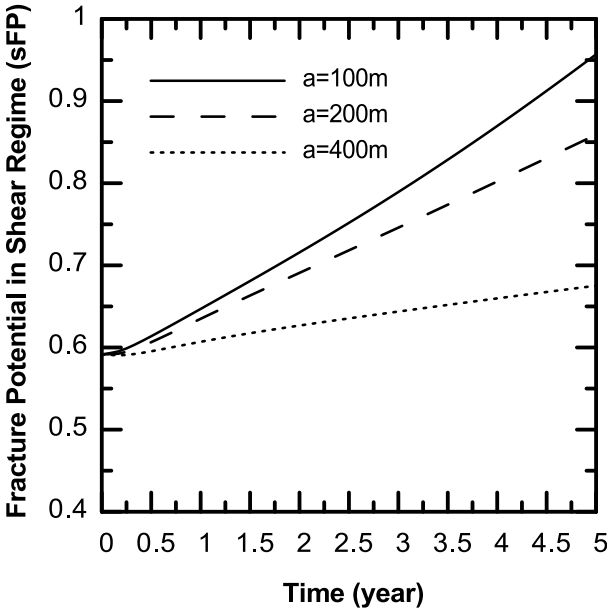

Figure 3.44 sFP evolution in 5 years for point B in extensional regime in case of different stratum thicknesses.

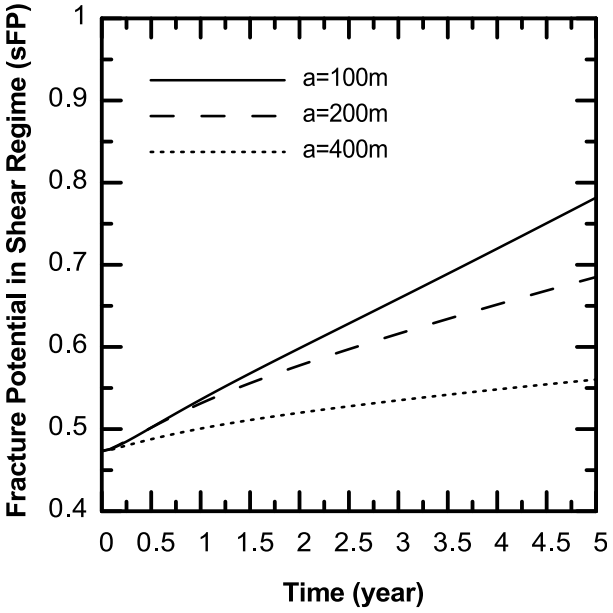

Figure 3.45 sFP evolution in 5 years for point C in compressional regime in case of different stratum thicknesses.

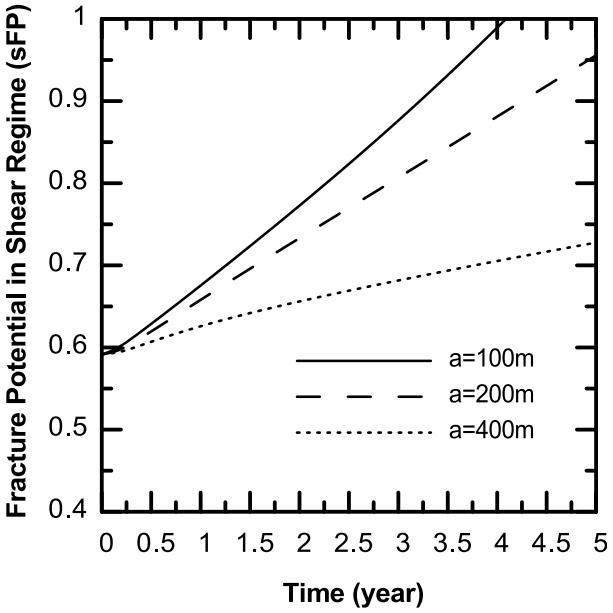

Figure 3.46 sFP evolution in 5 years for point C in extensional regime in case of different stratum thicknesses.

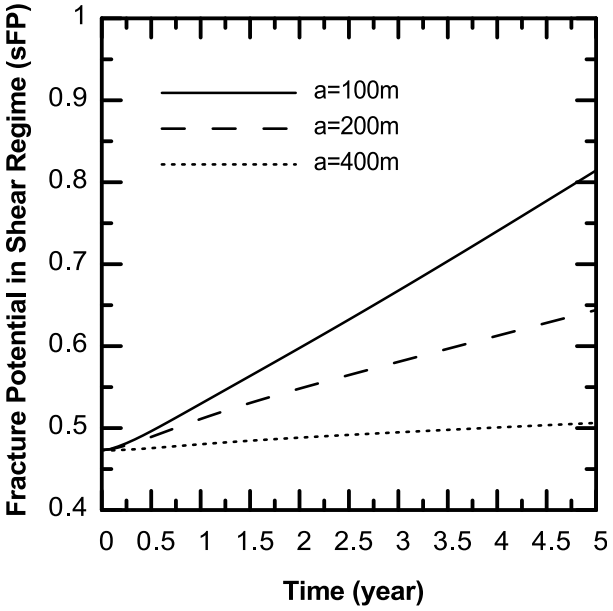

Figure 3.47 sFP evolution in 5 years for point D in compressional regime in case of different stratum thicknesses.

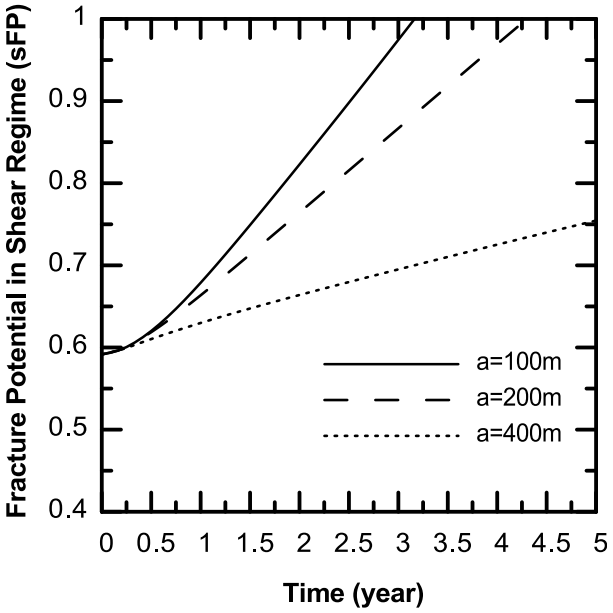

Figure 3.48 sFP evolution in 5 years for point D in extensional regime in case of different stratum thicknesses

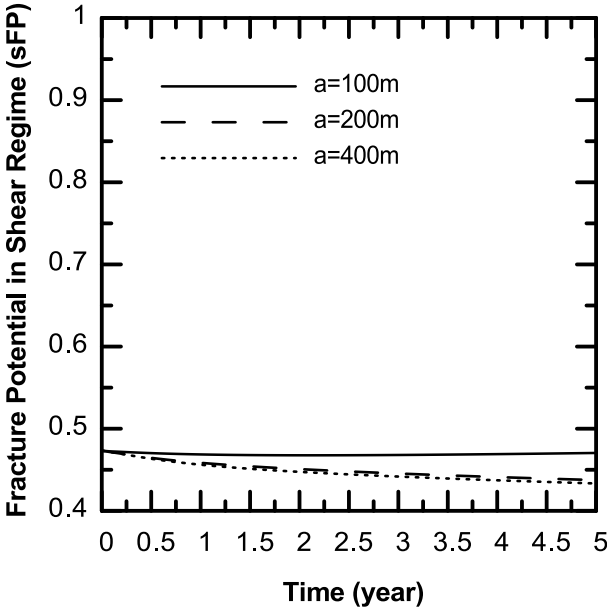

Figure 3.49 sFP evolution in 5 years for point E in compressional regime in case of different stratum thicknesses.

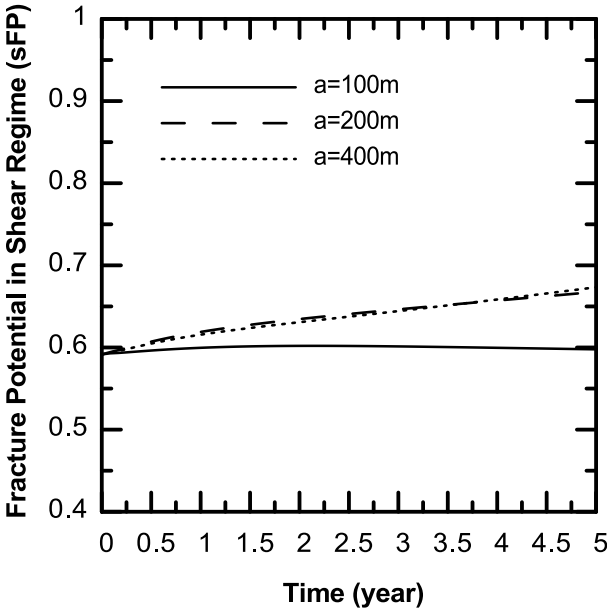

Figure 3.50 sFP evolution in 5 years for point E in extensional regime in case of different stratum thicknesses.

3.8.3 Effect of Horizontal Distance between Injection Zone and Fault (b)

In this section, three simulations were performed with three different values as an input for b ($750m$, $1000m$, and $1250m$). Input values used for permeable layer thickness and fault angle are the same in all three simulations. The fault angle is equal to 60° and stratum width is equal to $200m$. Again, each analysis includes sFP changes in five points of interest.

Similar to previous sections, it seems that in this injection program, seismic risk activity is relatively less outside stratum layer where point A and point E are located, since in all cases and simulations there is not much of change in sFP through time for this point. This can be understood from Figure 3.51 to 3.54.

Figures 3.55 to 3.60 show the results obtained for sFP evolution in points B, C, and D. The trend of sFP change is similar in these three locations under both stress regimes.

Increase in seismic activity potential is always higher when the injection point is nearer to the fault. This is what was expected to be observed before running the simulations. Again, extensional stress regime is more at risk. It also seems that the most critical location point D. It is interesting to observe that only $250m$ difference between injection zone and fault make a huge difference in occurrence of seismic failure in terms of time.

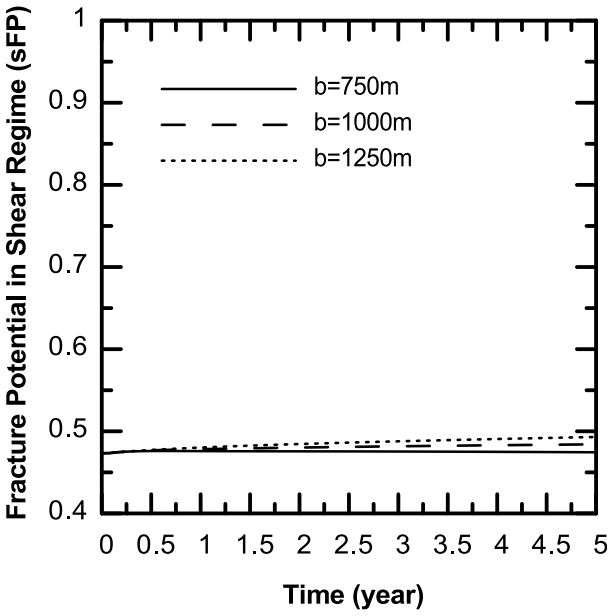

Figure 3.51 sFP evolution in 5 years for point A in compressional regime in case of different distances between injection zone and fault.

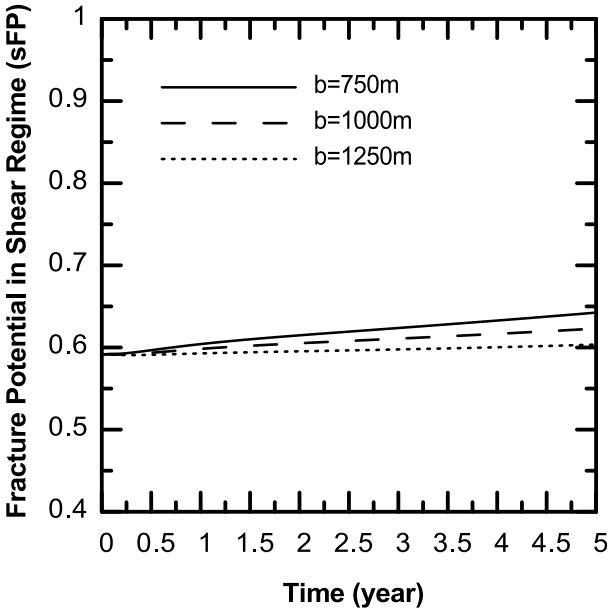

Figure 3.52 sFP evolution in 5 years for point A in extensional regime in case of different distances between injection zone and fault.

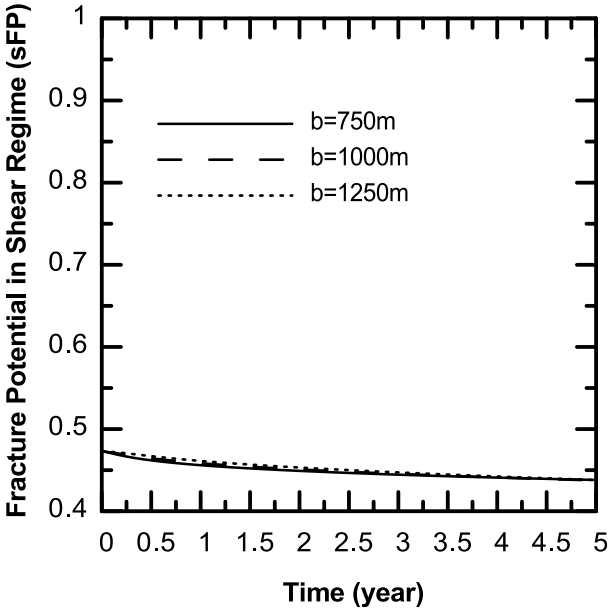

Figure 3.53 sFP evolution in 5 years for point E in compressional regime in case of different distances between injection zone and fault.

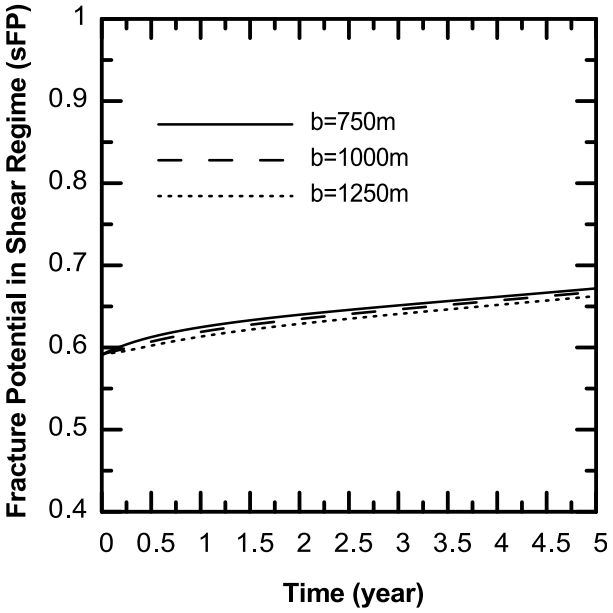

Figure 3.54 sFP evolution in 5 years for point E in extensional regime in case of different distances between injection zone and fault (Continuous line: $750m$,dashed line: $1000m$,dotted line: $1250m$).

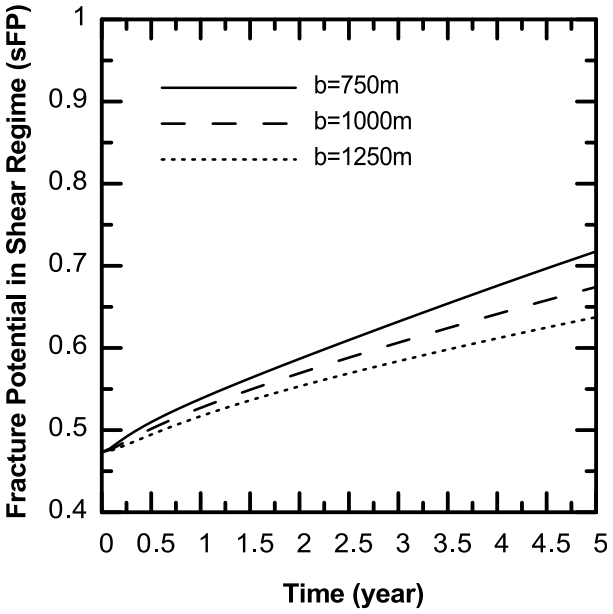

Figure 3.55 sFP evolution in 5 years for point B in compressional regime in case of different distances between injection zone and fault.

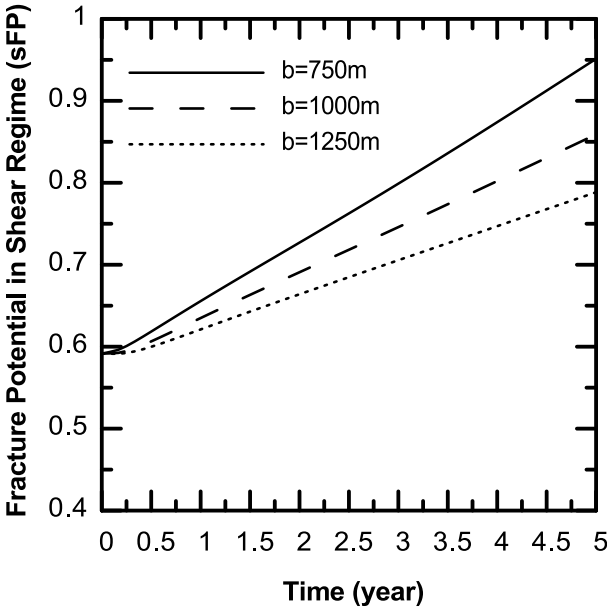

Figure 3.56 sFP evolution in 5 years for point B in extensional regime in case of different distances between injection zone and fault.

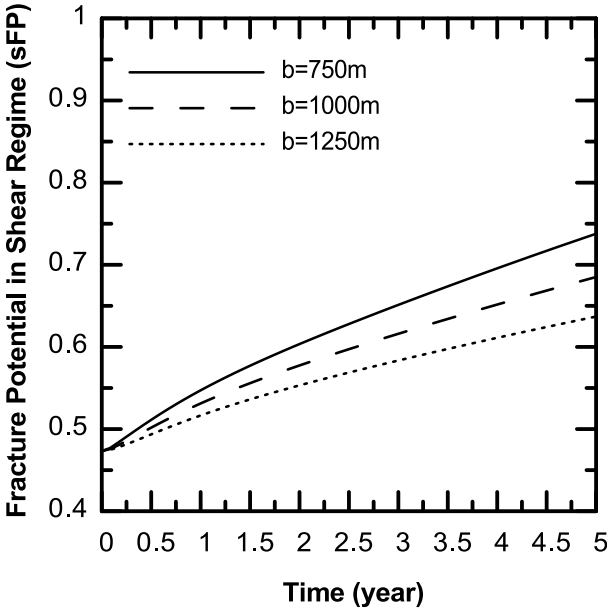

Figure 3.57 sFP evolution in 5 years for point C in compressional regime in case of different distances between injection zone and fault.

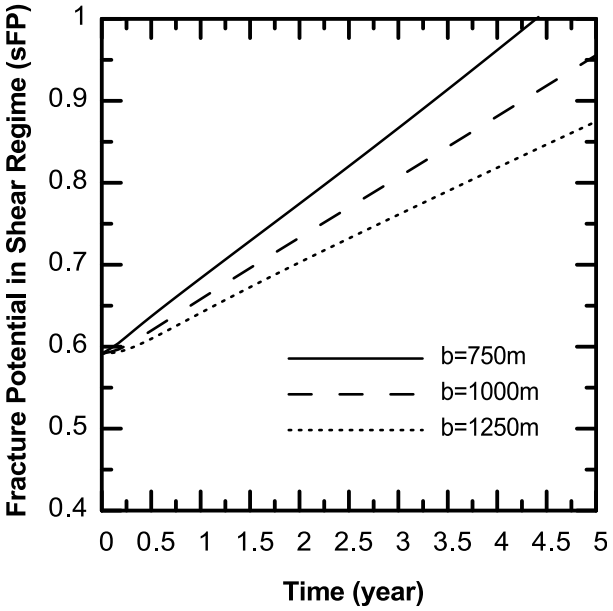

Figure 3.58 sFP evolution in 5 years for point C in extensional regime in case of different distances between injection zone and fault.

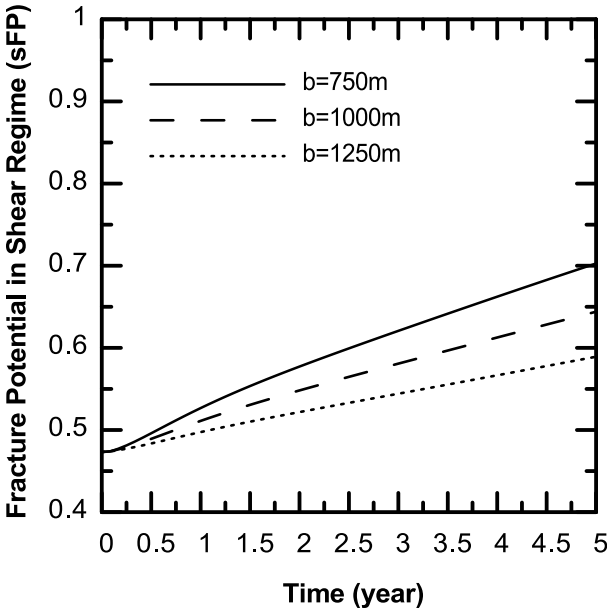

Figure 3.59 sFP evolution in 5 years for point D in compressional regime in case of different distances between injection zone and fault.

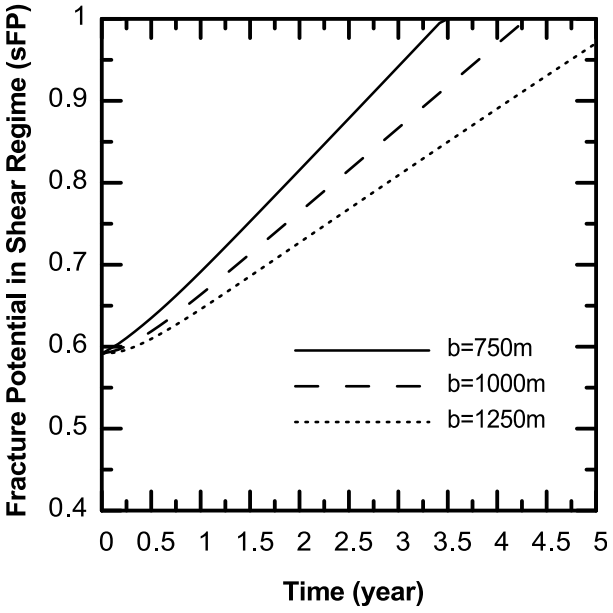

Figure 3.60 sFP evolution in 5 years for point D in extensional regime in case of different distances between injection zone and fault.

3.8.4 Effect of Fault Stiffness

The effect of fault stiffness is studied by changing the value of Young's modulus and observing the results. Other varying parameters are held constant. The fault angle is considered equal to 60°, a is equal to $200m$ and b is equal to $1000m$.

Changes in seismic activity are still not significant at points A and E (Figures 3.61 to 3.64). In compressional stress regime, in points located in the stratum, it is interesting yet unexpected to see that the seismic potential is increasing with higher values of fault stiffness. However, in an extensional regime, highest value of fault stiffness shows the lowest seismic potential in point B and point C, with a significant difference, but in point D the behaviour is opposite. This is the first time in all simulations where the seismic activity is higher in compressional regime, which means the stress drop is more in vertical direction than horizontal. The plots are presented in Figures 3.65 to 3.70.

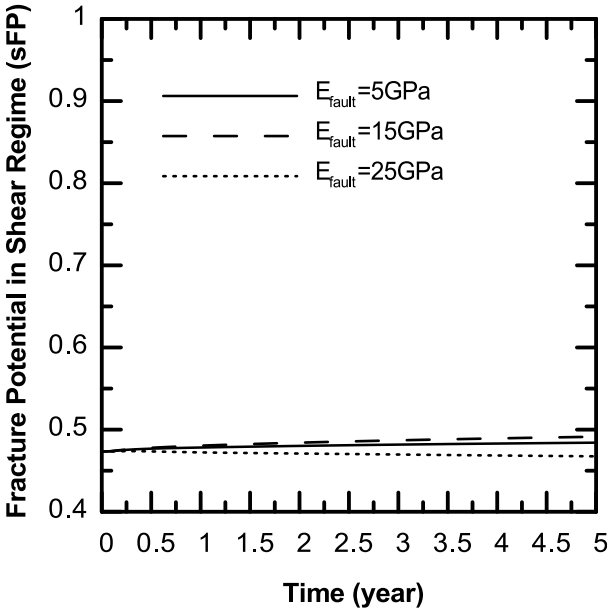

Figure 3.61 sFP evolution in 5 years for point A in compressional regime in case of different fault stiffness.

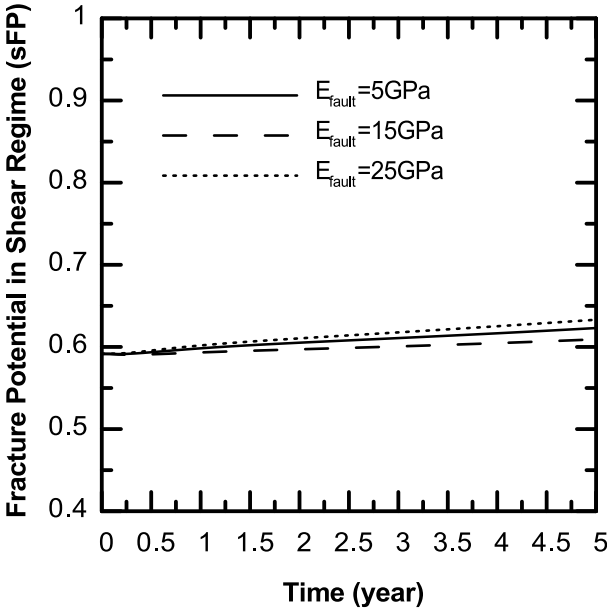

Figure 3.62 sFP evolution in 5 years for point A in extensional regime in case of different fault stiffness.

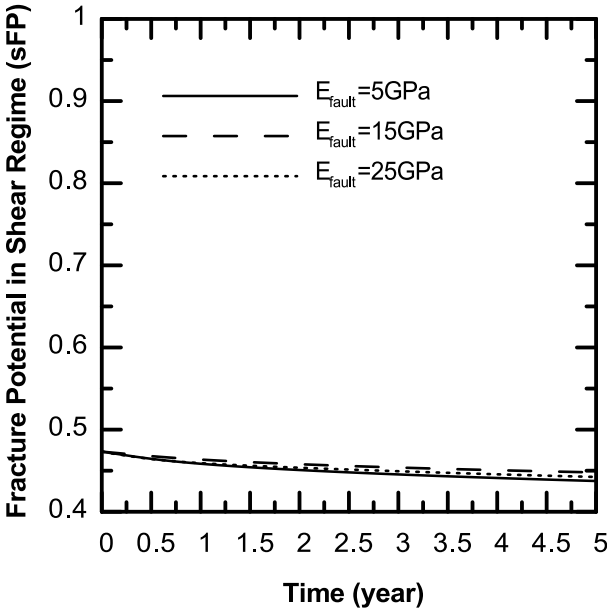

Figure 3.63 sFP evolution in 5 years for point E in compressional regime in case of different fault stiffness

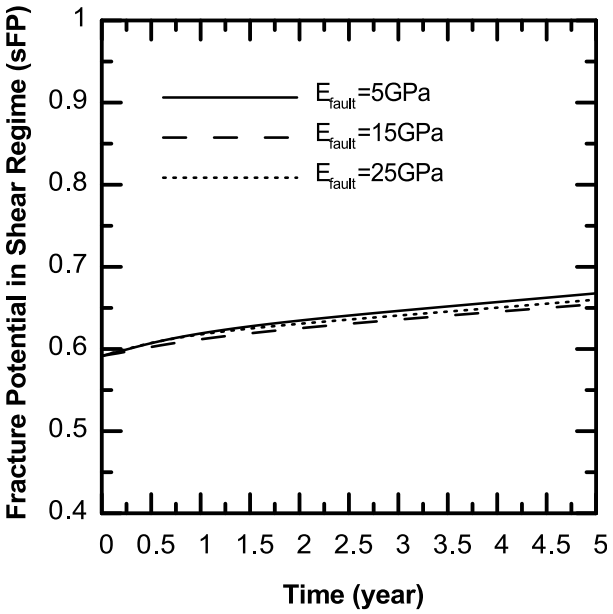

Figure 3.64 sFP evolution in 5 years for point E in extensional regime in case of different fault stiffness.

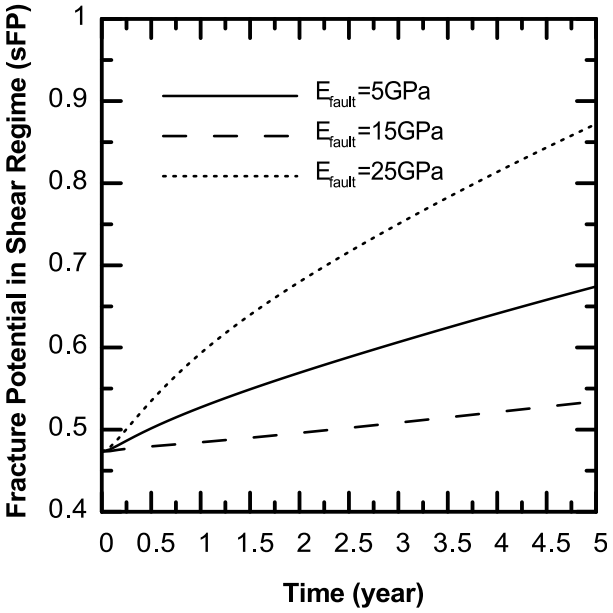

Figure 3.65 sFP evolution in 5 years for point B in compressional regime in case of different fault stiffness.

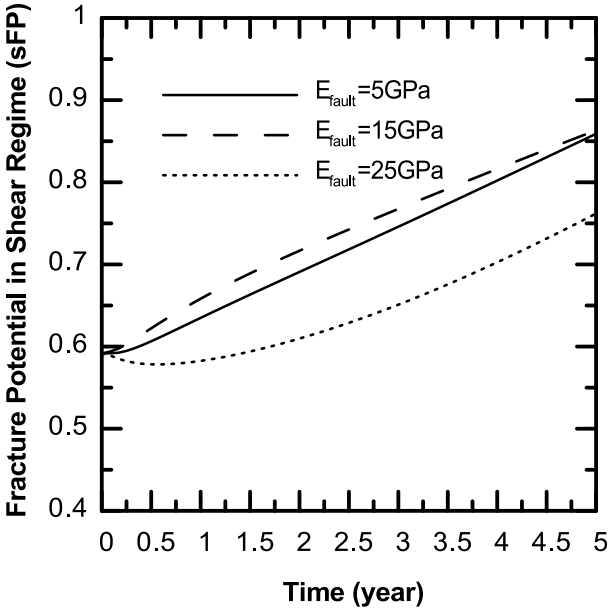

Figure 3.66 sFP evolution in 5 years for point B in extensional regime in case of different fault stiffness.

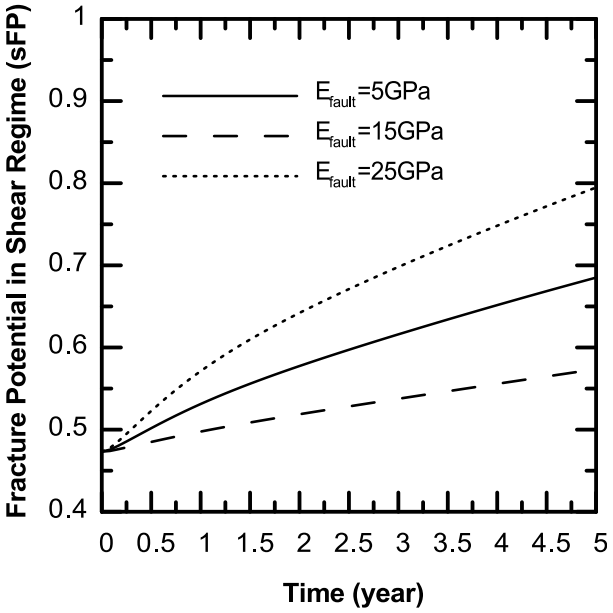

Figure 3.67 sFP evolution in 5 years for point C in compressional regime in case of different fault stiffness.

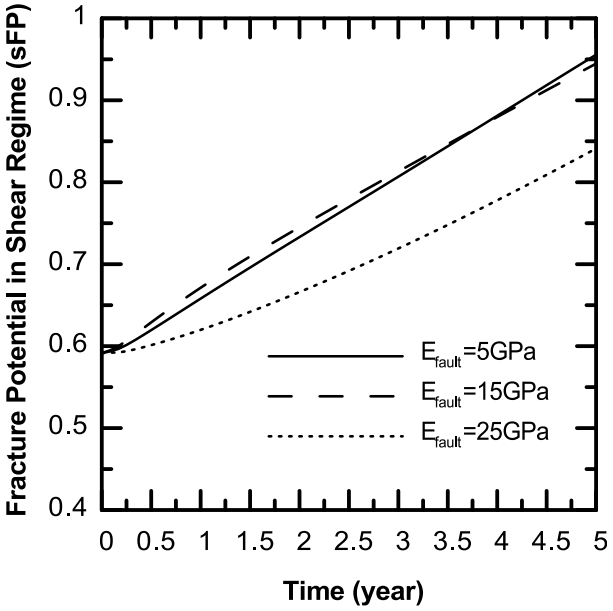

Figure 3.68 sFP evolution in 5 years for point C in extensional regime in case of different fault stiffness.

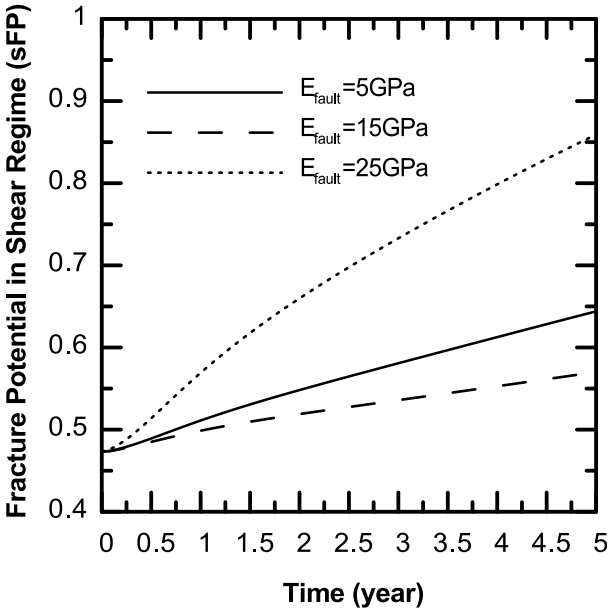

Figure 3.69 sFP evolution in 5 years for point D in compressional regime in case of different fault stiffness.

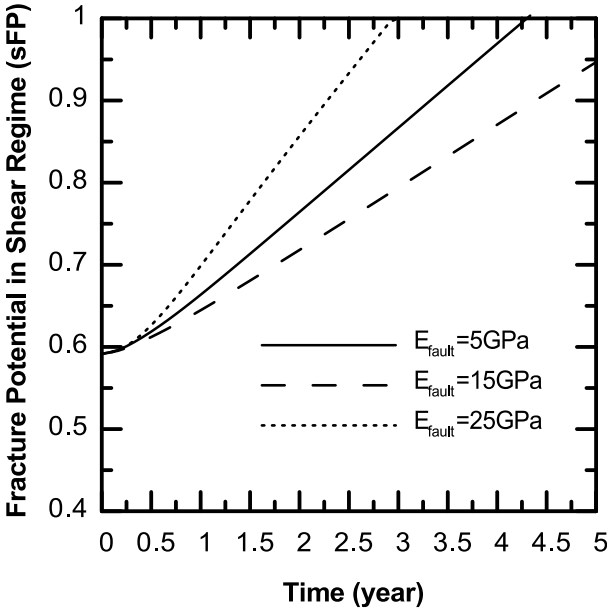

Figure 3.70 sFP evolution in 5 years for point D in extensional regime in case of different fault stiffness.

3.8.5 Effect of Poisson's Ratio of the Medium

In this section, it is tried to observe how a change in Poisson's ratio of the medium affects seismic activity. All of input values are the ones presented in Table 3.7. Values selected for fault angle, stratum thickness, and distance between fault and injection zone are the same as previous section. Three values of 0.25, 0.35, and 0.45 are considered for Possion's ratio.

Under compressional regime in points A and E, sFP either decreases or does not change. Under extensional regime, small increase in sFP is observed on both locations. This small increase is higher in case of higher Poisson's ratio (Figures 3.71 to 3.74).

As it can be deduced from Figures 3.75 to 3.80, except in point B under compressional regime, higher values of Poisson's ratio tend to show more seismic activity, often leading to actual seismic failure. Among all parameters studied so far, the case of high Poisson ratio exhibits the earliest failure in the medium. However, this case cannot be directly compared to others since input values are different. This note was only mentioned in order to state that Poisson's ratio is seemed to highly affect the results comparing to other varying factors. Similar to most previous cases, the most critical point is D where failure is observed in all three cases under extensional regime.

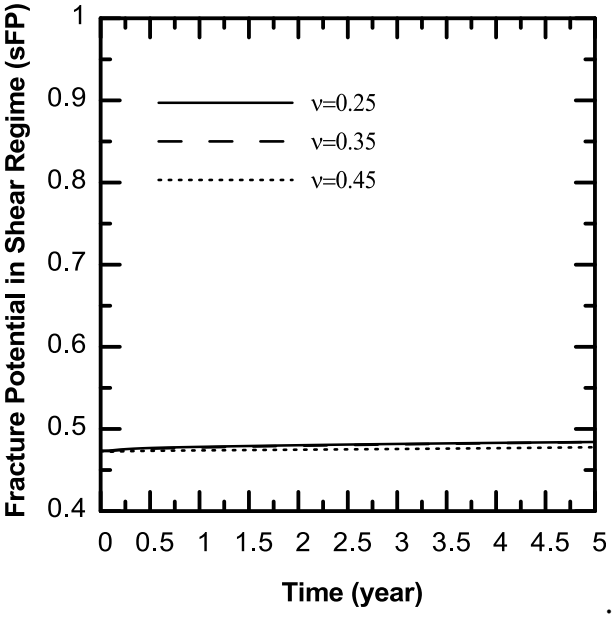

Figure 3.71 sFP evolution in 5 years for point A in compressional regime in case of choosing different Poisson's ratio for medium.

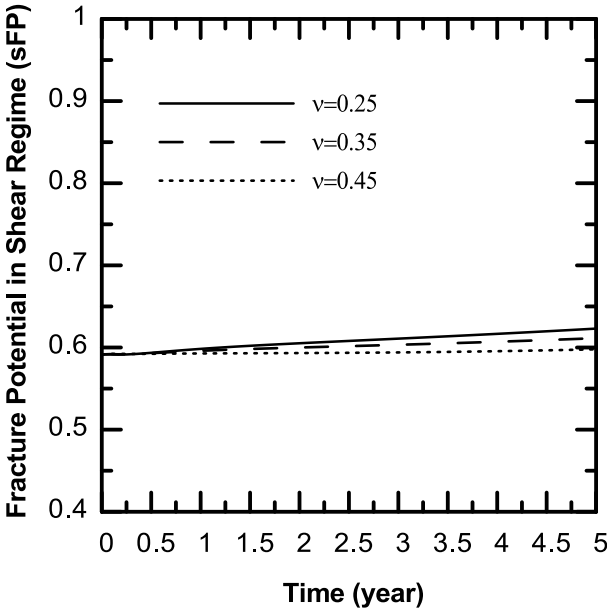

Figure 3.72 sFP evolution in 5 years for point A in extensional regime in case of choosing different Poisson's ratio for medium.

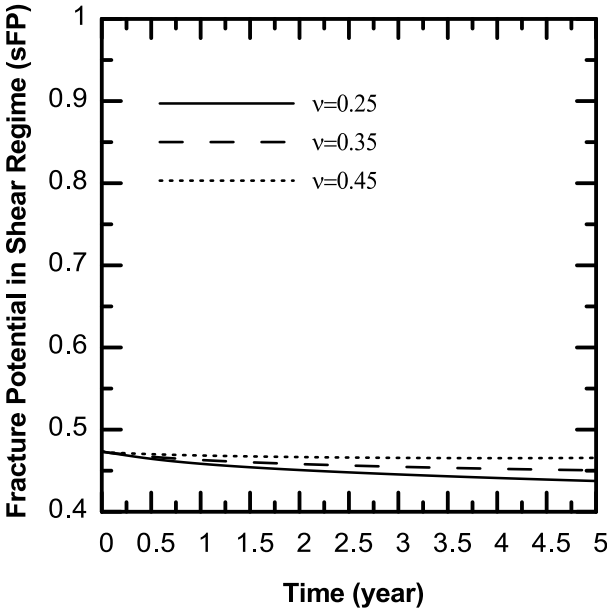

Figure 3.73 sFP evolution in 5 years for point E in compressional regime in case of choosing different Poisson's ratio for medium.

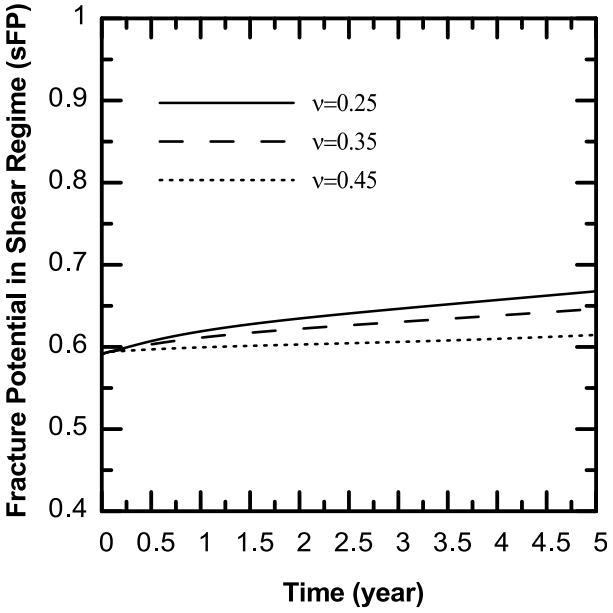

Figure 3.74 sFP evolution in 5 years for point E in extensional regime in case of choosing different Poisson's ratio for medium.

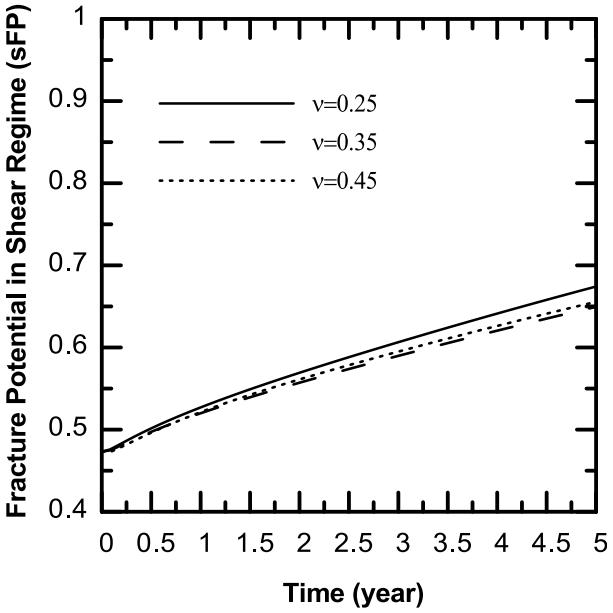

Figure 3.75 sFP evolution in 5 years for point B in compressional regime in case of choosing different Poisson's ratio for medium.

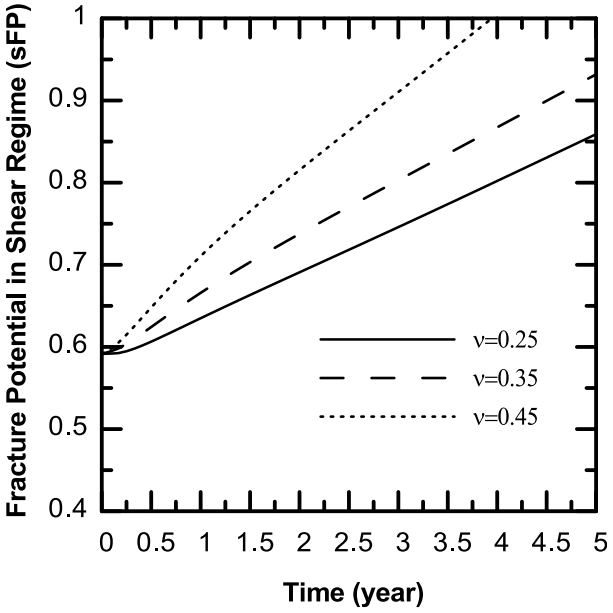

Figure 3.76 sFP evolution in 5 years for point B in extensional regime in case of choosing different Poisson's ratio for medium.

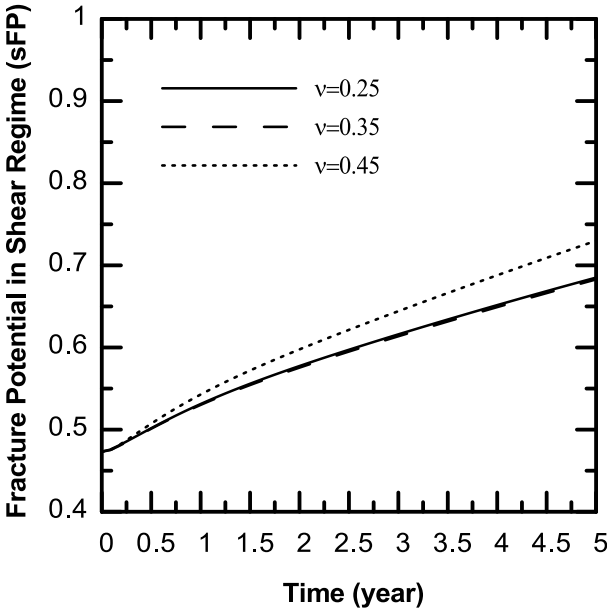

Figure 3.77 sFP evolution in 5 years for point C in compressional regime in case of choosing different Poisson's ratio for medium.

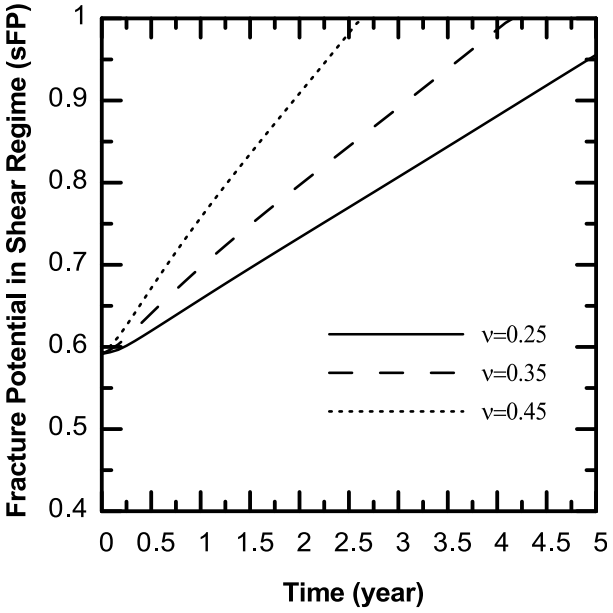

Figure 3.78 sFP evolution in 5 years for point C in extensional regime in case of choosing different Poisson's ratio for medium.

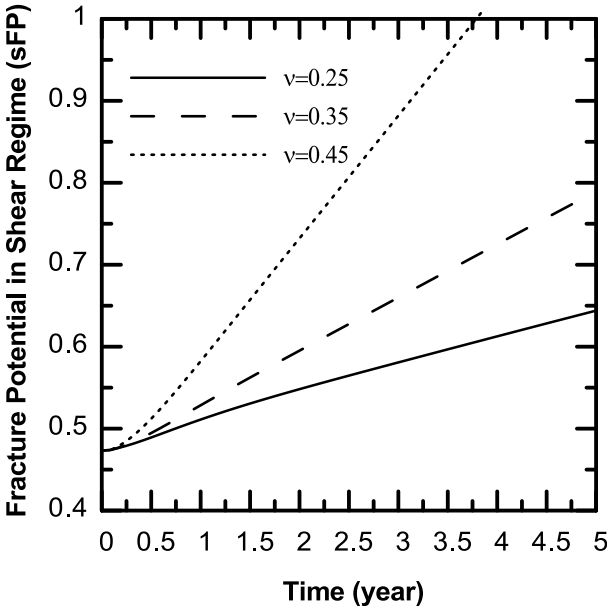

Figure 3.79 sFP evolution in 5 years for point D in compressional regime in case of choosing different Poisson's ratio for medium.

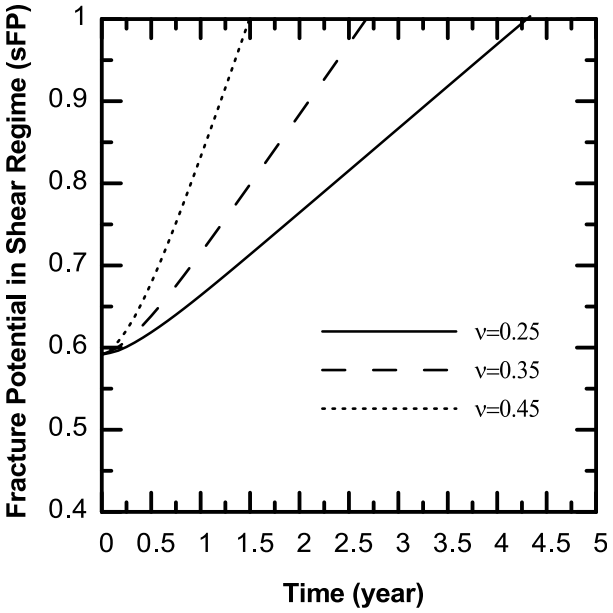

Figure 3.80 sFP evolution in 5 years for point D in extensional regime in case of choosing different Poisson's ratio for medium.

CHAPTER 4 – Summary and Conclusions

The aim of this research study was to come up with an efficient method to analyze the problem of induced seismicity in an Enhanced Geothermal System. The thesis starts with introducing geothermal energy and geothermal systems. Chapter 1 is concerned with a detailed introduction of geothermal energy and all available types of geothermal resources. The research scope and objectives are also presented. Chapter 2 highlighted the major geomechanical issues associated with an EGS. A full literature review of in situ stresses, hydraulic fracturing (HF) process, THM coupling studies, and induced seismicity associated with EGS system is presented.

Chapter 3 examined the approach selected for investigation of an Enhanced Geothermal System. Descriptions of geomechanics issues mentioned in chapter 2 were explained from mathematical point of view, leading to introduction of governing equations of subsurface porous media. Finite element method was found suitable for modeling, and a linear Thermo-Hydro-Mechanical fully coupled code was developed in order to obtain the results of cold fluid injection in an enhanced geothermal reservoir. The program is capable of providing with values three major primary unknowns which are displacement field, pressure, and temperature, during a specified period of time. This made available for calculating stress distribution which is a vital secondary variable. The code was verified against several benchmark problems in order to make sure that the outputs were correct. All components of governing equations which play a role in final outputs were used at least once while solving these examples. Subsequently, the concept of shear fracture potential in Mohr-Coulomb diagram was illustrated. Finally, geometry of the problem was defined and effects of several parameters on induced seismicity of an EGS were studied.

The dominant effect on seismic activity of the fault as a result of cold fluid injection is originated from the poroelastic effects. The rate of conductive heat flow in subsurface bedrocks is low. Heat flow in subsurface media is believed to be convectively driven, where the convective term in governing equation of heat transfer appears. This term is highly dependent on permeability of the medium (since it's related to fluid velocity), which is extremely low in our case study. In the FE code, all nonlinearities such as changes in properties are ignored for the sake of simplicity. Therefore, it is not possible to update inputs such as permeability of the medium, which in real case may be increased as a result of injection. Therefore, the temperature drop which is forced to the medium in the injection zone does not spread and never reaches the fault. As a result, the first recommendation for future studies is to add nonlinearity to the governing equation of fluid flow.

Generally, the fact that there is not a noticeable seismic activity in two points which are located outside the permeable zone shows that the stress drops as a result of injection are mostly limited to the location where fault meets the stratum. At least for this injection program, this is what was observed in almost all cases of simulation in point A and point E. Therefore, the final conclusions and judgements are mostly based on other three points of interest which are located in the stratum.

Although the major outcome of sFP graphs is the probability of seismic activity and figuring out whether a seismic event is triggered or not, comparison of the graphs under two different stress regimes in each point can provide with well understanding of the path of stress drop. In most cases among the simulations, it is observed that the final value of sFP is higher in extensional stress regime comparing to compressional stress regime. This means that probably horizontal effective stress drop is as much as or more than vertical effective

stress drop. Or the fact that sFP is increasing in most cases inside the stratum regardless of the stress regime means that there is always a significant induced shear stress as a result of injection.

It was found that inside the permeable layer, higher fault angle shows more potential of seismic activity in an extensional regime, whereas the opposite trend is observed in compressional stress regime. Also, seismic potential increases when the injection zone is nearer to the fault. This effect is relatively higher in an extensional regime. The system is at more risk in case of dealing with thinner permeable layer. Higher fault stiffness tends to express more seismic activity in a compressional regime, however, there is no general trend in an extensional regime and each point shows different order of results in case of different fault stiffness. Simulations carried out with different Poisson's ratio showed that this parameter is highly effective on outputs and higher values of Poisson's ratio result in a significant higher seismic activity.

In order to summarize and highlight the results, the main conclusions are briefly outlined in the following:

- Amount of seismic activity increase is relatively higher in an extensional regime in almost all cases. This means the drop in horizontal effective stress is almost equal to or more than vertical effective stress drop.
- Thermo-elastic stresses do not show up since the permeability of the medium is not sufficiently enough to result in convective heat transfer and therefore there is no temperature change on the fault.
- Increase in seismic activity is mainly limited to where the fault meets the stratum.

- Higher fault angle is more at risk in an extensional regime, whereas the lower angle shows more seismic potential growth in compressional regime.
- As expected, lower distance between injection zone and fault zone results in more seismic potential.
- Lower thickness of stratum leads to more increase in seismic potential of the fault.
- No general trend is observed in case of different values of fault stiffness.
- Higher Poisson's ratio of the medium results in higher seismic activity as the injection program starts.

For future studies, it is highly recommended to introduce nonlinearity into the model in order to understand the effects of thermal processes as well. Also, it is obvious that expanding the code to model a three-dimensional geological medium will be more realistic. This research is conducted on a large-scale area, ignoring the function of fracture network and how it grows as a result of injection. Therefore, modeling fracture generation and propagation in a small scale can be a complementary analysis for this study.

References

Aboud-Sayed, A.S., Brechtel, C.E., Clifton, R.J., 1978. In situ stress determination by hydrofracturing: a fracture mechanics approach. JGR, 83, 2851-2862.

Aboustit, B.L., Advani S.H., and Lee, J.K., 1985. Variational principles and finite element simulations for thermo-elastic consolidation', Int. J. Num. An. Methods in Geomech., 9,49-69.

Amadei, B., Stephansson, O., 1997. Rock stress and its measurement. Chapman and Hall, London.

Barbier, E., 2002. Geothermal energy technology and current status: An overview. Renewable and Sustainable Energy Reviews, 6: 3-65.

Barenblatt, G.I., The mathematical theory of equilibrium cracks in brittle fracture. Advan. Appl. Mech. 7:55-129, 1962.

Baria, R., Baumgartner, J., Gerrard, A., Jung, R., Garnish, J., 1999. European HDR research programme at Soultz-sous-Forets (France) 1987–1996. Geothermics 28:655–669.

Bear, J., 1972. Dynamics of fluid in porous media. Reprint of the American Elsevier Publishing Company, Inc., New York, 1972 edition.

Bertani , R.,2015. Geothermal Power Generation in the World 2010-2014 Update Report. Proceedings World Geothermal Congress 2015. Melbourne, Austrailia, 2015.

Bell, J.S., 2003. Practical methods for estimating in situ stresses for borehole stability applications in sedimentary basins. J Pet Sci Eng 38:111–119.

Biot, M.A., 1941. General theory of three-dimensional consolidation, J. Appl. Phys. 12 (1941) 155–164.

Biot, M.A., 1956. Thermoelasticity and irreversible thermodynamics. Journal of Applied Physics, Vol. 27, No. 3, 240-253.

Bishop, A.W., 1973. The influence of an undrained change in stress on the pore pressure in porous media of low compressibility. Geotechnique, 435-442.

Bobet, A., Einstein, H.H., 1998. Numerical modeling of fracture coalescence in a model rock material. Int J Fract 92:221–252.

Boone, T.J., Ingraffea, A.R., Roegiers, J.C., 1991. Simulation of hydraulic fracture propagation in poroelastic rock with application to stress measurement technique. Int J Numer Anal Meth Geomech 28:1–14.

Bredehoeft, J.D., Wolff, R.G., Keys, W.S., 1976. Hydraulic fracturing to determine the regional in situ stress field, Piceance Basin, Colorado.

Burns, K.L., 1990. Hot Dry Rock Research – A compendium of publications Oct. 89 -Sept. 90, Los Alamos Nat. Lab. 1990 Fiscal year Report.

Cao, W., Huang, W., Jiang, F., 2015. A Thermal-Hydraulic-Mechanical Fully Coupled Model for Heat Extraction in Enhanced Geothermal Systems. Proceedings World Geothermal Congress 2015. Melbourne, Australia.

Cappa, F., Rutqvist, J., 2011. Modeling of coupled deformation and permeability evolution during fault reactivation induced by deep underground injection of CO_2. International Journal of Greenhouse Gas Control. Volume 5, Issue 2, Pages 336-346.

Carter, B.J., Desroches, J., Ingraffea, A.R., Wawrzynek, P.A., 2000. Simulating fully 3D hydraulic fracturing. In: Zaman, M., Booker, J., Gioda, G., (eds) Modeling in geomechanics. Wiley Publishers, New York.

Carter, J.P., Booker, J.R., 1989. Finite element analysis of coupled thermo-elasticity. ComputersandStructures Vol. 31, No. 1, pp. 73-80.

Chen, W., Tan, X., Yu, H., Wu, G., Jia, S., 2009. A fully coupled thermo-hydro-mechanical model for unsaturated porous media Journal of Rock Mechanics and Geotechnical Engineering, 1 (1): 31–40.

Christianovich, S.A., Zheltov, Y.P., Barenblatt, G.I., Maximovich, G.K., 1959. Theoretical principles of hydraulic fracturing of oil strata. Proc. 5th World Petr. Congr., New York, Section II 23, 289-296.

Combarnous, M.A., and Bories, S.A., 1975. Hydrothermal Convection in Saturated Porous Media, Advances in Hydroscience, vol.10, Academic press, New York.

Cornet, F.H., 1987. Results from Le Mayet de Montagne project. Geothermics 16(4):355–374.

Cornet, F.H., 2000. Comment on Large-scale in situ permeability tensor of rocks from induced microseismicity by S.A.

Crank, J., 1975. The mathematics of diffusion. Brunel University Uxbridge. Second edition.

Das, I., Zoback, M.D., 2011. Long period long duration seismic events during hydraulic fracture stimulation of a shale gas reservoir: The Leading Edge, 30, 778–786, doi: 10.1190/1.3609093.

De Pater, C.J., Baisch, S., 2011.Geomechanical Study of Bowland Shale Seismicity :Synthesis Report.

Dickson, M.H. and Fanelli, M., 1990. Small Geothermal Resources: A Guide to Development and Utilization, UNITAR, New York.

DiPippo, R., 2004. Second Law assessment of binary plants generating power from low temperature geothermal fluids. Geothermics 33, 565-586.

Dobroskok, A.A., Ghassemi, A., Linkov, A.M., 2005. Numerical simulation of crack propagation influenced by thermal and porous liquid stresses. Int J of Fract 134:L29–L34.

Duchane, D.V., 1996. Geothermal energy from hot dry rock: A renewable energy technology moving. towards practical implementation . Renewable Energy, 9(1-4): 1246-1249.

Dunn, J.C., 1988. Research to tap the crustal magma source. Proc. Geothermal Program Review VI, "Beyond goals and objectives", April 19–21, 1988, San Francisco, California: 151–153.

Eckert, A., 2007. 3D multi-scale finite element analysis of the crustal state of stress in the Western US and the Eastern California Shear Zone, and implications for stress – fluid flow interactions for the Coso Geothermal Field.

Economides, M.J., Nolte, K.G., 1987. Reservoir stimulation. Schlumberger Educational Services Houston, SMP-7018.

Evans, K.F., Cornet, F.H., Hashida, T., Hayashi, K., Ito, T., Matsuki, K., Wallroth, T., 1999. Stress and rock mechanics issues of relevance to HDR/HWR engineered geothermal systems: review of developments during the past 15 years. Geothermics 28:455–474.

Evans, K.F., Zappone, A., Kraft, T., Deichmann, N., Moia, F., 2012. A survey of the induced seismic responses to fluid injection in geothermal and CO2 reservoirs in Europe. Geothermics 41:30–54.

Ferronato, M., Castelletto, N., Gambolati, G., 2010. A fully coupled 3-D mixed finite element model of Biot consolidation. Journal of Computational Physics 229 (2010) 4813-4830.

Ghaboussi, J., and Wilson, E.L., 1973. Flow of compressible fluid in porous elastic solids. Int. J. numer. methods eng., 5,419442.

Ghassemi, A., Roegiers, J-C., 1996. A three-dimensional poroelastic hydraulic fracture simulator using the displacement discontinuity method. In: Proceedings of the 2nd North American rock mechanics symposium, Montreal, pp 982–987.

Ghassemi, A., Tarasovs, S., Cheng, A.D., 2003. An Integral equation method for modeling three-dimensional heat extraction from a fracture in hot dry rock. Int J Numer Anal Methods Geomech 27(12):989–1004.

Ghassemi, A., Zhou, X.X., 2011. A three-dimensional poro- and thermoelastic model for analysis of fracture response in EGS. Geothermics 40:39–49.

Ghassemi, A., 2012. A Review of Some Rock Mechanics Issues in Geothermal Reservoir Development. Journal of Geotechnical Geological Engineering, 30:647–664, DOI 10.1007/s10706-012-9508-3 .

Ghomshei, M.M., Sadler-Brown, T., 1996. Direct Use Energy from the hotsprings and subsurface geothermal resources of British Columbia, Canadian Geothermal Energy Association, BTech Publishers, Richmond, BC.

Goodman, R.E., Taylor, R.L., and Brekke, T.L., 1968. A model for the mechanics of jointed rock. Journal of Soil Mechanics and Foundation Division, ASCE, 99(SM3):637-659.

Goodman, R.E., and St.John, C., 1977. Finite element analysis for discontinuous rocks. In Desai C.S. and Christian, J.T., editors, Numerical Methods in Geotechnical Engineering, chapter , pages 149-175. McGraw-Hill, New York.

Grasby, S.E., Allen, D.M., Bell, S., Chen, Z., Ferguson, G., Jessop, A., Kelman, M., Ko, M., Majorowicz, J., Moore, M., Raymond, J., Therrien, R., 2012. Geothermal Energy Resource Potential of Canada. Geological Survey of Canada Open File 6914.

Geertsma, J., de Klerk, F.A., 1969. A rapid method of predicting width and extent of hydraulically induced fractures. Journal of Petroleum Technology (Dec):1571–1581.

Haimson, B., 1968. Hydraulic fracturing in porous and nonporous rock and its potential for determining in situ stresses at great depth. PhD-thesis, Univ. Minnesota.

Haring, M., Ulich, S., Ladner, F., Dyer, B., 2008. Characterization of the basel 1 enhanced geothermal system. Geothermics 37(5):469–495.

Hochstein, M.P., 1990. Classification and assessment of geothermal resources. In: Dickson MH, Fanelli M, editors. Small geothermal resources - A guide to development and utilization. Rome Italy, UNITAR/UNDP Centre on Small Energy Resources: 31-59.

Hopkirk, R.J., Sharma, D., Pralong, P.J., 1981. Coupled convective and conductive heat transfer in the analysis of HDR geothermal sources. In: Lewis RW et al (eds) Numerical methods in heat transfer. Wiley, New York, pp 261–307.

Howard, G.C., Fast, C.R., 1957. Optimum fluid characteristics for fracture extension. Drilling and Production Practise, 261 ff. .

Hubbert, M., Willis, D., 1957. Mechanics of Hydraulic Fracturing. Trans. AIME, Vol. 210, 153-168.

International Energy Agency, 2011. Geothermal Road Map.

Jaeger J., Cook, N.G., Zimmerman, R., 2007. Fundamentals of Rock Mechanics.

Jeffrey, R.G., Zhang, X., Bunger, A.P., 2010. Hydraulic fracturing of naturally fractured reservoirs. In: Proceedings of the 35th workshop on geothermal reservoir engineering Stanford University, Stanford, CA.

Kappelmeyer,O., Gerard, A., 1987. Production of heat from impervious hot crystalline rock sections (hot-dry-rock concept). In: Terrestrial heat from impervious rocks-Investigation in the Falkenberg granite massif. Geologisches Jahrbuc, Reihr E, Heft 39, pp 7–22.

Karahanoglu, N., Doyuran, V., Akkas, N., 1984. Finite element simulation of hot water-type geothermal reservoirs. Journal of Volcanology and Geothermal Research, 23 (1984) 357-382.

Kelkar, S., Lewis, K., Karra, S., Zyvoloski, G., Rapaka, S., Viswanathan, H., Mishra, P.K., Chu, S., Coblentz, D., Pawar, R., 2014. A simulator for modeling coupled thermo-hydro-mechanical processes in subsurface geological media. International Journal of Rock Mechanics and Mining Sciences 70. 569–580.

Kim, J-M., Parizek, R.R., 1997. Numerical simulation of the Noordbergum effect resulting from groundwater pumping in a layered aquifer system. Journal of Hydrology 202 (1997) 231–243.

Kirsch, G., 1898. Die Theorie der Elastizität und die Bedürfnisse der Festigkeitslehre. Zeitschrift des Vereines deutscher Ingenieure 42 (28): 797–807.

Kohl, T., Evans, K.F., Hopkirk, R.J., Ryback, L., 1995. Coupled hydraulic, thermal, and mechanical considerations for the simulation of hot dry rock reservoirs. Geothermics 24:345–359.

Koshelev, V.F., Ghassemi, A., 2003. Hydraulic fracture propagation near a natural discontinuity. In Proceedings of the 28th Geotech Geol Eng (2012) 30:647–664 661. workshop on geothermal reservoir engineering. Stanford University, Stanford, CA

Lecampion, B., Jeffrey, R., Detournay, E., 2005. Resolving the Geometry of Hydraulic Fractures from Tilt Measurements. *Pure and Applied Geophysics*, 162: 2433-2452.

Li, J., and Kaliakin, V.N., 1993. Numerical simulation of interfaces in geomaterials: Development of new zero-thickness interface elements. Civil Engineering Report No. 93-6. Department of Civil Engineering. University of Delaware. Newark, Delaware 19716.

Liu, G.R., Nourbakhshnia, N., Zhang, Y.W., 2011. A novel singular ES-FEM method for simulating singular stress fields near the crack tips for linear fracture problems. Engineering Fracture Mechanics 78 (2011) 863–876.

Lund, J., Sanner, B., Rybach, L., Curtis, R., Hellstrom G., 2004. Geothermal (Ground-Source) Heat Pumps: A World Overview. GHC Bulletin, September 2004, 1-10.

Lund, J., Freeston, D.H., Boyd, T.L., 2010. Direct Utilization of Geothermal Energy 2010 Worldwide Review. Proceedings World Geothermal Congress 2010 Bali, Indonesia, 25-29 April 2010.

Mandel, J., 1953.Consolidation des sols (étude mathématique), Géotechnique 30 (1953) 287–289.

Majer, E.L., 2007. White Paper: Induced seismicity and enhanced geothermal systems. Center for Computational Seismology, Ernest Orlando Lawrence Berkeley Laboratory, Berkelely 32 pp.

Majer, E.L., Baria, R., Stark. M., Oates, S., Bommer, J., Smith, B. and Asanuma, H., 2007. Induced seismicity associated with Enhanced Geothermal Systems, Geothermics 36, 185-222.

Meier, P.M., Rodriguez, A.A., Bethmann, F., 2015. Lessons learned from Basel: New EGS projects in Switzerland using multistage stimulation and a probabilistic Traffic Light System for reduction of seismic risk. Proceedings World Geothermal Congress 2015.

MIT (Massachusetts Institute of Technology), 2006. The Future of Geothermal Energy: Impact of Enhanced Geothermal Systems (EGS) on the United States in the 21st Century, pp. 372.

Nathwani, J., Blackstock, J., 2012. A report on the outcomes of the Equinox Summit: Energy 2030, convened by the Waterloo Global Science Initiative and held in Waterloo, Ontario, Canada on 5-9 June 2011

Nguyen, V.P., 2014. An open source program to generate zero-thickness cohesive interface elements. Advances in Engineering Software 74 (2014) 27–39.

Nowacki, W., 1963. Thermoelasticity. Volume 3 in the International Series of Monographs in Aeronautics and Astronautics, Division 1. Pergamon Press, London. 628 pp. 6 gns.

Olson, J.E. (2008) Multi-fracture propagation modeling: application to hydraulic fracturing in shale and tight gas sands. In: Proceedings of the 42nd American rock mechanics symposium, San Francisco.

Parotidis, M., Shapiro, S.A., Rothert, E., 2004. Backfront of seismicity induced after termination of borehole fluid injection. Geophys Res Lett 31:L02612. doi:10.1029/2003 GL018987.

Perkins, T.K., Kern, L.R., 1961. Widths of hydraulic fractures. J Pet Tech Sep, pp 937–949.

Reddy, J.N., 2006. An introduction to the finite element method. McGraw-Hill.

Rothert, E., Shapiro, S.A., 2003. Microseismic monitoring of borehole fluid injections: Data modeling and inversion for hydraulic properties of rocks. Geophysics 68:685–689.doi: 10.1190/1.1567239.

Rummel, F., Hansen, J., 1989. Interpretation of hydrofrac pressure recordings using a simple fracture mechanics simulation model. Int. J. Rock Mech., 26/6, 483-488.

Rutqvist, J., Oldenburg, C., 2007. Analysis of cause and mechanism for injection-induced seismicity at the Geysers Geothermal Field, California. Lawrence Berkeley National Laboratory, http://repositories.cdlib.org/lbnl/LBNL-63015 .

Rutqvist, J., Stephansson, O., 2003. The role of hydromechanical coupling in fractured rock engineering. Hydrol J 11:7–40.

Rutqvist, J., Rinaldi, P., Cappa, F., Moridis, G.J., 2013. Modeling of fault reactivation and induced seismicity during hydraulic fracturing of shale-gas reservoirs. Journal of Petroleum Science and Engineering 107 (2013) 31-44.

Rutqvist, J., 2015. Fractured rock stress-permeability relationships from in situ data and effects of temperature and chemical-mechanical couplings. Geofluids (2015) 15, 48-66.

Sandhu R.S. , and Wilson, E.L. , 1969. Finite element analysis of seepage in elastic media. J. Eng. Mech. Div., ASCE,95.

Scholz, H., 1990. The Mechanics of Earthquakes and Faulting. Cambridge University Press, New York, 1990.

Selvadurai, A.P.S., Nguyen, T.S., 1993. Computational modeling of isothermal consolidation of fractured porous media. Computers and Geotechnics 17 (1995) 39-73.

Sesetty, V., Ghassemi, A., 2012. Modeling and analysis of stimulation for fracture network generation. In: Proceedings of the 37th workshop on geothermal reservoir engineering, Stanford University, Stanford, CA.

Shapiro, S., Huenges, E., Borm, G., 1997. Estimating the crust permeability from fluid-injection-induced seismic emission at the KTB site. Geophys J Int 131:F15–F18.

Shapiro, S., Audigane P., Royer J., 1999. Large-scale in situ permeability tensor of rocks from induced microseismicity. Geophys J Int 137:207–213.

Shapiro, S.A., Rothert E., Rath, V., Rindschwentner, J., 2002. Characterization of fluid transport properties of reservoirs using induced microseismicity. Geophysics 67:212–220.

Sneddon , I.N., 1946. The distribution of stress in the neighbourhood of a crack in an elastic solid .DOI: 10.1098/rspa.1946.0077.

Swenson, D., Hardemana, B., 1997. The effects of thermal deformation on flow in a jointed geothermal reservoir. Int J Rock Mech Min Sci 34(3–4): 308.E1–308.E19.

Terzaghi, K., 1925. Erdbaumechanik auf Bodenphysikalischer Grundlage, F. Duticke, Vienna.

Timoshenko, S., Goodier, J.N., 1951. Theory of Elasticity. McGraw-Hill Book Company, Inc.

The MathWorks, Inc (2016), Version R2016b < https://www.mathworks.com/> (accessed December 15, 2016).

Thompson, A., Bakhteyar, F., Van Hal, G., 2015. Geothermal Industry Development in Canada- Country Update. Proceedings World Geothermal Congress. Melbourne, Austrailia, 2015.

Tomiya, A., 2000.Depth of magma chamber determined by experimental petrologic methods. Proc. World Geoth. Congress 2000, International Geothermal Association, 5 pages, on CD Rom 2000 (670 papers).

Vaziri, H. H., 1988. Coupled fluid flow and stress analysis of oil sands subject to heating. Journal of Canada Petroleum Technology. 27, 84-91.

Vaziri, H.H., 1996. Theory and application of a fully coupled thermo-hydro-mechanical finite element model. Computers and Strucrures, Vol. 61. No. I. pp 131-146.

Verdon, J.P., Kendall, J.-M, White, D.J., Angus, D.A., 2011. Linking microseismic event observations with geomechanical models to minimise the risks of storing CO_2 in geological formations. Earth and Planetary Science Letters 305 143-152.

Verruijt, A., 1969. Elastic storage of aquifers. Delft University. Reprinted from "Flow through porous media".

Warpinski, N.R., Teufel, L.W., 1987. Influence of geological discontinuities on hydraulic fracture propagation. JPT 39:209–220.

Wells, G.N., Sluys, L.J., 2001. A new method for modelling cohesive cracks using finite elements. International Journal for Numerical Methods in Engineering. .Int. J. Numer. Meth. Engng; 50:2667-2682.

Weng, X., Kresse, O., Cohen, C., Wu, R., Gu, H., 2011. Modeling of hydraulic fracture network propagation in a naturally fractured formation, SPE 140253, presented at the

SPE Hydraulic fracturing technology conference and exhibition held in the woodlands. Texas, USA.

White, D. E., 1973. Characteristics of geothermal resources. In: Kruger, P. and Otte, C.,eds., Geothermal Energy, Stanford University Press, Stanford, pp. 69-94.

Yazid, A., Abdelkader, N., Abdelmadjid, H., 2009. State-of-the-art review of the X-FEM for computational fracture mechanics. Appl Math Model 33:4269–4282.

Zhang, X., Jeffrey, R.J.G., 2006. The role of friction and secondary flaws on deflection and re-initiation of hydraulic fractures at orthogonal pre-existing fractures. Geophys J Int 166:1454–1465.

Zhou, X., Ghassemi, A., 2011. Three-dimensional poroelastic analysis of a pressurized natural fracture. Int J Rock Mech. doi:10.1016/ j.ijrmms.2011.02.002.

Zienkiewicz, O.C. , Humpheson, C. and R.W. Lewis, 1977. A unified approach to soil mechanics problems (including plasticity and viscoplasticityl). Finite Element in Geomechanics. edited by Gudehus, G., 151-178, John Wiley and Sons.